SPATIAL AND TEMPORAL VARIATIONS IN SLIP BEHAVIOR BENEATH ALASKA-ALEUTIAN SUBDUCTION ZONE

By

Shanshan Li, M.S.

A Dissertation Submitted in Partial Fulfillment of the Requirements

for the Degree of

Doctor of Philosophy

in

Geophysics

University of Alaska Fairbanks

August 2018

APPROVED:

Dr. Jeffrey T. Freymueller, Committee Chair

Dr. Douglas Christensen, Committee Member

Dr. Carl Tape, Committee Member

Dr. Michael West, Committee Member

Dr. Paul McCarthy, Chair

Department of Geosciences

Dr. Anupma Prakash, Interim Dean

College of Natural Science and Mathematics

Dr. Michael Castellini, Dean

Graduate School

Abstract

Characterizing spatial and temporal variations of slip behavior observed along subduction faults is of great significance for understanding the dynamics of subduction zones, features of great subduction zone earthquakes and deformation patterns across the subduction plate boundary through the seismic cycle. The Alaska-Aleutian subduction zone is one of the most tectonically active margins in the world. Great earthquakes and slow slip events recorded in this area are closely related in space. An increasingly dense array of Global Positioning System (GPS) receivers measures surface deformation at sites with high accuracy and provides a perfect tool for estimating the slip distribution on the plate boundary.

GPS observations show that the motion of the Earth is not entirely linear: the long-term steady motion is interrupted by events like earthquakes, slow slip events (SSEs) and deformation of volcanoes, etc. Two long-term SSEs were detected in Lower Cook Inlet, Alaska (1992.0-2004.8 and 2009.85-2011.81) by inverting the slip distributions from GPS site velocities. The occurrence of SSEs based on the estimated slip distribution patterns provides strong evidence for the transition from stick-slip behavior to episodes and continuous aseismic creep on the subduction plate interface.

Coulomb stressing rate changes (CSRC) due to the two detected long-term SSEs indicate that regions in the shallow slab (30-60 km) that experience significant increase in CSRC show an increase in seismicity rate during SSE periods. The modified quantitative rate/state stress transfer model suggests that the SSEs increase stress on surrounding faults, thereby increasing the seismicity rate even though the ratio of the SSE induced stressing rate to the background stressing rate is small. The SSEs were shown to cause significant stress changes in the seismogenic zone. This highlights the importance of exploring the relationship between SSEs and earthquakes, as well as how this relationship impacts the strain accumulation in the subduction zone.

A repeat survey of the existing campaign GPS sites combined with continuous GPS sites provided a > 20 year time span for estimating the interseismic velocities of the Alaska Peninsula. From this I inferred a more precise model for the location and spatial extent of the change from locked to creeping behavior across the Alaska Peninsula. Given this more detailed distribution of the slip behavior, the results suggest that slip behavior correlates with the pre-existing plate fabric on the downgoing plate, seismic behavior, the reflection character of the slab interface itself and the rupture history of past great earthquakes.

Table of Contents

Page

Title Page i

Abstract iii

Table of Contents iv

List of Figures vii

List of Tables xi

List of Other Materials xiii

List of Appendices xiv

Acknowledgments xv

Chapter 1 General Introduction 1

1.1 Background Review 1

1.2. Thesis Structure 3

1.3 References 4

Chapter 2 Slow slip events and time-dependent variations in locking beneath Lower Cook Inlet of the Alaska-Aleutian Subduction Zone 7

2.1 Abstract 7

2.2 Introduction and Background 8

2.2.1 Objective 8

2.2.2 Tectonic Setting 8

2.2.3 Previous Work 9

2.2.4 Present Study 10

2.3 GPS Data and Analysis 10

2.3.1 GPS Data and Characteristics of the time series 10

2.3.2 Estimating Timing of Velocity Change 11

2.3.3 GPS Velocities 12

2.4 Modeling Approach and Evaluation 13

2.4.1 Block Model 13

2.4.2 Estimation of Angular Velocity of PENN Block 14

2.4.3 Modeling of Slip Deficit Rate Distribution 16

2.5 Results 18

2.5.1 Model Prediction vs. Observed Velocity Data in the four time periods 18

2.5.2 Slip distribution in each time period 18

2.5.3 Model Resolution 20
2.6 Discussion 20
2.6.1 Interseismic slip deficit distribution and reconstruction of slip history over the last 20 years 20
2.6.2 Duration and magnitude scaling of the Lower Cook Inlet slow slip events 23
2.7 Conclusions 24
2.8 Acknowledgments 25
2.9 References 25
Chapter 3 Correlation between Seismicity Rate Changes and Coulomb Stressing Rate Changes due to Slow Slip Events in Lower Cook Inlet, Alaska-Aleutian Subduction Zone 67
3.1 Abstract 67
3.2 Introduction 68
3.3 Data 69
3.3.1 Earthquake Data 69
3.3.2 Source faults of the two long-term SSEs 70
3.3.3 Receiver faults 70
3.4 Method 71
3.4.1 Coulomb Stressing Rate Change Criteria 71
3.4.2 Rate/State Stress Transfer Model 72
3.5 Results 75
3.5.1 Correlation between Increasing Stressing Rate Change due to SSEs and Observed Seismicity Rate Increase 75
3.5.1.1 Correlation Study on Receiver faults based on Optimally Oriented Fault Planes 75
3.5.1.2 Correlation Study on Receiver Faults based on Geometry of Nodal Planes of the Focal Mechanism Solutions 76
3.5.2 Rate/State Stress Transfer Model Results 76
3.5.2.1 Rate/State Model in Stress Triggering Zones based on Optimally Oriented Fault Planes 77
3.5.2.2 Rate/State Model in Stress Triggering Zones based on Geometry of Nodal Planes of the Focal Mechanism Solutions 77
3.6 Discussion 78
3.6.1 Significance of Seismicity Rate Changes and Stressing Rate Changes due to SSEs .. 78
3.6.2 Limitations in investigating the relationship between SSEs and Regular Earthquakes 79
3.6.3 Triggering Effects on Seismogenic zone from the observed long-term SSEs in Alaska 79
3.7 Conclusion 80

3.8 Acknowledgements 81
3.9 Reference 81
Chapter 4 Spatial Variation of Slip Behavior beneath the Alaska Peninsula along Alaska-Aleutian Subduction Zone 102
4. 1 Abstract 102
4.2 Introduction and Background 103
4.3 Data 104
4.4 Method 105
4.5 Results 106
4.5.1 Slip Model for Sub-segments 106
4.5.2 Locating the Boundaries that Mark Sharp Changes in Locking 107
4.6 Discussion 108
4.6.1 Correlation between the Locking Distribution and the Plate Fabric from Magnetic Anomalies, and Subduction Seismicity 108
4.7 Conclusion 111
4.8 Acknowledgement 111
4.9 References 112
Chapter 5 General Conclusion 127
Appendices 130

List of Figures

Page

Figure 1.1 Map of Alaska showing the study region for each chapter in the thesis. 6

Figure 2.1 Topographic map and tectonic setting (inset) and study area in south-central Alaska (red outline in inset map). 29

Figure 2.2 Continuous (red) and campaign GPS sites (blue) in the study area. 30

Figure 2.3 Example of GPS time series in Lower Cook Inlet. 31

Figure 2.4 The spatial distribution of timing of velocity change for the continuous sites (a) and the general result for timing of velocity change at ~2010 (b) based on absolute difference of misfit for significant sites. 32

Figure 2.5 Comparison of the other two criteria used to determine which sites had significant velocity changes, for comparison to Figure 2.4. 33

Figure 2.6 The spatial distribution of timing of velocity change for the continuous sites (a) and the general result for the timing of velocity change at ~2011 (b). 34

Figure 2.7 Comparison between original GPS velocity data (left) and GPS velocity data with postseismic effect corrected for period 1: 1992.0-2004.8 (a, b). 35

Figure 2.8 Comparison between the original GPS velocity data and GPS velocity data with postseismic effect corrected for periods 2 (a, b), 3 (c, d) and 4 (e, f). 36

Figure 2.9 We used data from our main study area and also from the Alaska Peninsula in estimating the pole of rotation in the PENN (Peninsula) block. 38

Figure 2.10 The location of poles (blue dots) for all the blocks. 39

Figure 2.11 Predicted rotation velocities based on the pole estimated by inversion of the combination of data from periods 1 and 4. 40

Figure 2.12 Slip distribution result with different ϕ ranges of period 1. 41

Figure 2.13 The trade-off curves between Chi-squared value of data and roughness for four time periods. 42

Figure 2.14 Comparison between the predicted (blue) and observed (red) velocities for each time period. 44

Figure 2.15 Slip deficit rate distribution and residual of GPS velocities (white arrows) with the node geometry for ϕ in the range [-2, 1] (a) and ϕ [0, 1] (b) during the period 1 (1992.0-2004.8). 45

Figure 2.16 Slip deficit rate distribution and residual of GPS velocities with the node geometry for ϕ [-2, 1] (a) and ϕ [0, 1] (b) during the period 2 (2004.8-2009.85)..... 46
Figure 2.17 Slip deficit rate distribution and residual of GPS velocities with the node geometry for ϕ [-2, 1] (a) and ϕ [0, 1] (b) during the period 3 (2009.85-2011.81)..... 47
Figure 2.18 Slip deficit rate distribution and residual of GPS velocities with the node geometry for ϕ [-2, 1] (a) and ϕ [0, 1] (b) during the period 4 (2011.81-2014.87)..... 48
Figure 2.19 Model resolution from the checkerboard test. 49
Figure 2.20 Inferred slip deficit rate distribution for the proposed 9-year-long slow slip event (thick black polygon) in period 1 (1992.0-2004.8)..... 50
Figure 2.21 Inferred slip deficit rate distribution for the newly observed ~2 year long period slow slip event (thick black polygon) in period 3 (2009.85-2011.81). 51
Figure 2.22 Moment versus duration of slow slip events in the Lower Cook Inlet in periods 1 and 3 compared to some at other subduction zones. 52
Figure 3.1 Tectonic setting (inset) and study area in south central Alaska (red solid rectangle in inset map)..... 85
Figure 3.2 Spatial distribution of recorded earthquakes and focal mechanism solutions of the past earthquakes from the AEC catalog. 86
Figure 3.3 Changes in Coulomb stressing rate on OOPs due to SSE1 (a1 – a3) and SSE2 (b1 – b3) within three different depth ranges (0 – 30 km, 30 – 60 km, 60 – 90 km). 87
Figure 3.4 Correlation between CSRC on OOPs and seismicity rate change due to the SSE1 in areas selected by three thresholds (a-c) within 30 – 60 km depth range. 88
Figure 3.5 Correlation between CSRC on OOPs and in seismicity rate change due to the SSE2 in areas selected by three thresholds (a-c) within 30 – 60 km depth range. 89
Figure 3.6 Correlation between CSRC resolved on receiver faults based on observed nodal plane geometry (a) and seismicity rate change (b) in stress triggering areas within the 30 – 60 km depth range due to SSE1. 90
Figure 3.7 Correlation between CSRC resolved on receiver faults based on observed nodal plane geometry (a) and seismicity rate change (b) in stress triggering areas within 30 – 60 km depth range due to SSE2. 91
Figure 3.8 The rate/state stress transfer model results in the different stress triggering areas affected by SSE1 on OOPs (a-c correspond to three areas in Figure 3.4a – 3.4c). 92

Figure 3.9 The rate/state stress transfer model results in the stress triggering zones affected by SSE2 on OOPs (a-c correspond to three areas in Figure 3.5a – 3.5c). 93
Figure 3.10 The rate/state stress transfer model results in the stress triggering zones affected by SSE1 on nodal planes (a-c). 94
Figure 3.11 The rate/state stress transfer model results in the stress triggering zones affected by SSE2 on nodal planes 95
Figure 3.12 Correlation between Coulomb stressing rate change and seismicity rate change in an area affected by both SSEs based on the stress triggering areas in section 3.5.1. 96
Figure 3.13 Resolved Coulomb stress change on seismogenic zone due to four detected long-term SSEs in Alaska-Aleutian Subduction Zone (a) and Coulomb Stress Change due to SSEs along Two Profile Lines (1 and 2 in (a)) (b). 97
Figure 4.1 Tectonic setting and Observed GPS velocities for stations in the Alaska Peninsula. 116
Figure 4.2 Optimal Locking model, Observed and modeled GPS velocities and variation of the locking fraction in the downdip direction. 117
Figure 4.3 Correlation among fault locking, pre-existing plate fabric and subduction seismicity. 118
Figure 4.4 Best fitting model and selection of optimal locking ratios for each segment 119
Figure 4.5 Forward locking model (a) and observed versus modeled horizontal GPS velocities in the forward model (b) based on our best estimation of locking distribution in the four individual segments within the Alaska Peninsula. 120

Figure A.1 Time Series of GPS station AB07 in the Alaska Peninsula, detrended based on pre-SSE velocity 135
Figure A.2 (a) The location of poles (blue dots) for all the blocks used in this study and (b) a zoom in map of the study area outlined by purple rectangle in (a). 136
Figure A.3 Trade-off curve and best fit model for inverted locking distribution by using both GPS horizontal and vertical velocities 137
Figure A.4 The trade-off curve and effects of smoothing on the standard inversion model by using GPS horizontal velocities only. 138

Figure A.5 "Zebra stripe" test showing the spatial resolution of the inversion of GPS horizontal velocities only. 139

List of Tables

Page

Table 2.1 GPS site locations ("Longitude, Latitude"), velocities ("Ve, Vn") and associated uncertainties ("Se, Sn") in the horizontal ("east and north") component, the correlations ("Rho") and names ("Site") for time period 1 (1992.0-2004.8). 53

Table 2.2 GPS site locations ("Longitude, Latitude"), velocities ("Ve, Vn") and associated uncertainties ("Se, Sn") in the horizontal ("east and north") component, the correlations ("Rho") and names ("Site") for time period 2 (2004.8-2009.85). 56

Table 2.3 GPS site locations ("Longitude, Latitude"), velocities ("Ve, Vn") and associated uncertainties ("Se, Sn") in the horizontal ("east and north") component, the correlations ("Rho") and names ("Site") for time period 3 (2009.85-2011.81). 59

Table 2.4 GPS site locations ("Longitude, Latitude"), velocities ("Ve, Vn") and associated uncertainties ("Se, Sn") in the horizontal ("east and north") component, the correlations ("Rho") and names ("Site") for time period 4 (2011.81-2014.87). 61

Table 2.5 Block Poles, Location of Poles and Angular Speed of the block model, relative to the North American plate. 64

Table 2.6 GPS site locations ("Longitude, Latitude"), velocities ("Ve, Vn") and associated uncertainties ("Se, Sn") in the horizontal ("east and north") component, the correlations ("Rho") and names ("Site") for combined data set of periods 1 and 4 in the Alaska. 65

Table 2.7 The variance for the selected boxes in four time periods. 66

Table 3.1 CSRC thresholds and Magnitude of Completeness (Mc) used for different stress triggering areas based on three thresholds due to each event within 30 – 60 km on OOPs. 98

Table 3.2 CSRC thresholds and Magnitude of Completeness (Mc) used for the stress triggering areas selected based on three thresholds due to the two SSEs within 30 – 60 km on nodal planes. 99

Table 3.3 Z-value and its significance within the stress triggering areas affected by the two SSEs for receiver faults defined by nodal planes. 100

Table 3.4 Z-value and its significance within the stress triggering areas affected by the two SSEs for OOP receiver faults. 101

Table 4.1 GPS site locations, velocities and associated uncertainties in the horizontal (east and north) component and vertical component, and names. Velocities are based on the survey period (1992 - 2016)..... 121
Table 4.2 GPS site locations, velocities and associated uncertainties in the horizontal (east and north) component, and names for sites used in estimating the new pole for PENN block in Appendix A.2 (Survey period: 1992 - 2016). 124
Table 4.3 Block Poles, Location of Poles, and Angular Speed of the Block Model, Relative to the North American Plate. 126

Table A.1 Estimated East and North Components of GPS velocities for Co-Located Sites in Sand Point (SNDP, AB07 and LSDP). 140

List of Other Materials

Animations A.1 - A.6	Supplemental files

List of Appendices

Page

Appendix A Support Information for Chapter 4 130

Appendix B General Appendix 142

Acknowledgments

This thesis documents five years of hard research, but it would not have happened without the support of a number of people. First and foremost, I want to thank my advisor, Jeffrey Freymueller. He has taken the time to talk about projects and future possibilities, helped solve programming and modeling problems, read over many paper drafts, offered opportunities to attend the research conferences, workshops, and provided future career suggestions. I would not have been able to touch the beauty of research in geodesy and geophysics without his kind and patient instructions through the whole Ph.D study. I also learned from him to be a good and responsible person in my family. Thank you to my committee members, Douglas Christensen, Carl Tape and Mike West for your feedback, time, and meeting attendance and always being willing to offer me suggestions in doing research, communicating with people and future career development. Thank you for being patient when I felt lost during my research.

I would not have gained a great deal of field work experience without appreciated help from Jeff, Max Kaufman and my other colleagues: Kimber Degrandpre, Summer Miller, Xueming Xue and visitors from China: Kaihua Ding, Ming Hao and Jianjun Wang. Jeff and Max were responsible for collecting the GPS data and shared nice field pictures in my study area, though I could not go there.

I am indebted to my co-authors Robert McCaffrey, Jianjun Wang, and Natalia Ruppert for your thoughtful comments, suggestions, edits and feedback. Thank you to Robert for answering my questions about TDEFNODE over my Ph.D study and research in slow slip events. Thank you to Jianjun for providing brilliant suggestions in calculating Coulomb stress changes due to interesting events. Thank you to Natalia for providing instructions in using Zmap and the Alaska seismic catalog.

Thank you to Jeanne Sauber for your time, geoscience and life lessons, encouragement, and for being willing to be my referee when I applied for postdoc positions. Thank you for your patience to listen to my problems and show me the beauty of GPS and GRACE. You are an amazing and talented female scientist who I want to emulate in the future.

Thank you to my fellow grad students and friends for all the help in the office, fun times inside in the lab and outside, runs during winter and summer, all of which made my time in Alaska very pleasant!

Finally, I want to thank my parents and my grandparents for letting me travel a long distance away from home to do the things I want to do and for supporting my decisions always. Thank you to my husband, Heming Liao for always understanding, communicating with and supporting me and our family. Special thanks to my dear baby girl Miranda for joining our family at 9:40 am on May 30th, 2018 in Fairbanks, Alaska. She is the most precious gift that I ever had in my life. “Every time a child is born, a mother is born”.

Chapter 1

General Introduction

1.1 Background Review

A subduction zone is the place where two tectonic plates slowly move towards each other and an oceanic plate sinks beneath a continental plate. The largest recorded earthquakes worldwide so far have all occurred in subduction zones, such as the Mw 9.5 earthquake in Chile (1960), the Mw 9.2 earthquake in Alaska (1964) and the Mw 9.2 earthquake in Sumatra (2004). These giant earthquakes are shallow inter-plate underthrusting events that accommodate the motion of the two plates in the subduction zone. Compared with divergent and transform plate boundaries, subduction zones have larger seismogenic areas with stronger locking which produces greater magnitude earthquakes, and the deeper downdip extent puts seismic slip beneath the inland population regions. In a subduction zone, there can be a transition zone where "slow slip" occurs between the shallow locked zone (seismogenic zone) and the deep freely slipping zone. The "slow slip" is always presumed to be aseismic slip. Most earthquakes happen in the locked zone, while the slow slip behavior happens downdip of the locked zone. Even though the slow slip behavior is aseismic, it may promote the loading of asperities into the seismogenic zone and bring them closer to failure. The spatial and temporal behavior of the seismogenic zone in subduction zones are more dynamic and subject to changes in slip pattern than previously thought.

Slip behavior on the subduction megathrust interface during the interseismic period can provide significant insight into the elastic strain accumulation on the locked plate interface and slow strain release from the slow slip behavior (Savage, 1983). It is usually assumed that the locked fault interface accumulates elastic strain during the interseismic period and subsequent rupture in the next large or great earthquake. Even though the locked fault interface is usually located in the shallow region, not all the shallow plate interface is locked. Significant along-strike and downdip variations in the slip distribution are exhibited in the subduction zone globally. Understanding the cause of along-strike and downdip variations in slip behavior on the plate interface is important for better understanding the dynamic mechanical properties of the faults, and the rheology of the lower crust and lithosphere.

Repeated Global Position System (GPS) measurements enable us to observe the Earth's steady motion with an accuracy of better than one millimeter per year. These sites provide time

series of the ground deformation which allow us to track the changes of the Earth's movement in space and time. The slip distribution on the plate interface is closely related with the surface deformation in space and time. Increasingly dense GPS networks provide us a better opportunity to interpret the observable changes in data and relate them to changes in slip behavior on the interface, as well as to evaluate the stress changes acting on and caused by slip on the subduction megathrust.

Alaska is one of the most active tectonic environments on earth and has an abundant history and current record of great earthquakes, slow slip events (SSE), non-volcanic tremors and volcanoes, etc. The most significant driving force for Alaska tectonics is the subduction between the Pacific and North American plates (Alaska-Aleutian megathrust) along the southern Alaska margin and Aleutian Islands (Ruppert et al., 2008). The convergent boundary between the two plates extends for approximately 4000 km from the Prince William Sound in the east to the Komandorsky Islands in the west (Carver and Plafker, 2008). Over this long distance boundary, remarkable along-strike variations in plate convergence rates, crustal deformation, seismicity patterns, slip behavior on the megathrust interface and width of the seismogenic zone have been identified in the Alaska-Aleutian subduction margin. This suggests that the Alaska-Aleutian subduction zone is a premier location for such studies about the spatial and temporal variation in slip behavior and their possible cause and impact.

The combination of campaign and continuous GPS measurements reveals that the entire upper plate in the southern Alaska subduction zone is not moving as a "stable plate" and actually goes through internal deformation. A block model composed of several crustal blocks has been proposed in continental Alaska to explain the complex crustal motions, seismicity distribution and the deformation pattern depending on the increasingly dense GPS network and high precision GPS velocity field. The block model helps us better interpret the changes in slip on the plate interface and tectonic deformation over the earthquake cycle, further may improve understanding the cause and impact of the seismogenic zone in the subduction zones.

This thesis addresses the following main questions with a focus on the spatial and temporal variations in slip behavior on the plate interface by using GPS measurements:

1. What are the processes controlling slip behavior on the subduction plate interface?

2. When do SSEs start and stop and how do the long-term events migrate through space and time? Do adjacent events affect each other?

3. What is the relationship between aseismic slip (SSE) in the transition zone and seismic slip (fast earthquakes) in the seismogenic zone?

4. Are the seismicity rates influenced by Coulomb stress change rates due to SSEs?

5. What governs the size of earthquakes on the megathrust?

6. What controls the along-strike variations in the geometry of the seismogenic zone?

7. Do the estimated variations in slip behavior correlate with features on the overriding or downgoing plates, the reflection character of the plate interface itself, seismicity patterns, or other observables? What are possible correlations and causes of the observed variations?

To begin, a background review was given here, three chapters follow, each detailing my research projects, and finally chapters discussing conclusions and future work.

1.2. Thesis Structure

This thesis consists of three main science chapters along with this introduction and a general conclusion section. Figure 1.1 illustrates the regions studied in each chapter.

Chapter 2 was published in *Journal of Geophysical Research: Solid Earth* in 2016. This paper mainly focused on estimating the slip distribution from GPS velocities in four different time periods below the Lower Cook Inlet of the Alaska-Aleutian subduction zone, and then evaluating whether the changes in slip distribution indicate the occurrence of slow slip events or simply changes in the extent of the locked zone. A weighted non-linear least-squares inversion was applied to estimate the angular velocity of the Peninsula block (PENN) and estimate the plate coupling variation simultaneously using TDEFNODE (McCaffrey, 2009). Based on the estimated slip distribution from the four time periods, we were able to reconstruct the slip history on the megathrust interface beneath the Southcentral Alaska over the last 20 years.

Chapter 3 was submitted for publication in *Journal of Geophysical Research: Solid Earth* and tests whether the two long-term SSEs in Chapter 2 triggered earthquakes outside the slow slip area, and how the SSEs impacted stress in the Alaska-Aleutian subduction margin, especially in the seismogenic zone. The Coulomb stressing rate changes (CSRC) on receiver faults were computed using two possible fault geometry definitions: the nodal planes of focal mechanism solutions of past earthquakes, and optimally oriented fault planes. Stress changes were resolved from the inverted slip distributions for the two SSEs given in Chapter 2. The potential significant stress triggering areas were selected based on three different thresholds in the calculated CSRC values, and then tested for changes in seismicity rate during the SSE periods. After locating those

potential significant stress triggering areas by the SSEs, the modified rate/state model (Dieterich, 1994; Segall et al., 2006) was used to quantitatively model the ratio of the stressing rate during SSEs to the background stressing rate based on the ratio of seismicity rate during SSEs to the background seismicity rate. Generally, the main goal for this paper is to explore the questions 2-4 mentioned in section 1.1.

Chapter 4 is in press in the *Geophysical Research Letter* and addresses the questions 1, 5-7 mentioned in section 1.1. A denser and highly precise GPS velocity field has been estimated in the Alaska Peninsula, which features a dramatic along-strike transition from a widely locked region to a mainly creeping area on the plate interface (Fournier & Freymueller, 2007). This paper explores the locations and the length scales over which the dramatic along-strike and downdip variations occur more precisely, and explores the causes of these variations. The orientation of the plate fabric from magnetic anomalies, and patterns of subduction seismicity are explored to see whether there is any correlation with the estimated locking distribution, and what can be the possible mechanism to explain these correlations. Appendix A expands on Chapter 4 to show results about a specific example of GPS time series in the Alaska Peninsula, an updated pole of rotation for the PENN block, and a discussion about inversions using horizontal velocities only or both horizontal and vertical velocities.

Chapter 5 summarizes the findings of this thesis and presents an outlook on problems that need to be investigated in the future to improve on this work.

1.3 References

Carver, G., & Plafker, G. (2008). Paleoseismicity and neotectonics of the Aleutian subduction zone—An overview. *Active Tectonics and Seismic Potential of Alaska*, 43–63.

Dieterich, J. (1994). A constitutive law for rate of earthquake production and its application to earthquake clustering. *Journal of Geophysical Research: Solid Earth*, *99*(B2), 2601–2618.

Fournier, T. J., & Freymueller, J. T. (2007). Transition from locked to creeping subduction in the Shumagin region, Alaska. *Geophysical Research Letters*, *34*(6).

McCaffrey, R. (2009). Time- dependent inversion of three- component continuous GPS for steady and transient sources in northern Cascadia. *Geophysical Research Letters*, *36*(7).

Plafker, G., Moore, J. C., & Winkler, G. R. (1994). Geology of the Southern Alaska margin, Boulder, CO, United States (USA), Geological Society of America, Boulder, CO. *The Geology of Alaska*.

Ruppert, N. A. (2008). Stress map for Alaska from earthquake focal mechanisms. *Active Tectonics and Seismic Potential of Alaska*, 351–367.

Savage, J. C. (1983). A dislocation model of strain accumulation and release at a subduction zone. *J. Geophys. Res*, *88*(6), 4984–4996.

Segall, P., Desmarais, E. K., Shelly, D., Miklius, A., & Cervelli, P. (2006). Earthquakes triggered by silent slip events on Kīlauea volcano, Hawaii. *Nature*, *442*(7098), 71.

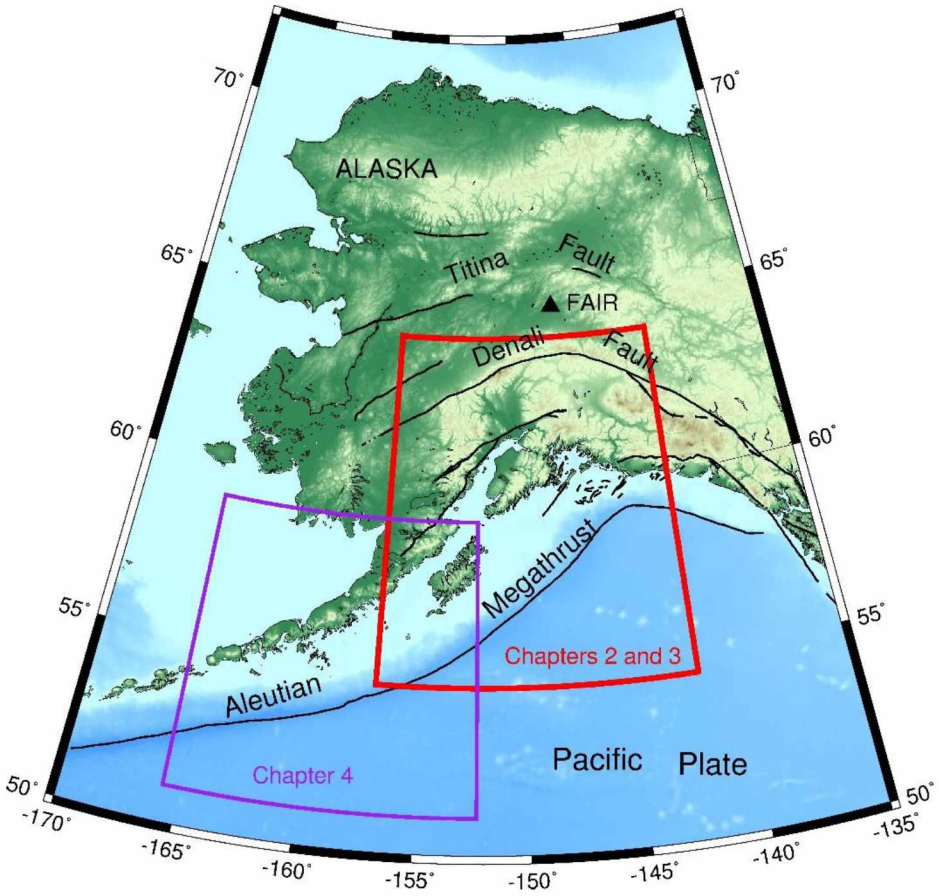

Figure 1.1 Map of Alaska showing the study region for each chapter in the thesis.Triangle shows Fairbanks (FAIR). (Fault Data from Plafker et al., 1994.) Red rectangle shows the study area, Lower Cook Inlet, for Chapters 2 and 3. Purple rectangle shows the study area for Chapter 4, the Alaska Peninsula including the Shumagin and Semidi segments.

Chapter 2

Slow slip events and time-dependent variations in locking beneath Lower Cook Inlet of the Alaska-Aleutian Subduction Zone[1]

2.1 Abstract

We identify a series of abrupt changes in GPS site velocities in Lower Cook Inlet, Alaska, in late 2004, early 2010, and late 2011. The site motions during each time period, are nearly linear. The surface deformation inferred from GPS for pre-2004 and 2010-2011 are similar to each other, as are 2004-2010 and post-2011. We estimate the slip distribution on the Alaska-Aleutian subduction plate interface accounting for upper plate block rotations, and interpret this toggling between two deformation patterns as caused by transient slip. We find that by allowing negative slip deficit rates (i.e.., creep rates in excess of relative plate motion), the data in Lower Cook Inlet are fit significantly better during pre-2004 and 2010-2011, suggesting the occurrence of slow slip events (SSE) there during those time periods. The earlier SSE lasted at least 9 years (observations in that area began in 1995) with M_w~7.8. The latter SSE had almost the same area as the earlier one, and a duration of ~2 years with M_w~7.2. During 2004-2010 and post-2011, the inversions result in only positive slip deficit rates (i.e., locking) in Lower Cook Inlet. Slip rates are nearly constant during the Lower Cook Inlet SSEs, and the events start and stop abruptly. Both of these properties contrast with observations of SSEs in Upper Cook Inlet and elsewhere. The Lower Cook Inlet SSEs are consistent with previously proposed duration-magnitude scaling laws and demonstrate that slow slip events can last as long as a decade.

---

[1] Li, S., J. Freymueller, and R. McCaffrey *(2016)*, Slow slip events and time-dependent variations in locking beneath Lower Cook Inlet of the Alaska-Aleutian subduction zone, *J. Geophys. Res. Solid Earth*, 121, 1060–1079, doi: 10.1002/2015JB012491.

2.2 Introduction and Background

2.2.1 Objective

Slow slip events (SSEs) are episodes of slip on a fault that are slow compared to the slip rates of normal earthquakes but fast compared to long-term fault slip rates. The basic description of an SSE is that a previously locked section of the fault slips for a while at a rate faster than plate motion, then locks up again at the end of the event (Dragert et al., 2001). Unlike continuous steady creep, slow slip events (SSEs) occur with a finite duration and can involve fault slip rates that are faster than long-term relative plate motion. Considerable variability has been observed in the duration, magnitude, slip amount, and slip rate of SSEs (Schwartz & Rokosky, 2007). Studies of SSEs provide significant insights into the dynamic mechanisms and physical conditions on the subduction plate interface (Peng & Gomberg, 2010).

Interseismic crustal deformation caused by the interplate locking on a subduction megathrust can be described using the basic model proposed by Savage (1983). It is modeled as the sum of steady reverse slip representing the plate convergence and normal slip (back slip) to represent the slip deficit distribution on the plate interface. The interseismic velocity field can provide detailed information about the distribution of the slip deficit on the plate interface. The slip deficit over some time interval is defined as the expected slip on the plate interface (from plate motions) minus the actual slip. There are four different states of interplate locking on the plate interface (Ochi & Kato, 2013): fully locked, partially locked, fully slipping, and overslipping. Fully locked indicates that there is no slip on the boundary so the slip deficit rate equals the plate convergence rate. Fully slipping means there is no slip deficit, as the slip rate on the interface is equal to the plate convergence rate. Partially locked indicates that the locking rate is lower than plate convergence rate. Finally, the state of overslip would occur if the slip rate on the fault is faster than the plate convergence rate and may indicate the occurrence of the slow slip events (Ochi & Kato, 2013). Here we examine the state of slip on a part of the Alaska megathrust and how it changes through time.

2.2.2 Tectonic Setting

South-central Alaska is a tectonically active region that features subduction, great earthquakes and active volcanoes. The Alaska-Aleutian subduction zone, where the Pacific plate subducts beneath the North American plate (Figure 2.1), has the shallowest dip, close to 3 degrees below the Kenai Peninsula, of any subduction zone in the world (Ohta et al., 2006). At the eastern

end of the subduction zone, a triangular-shaped block called the Yakutat Terrane is colliding with Alaska, producing a collisional boundary between the subduction at the Aleutian megathrust and the Queen Charlotte-Fairweather transform fault (Elliott et al., 2013). The exceptionally shallow dip of the subduction zone is related to this transition from simple subduction to collision. The convergence rate of the Pacific plate relative to North America increases from ~55 mm/yr near south-central Alaska to 60 mm/yr along the Alaska Peninsula; in south-central Alaska the convergence vector is rotated $\sim 17^{o}$ clockwise relative to the trench-normal direction, while subduction is trench-normal along the Alaska Peninsula. The upper plate in Alaska is characterized by major active faults like the Denali fault (Figure 2.1), and all of southern Alaska moves relative to the stable North American plate (Freymueller et al., 2008). Several great earthquakes and long-term slow slip events have happened along the Alaska-Aleutian subduction zone. The 1964 earthquake (M_w9.2) (Cohen & Freymueller, 2004) ruptured the eastern section of the subduction zone (purple outline in Figure 2.1), and its postseismic deformation continues today (Suito & Freymueller, 2009).

2.2.3 Previous Work

Slow slip events (SSE) with durations from days to years have been observed in many subduction zones. The largest SSEs on the Cascadia subduction interface last days to weeks, are estimated to have ~2 centimeters of aseismic slip over the interface downdip from the seismogenic zone and moment magnitudes of ~6.7 (Dragert et al., 2001; Szeliga et al., 2004). These and all other magnitudes in this paper are estimated from geodesy, and the moments depend on the assumed shear modulus; we assume 50 GPa for the Lower Cook Inlet event. Kostoglodov et al. (2003) observed a large SSE in southern Mexico lasting about 6-7 months in the Guerrero seismic gap, with average slip of ~10 centimeters and Mw ~7.5. Several short-term and long-term slow slip events were observed in southwest and central Japan. For example, a long-term SSE occurred in the Tokai region from 2000 to 2005 with the maximum slip rate about 20 mm/yr faster than plate motion rate (overslip), and a moment magnitude of M_w~6.6 (Ochi & Kato, 2013). Some short-term slow slip events have been detected along the Nankai Trough in southwest Japan with moment magnitudes ranging from 5.5 to 6.3 (Nishimura et al., 2013). At least 15 SSEs have occurred at the Hikurangi subduction margin since 2002; the durations of these events varied from 6 days to 1.5 years with moment magnitude ranging between M_w 6.3-7.2 (Wallace & Beavan, 2010).

In Alaska, Ohta et al. (2006)discovered a large slow slip event from 1998 to 2001 below Upper Cook Inlet within the south central Alaska subduction zone. Fu & Freymueller (2013) identified a second slow slip event from 2008.96 to 2012.87 in the same area as 1998-2001 SSE, and Wei et al. (2012) identified another SSE that occurred beneath Lower Cook Inlet from 2010 to 2011 located southwest of the 1998-2001 SSE.

2.2.4 Present Study

We relate the observations of abrupt changes in GPS site motions in late 2004, ~2010 and ~2011 around the Lower Cook Inlet region to changes in the slip distribution on the plate interface.

We augment the sparse continuous GPS data from 1996 through 2014 with repeat surveys of campaign GPS sites starting in the 1990s to the end of 2014 to better estimate the velocity changes. As described below, we divide the GPS time series into four time periods based on the observed changes in trends at ~2004, ~2010 and ~2011. Using the horizontal components of the GPS velocities, we estimate the slip variations below the Lower Cook Inlet of the Alaska-Aleutian subduction zone for each period and then evaluate whether they indicate the occurrence of slow slip events or changes in the extent of the locked zone. Meade & Loveless (2009) proposed that very long-duration SSEs would have slip rates comparable to plate motion rates, which would make them difficult to distinguish from partial locking. However, rates of slip on the interface faster than plate motion, aside from postseismic transient effects, can only result from SSEs. Therefore, we assume that the presence of overslip as described above requires an SSE.

2.3 GPS Data and Analysis

2.3.1 GPS Data and Characteristics of the time series

We estimate the slip deficit distribution on the plate interface and its time dependence by using 65 continuous and 107 campaign GPS sites in total (Figure 2.2). GPS sites located on or near active volcanoes were not used.

We use the GIPSY/OASIS goa-5.0 software developed by Jet Propulsion Laboratory (JPL) to obtain daily coordinate and covariance estimates for all the GPS continuous and campaign stations around the Cook Inlet region. We adopt the JPL non-fiducial orbits and clock products, derived from a free network solution, and estimate a daily transformation for each solution into the ITRF2008 reference frame. The details of the data analysis were described in Fu et al. (2012).

The GPS time series reveal abrupt changes in slopes (velocities) in Lower Cook Inlet of the Alaska-Aleutian subduction zone in late 2004, early 2010 and late 2011 (Figure 2.3a). There

were only two continuous GPS sites operating in the area prior to 2004. Site SELD in Seldovia (Figure 2.2), set up in 2000 (Figure 2.3b), reveals a velocity change in the north component at about 2004 (Figure 2.3b and Figure 2.3c). A small offset in the east component at ~2006.4 is due to an antenna change. The north components of the time series of several other continuous and campaign sites around the study area (examples shown in Figure 2.3a), also reveal velocity changes at ~2010.0 and ~2011.0. Relative to the 2004.8-2010 velocities, sites in the study area generally moved faster southward prior to 2004.8, and did so again from early 2010 – late 2011 (Figure 2.3a). Post-2011 motions are similar to those of 2004.8-2010, or are slightly more northward. Site KEN1 in Nikiski (Figure 2.2) has a similar timing of velocity change as SELD, but the change is smaller and including KEN1 does not improve the estimate of the timing. The timing of the velocity changes are examined in the following section.

2.3.2 Estimating Timing of Velocity Change

To estimate the timing of the velocity change in late 2004, we first de-trend the time series from SELD (Figure 2.3b) based on the pre-2004 velocity. It is evident that the site moved faster to the north after late 2004. We then fit the time series assuming an abrupt velocity change, as well as offsets in 2002 for the Denali fault earthquake and in 2006 for a receiver/antenna change. We test a series of dates for the timing of the velocity change by least-squares fit to the positions. There is a broad minimum in the misfits between mid-2004 and mid-2005 (Figure 2.3c) while the minimum is at 2004.8. The pattern of the velocity changes is consistent with an expansion of the downdip width of the locked zone on the plate interface after ~2004.8, as it is the elastic deformation from the locked zone that causes motion in a roughly northward direction here.

To estimate the specific timing of velocity changes in ~2010 and ~2011, we use the time series from 23 continuous sites around Lower Cook Inlet and the same approach described above for SELD. Unlike for the 2004.8 change, the test for the timing of the velocity change reveals a narrow minimum in the misfit for each individual site. However when all sites are combined, the minimum in the misfit is broader because the specific date of the velocity change varies from site to site, likely due to migration of the slip on the plate boundary. Therefore, we fit each site independently and use only those sites that have significant changes in velocity to estimate the best time to use. We test thresholds based on three different criteria of significance of the velocity change: the relative difference of the data misfit, the absolute difference of data misfit and the magnitude of velocity change. We find that the second criteria, the absolute difference of the misfit,

produces the most spatially coherent set of sites with significant changes (Figure 2.4, Figure 2.5 and Figure 2.6).

After removing the sites that show no significant velocity change based on each of the criteria, we map the spatial distribution of the timing of the velocity changes (Figure 2.5). For the change at ~2010.0, it appears that the velocities of sites over deeper parts of the plate interface (downdip) changed first and then the sites to the SE (updip) changed later (Figure 2.4a). Based on the selected significant sites (Figure 2.4), the mean timing of velocity change at ~2010 is at 2009.85.

We apply the same approach for estimating the timing of velocity change in 2011 and find the average of 2011.81 (Figure 2.6). For this velocity change, the updip sites changed first and then the velocity change gradually propagated towards the downdip sites, opposite the direction of propagation in early 2010.

2.3.3 GPS Velocities

Based on the estimates of the velocity changes in late 2004, ~2010 and late 2011 as determined above, we divide the GPS time series into four time periods: period 1 (1992.0-2004.8), period 2 (2004.8-2009.85), period 3 (2009.85-2011.81), and period 4 (2011.81-2014.87). For almost all sites, the data span used by Suito & Freymueller (2009) is the same as our period 1 because there were only a few campaign measurements made between 2004 and 2009.

We use only the horizontal GPS velocities for estimating the interseismic slip distributions because of the high uncertainties in the vertical component and large vertical deformation due to glacial isostatic adjustment (GIA). We calculate GPS velocities from individual site time series by weighted least-squares using all data from each period and correct the velocities for the estimated geocenter translation rate of the ITRF2008 based on Altamimi et al. (2011). Then we remove the motion of North America in ITRF2008 to transform velocities into a North America fixed reference frame (Argus et al., 2010) and apply GRACE-derived seasonal variation corrections (Fu et al., 2012) to the continuous and campaign GPS time series.

The GPS velocity field (Tables 2.1-2.4) reveals strong along-strike and across-strike gradients (Suito & Freymueller, 2009). Outside of the Cook Inlet region, the velocity fields for all four time periods are similar, differing mainly in the sites available. Velocities close to Prince William Sound are generally higher than those on the Kenai Peninsula. The sites far from the trench tend to move trenchward while the sites closer to the trench move in the direction of relative

Pacific plate motion (Figure 2.7). Postseismic deformation from the 1964 earthquake causes the trenchward motion while elastic deformation from locking on the subduction interface causes motion in the direction of plate motion (Suito & Freymueller, 2009). We remove the postseismic deformation using the model of Suito & Freymueller (2009) to isolate the interseismic deformation. We minimize the effect of postseismic deformation from the 2002 Denali earthquake by using only sites located well to the south of the Denali fault. This selection is based on the predictions of existing postseismic models (Freed et al., 2006; Johnson et al., 2009), which predict negligible postseismic displacements in our study region, except for the northwest corner.

Figure 2.7 shows the comparison between original GPS velocities and GPS velocities with postseismic deformation removed for periods 1 (a, b). The same information for periods 2, 3 and 4 are shown in Figure 2.8. The trenchward postseismic motion from the original velocity field, disappears when the postseismic model is subtracted from the data, especially in the west and northwest part of the study area.

2.4 Modeling Approach and Evaluation

2.4.1 Block Model

The entire upper plate in the southern Alaska subduction zone moves relative to North America (Freymueller et al., 2008) and we must account for this motion via a block model to avoid biasing the estimated slip distribution on the megathrust. Estimating the motion of all of the upper plate blocks would require using GPS velocities from a much larger area and accounting for additional complications that are not relevant to the main topic of this paper. Therefore, we first develop a block model using mostly published sources, and keep that model fixed for investigation of the time-dependence of slip on the plate interface.

Lahr & Plafker (1980) proposed a model for the tectonics of southern Alaska comprising three blocks: the Wrangell block, the St. Elias block and the Yakutat block. Relative motion rates in their model were educated guesses, which turned out to agree fairly well with later geodetic data (Freymueller et al., 2008). Fletcher (2002) improved the Lahr & Plafker (1980) relative block motion rates based on the GPS data available at that time but used different block names: the southern Alaska block (SOAK) instead of the Wrangell block, and the Fairweather block instead of the St. Elias block. In Fletcher (2002), the pole of rotation for SOAK relative to the North American Plate (NOAM) was based on the fit of a small circle to the trace of the central Denali fault. The angular speed of the SOAK block (Table 2.5) was calculated by estimating the average

slip rate on the Denali fault from the available GPS data at that time (Fletcher, 2002; Freymueller et al., 2008).

Cross & Freymueller (2008) discovered that sites in western Alaska and on the Bering Sea Islands have southward or southwestward velocities relative to NOAM. These velocities were well-fit by a single clockwise rotation about a pole located in northeast Asia. They called this block the Bering plate (BRNG), although they could not define its eastern boundary (Figure 2.1), and proposed that the Alaska Peninsula lay on the Bering plate. Suito & Freymueller (2009) suggested that the systematic residuals of sites on the Kenai Peninsula relative to the interseismic model result from westward block motion relative to both SOAK and NOAM. These residuals are similar to the motion of sites on the Alaska Peninsula from Cross & Freymueller (2008). Given that and the lack of a clear tectonic boundary between the Alaska Peninsula and the Kenai Peninsula, we test a model with an additional Peninsula block (PENN) that includes both regions. Our model uses the SOAK block from Fletcher (2002), BRNG (Cross & Freymueller, 2008), the PENN block, and two major plates: NOAM and the Pacific plate (PCFC) (Sella et al., 2007) (Figure 2.1). We estimate the angular velocity of PENN, but fix the poles of all the other plates and blocks at their published values (Table 2.5). We also test a recently published PCFC-NOAM pole (DeMets et al., 2014). That pole produces a slower convergence rate at the Alaska trench and the model residuals approximately double if we use it in place of the Sella et al. (2007) pole because the observed strain in the upper plate cannot be matched even with a wide fully locked interface. Therefore, we use the estimate from Sella et al. (2007) in this paper.

2.4.2 Estimation of Angular Velocity of PENN Block

We estimate the pole of rotation of the Peninsula Block (PENN) by using GPS sites in the periods 1 and 4 because there are more sites with precise velocities in period 1 (due to its long duration), and period 4 has the second best distribution of sites and the most continuous sites. Compared with periods 1 and 4, period 2 has very few campaign sites, and period 3 spans only 2 years (resulting in large uncertainties). We find that the data from these latter two time periods are consistent with the angular velocity of PENN estimated from periods 1 and 4.

The subducting plate geometry beneath southern Alaska is complex due to the transition from Pacific plate subduction to Yakutat terrane collision. Brocher et al. (1994) suggested that there were actually two separate subduction interfaces beneath Prince William Sound, Yakutat subducting beneath North America, and Pacific subducting beneath Yakutat. In this paper we use

the Slab 1.0 plate geometry (Hayes et al., 2012), which is considerably deeper (by as much as 15-20 km beneath Upper Cook Inlet) than the slab geometry assumed in previous studies (Suito & Freymueller, 2009). The slab geometries are more similar in Lower Cook Inlet, and are essentially the same from Kodiak Island to the west. Assuming a shallower plate interface would reduce the estimated magnitude of slip in the slow slip events because the interface is shallower (less slip is needed to cause the same deformation at the surface), but for this study we retain Slab 1.0 because it is not yet clear which geometry is more accurate.

After removing the 1964 earthquake postseismic effect from the horizontal GPS velocities, they can be expressed as a combination of block rotations and the elastic deformation from locked faults, including the Denali fault and the subduction megathrust. We perform a non-linear, constrained, least-squares inversion to estimate the pole of rotation of the PENN block and the plate locking variation simultaneously using a simulated annealing approach (Press, 1989) in the program TDEFNODE (McCaffrey, 2009). All other block angular velocities are fixed to the values in Table 2.5. Details of the block boundaries will be described in section 2.4.3. The site velocity is equal to:

$$v_i(x_{site}) = v_B - v_{SD} = \Omega \times x_{site} - v_{SD} \quad (2.1)$$

$\boldsymbol{v_B}$ is the velocity at the site due to block rotation, $\boldsymbol{v_{SD}}$ is the surface velocity related to the fault slip deficit distribution, $\boldsymbol{x_{site}}$ is the vector pointing from the earth center to the surface observation point, and Ω is the angular velocity of the block that contains the site relative to the reference plate NOAM. The slip deficit rate on the megathrust is parameterized using a spatially variable coefficient ϕ, multiplied by the relative plate velocities determined from the block angular velocities projected on to the fault plane. The details of the calculation approach of TDEFNODE are given in McCaffrey (2002); [http://web.pdx.edu/~mccaf/www/defnode].

We estimate the angular velocity of the PENN block based on the approach outlined above by using three different velocity sets: period 1 only, period 4 only and a combination of periods 1 and 4. In the solution using the combination, we use the average velocity and its corresponding uncertainty if a site was present in both time periods. All three inversions produce a similar solution for the PENN block, so we adopt the solution for the angular velocity of the PENN block (Table 2.5) estimated from the combination of GPS velocities from periods 1 and 4 (Table 2.6). We use data from our main study area and also from the Alaska Peninsula; see Figure 2.9 for the

observations and model predictions from this inversion. Figure 2.10 shows the location of poles for all the blocks in the block model. The estimated block rotation velocities for sites on the PENN block have clear southwestward motion (Figure 2.11). For the remainder of this paper, we will keep the angular velocity of PENN fixed while we estimate the slip deficit distributions.

The location of the pole for the PENN block is quite sensitive to small changes in the data used in the inversion, although the predicted block motion velocities are not. The best fit pole for the PENN block is located in northern Russia, but if we use data only from the main study area (Cook Inlet), then the pole shifts to a location south-southeast of Alaska, in the Pacific Ocean (Figure 2.10). A great circle connecting these two poles passes through the center of the PENN block itself, and both poles give nearly identical trench-parallel velocities over the limited area of the PENN block (one pole has clockwise rotation, and the other counter-clockwise). There are small differences in the trench-normal motions predicted by these two poles, but only about 0.5 mm/yr, and the small difference changes the estimated slip distribution only slightly. Therefore, the predicted block motions are well determined even if the pole of rotation is not, and we use the PENN pole based on the larger data set.

2.4.3 Modeling of Slip Deficit Rate Distribution

We use TDEFNODE (McCaffrey, 2002, 2009) to estimate the block-bounding fault slip deficit rate distributions for each time period by inverting the GPS velocity data. We then interpret variations in the slip deficit rate distribution in terms of locking variations and transients such as slow slip events. For these inversions, we fix the block motions per Table 2.5.

TDEFNODE combines spherical block rotations with interseismic locking distributions on the faults using the halfspace dislocation method (Okada, 1985). The main faults that define boundaries in the model are the central Denali fault and the Aleutian subduction zone based on mapped fault segments. All blocks must be closed polygons, and arbitrary boundaries were used far from the data used here to do that. The subduction zone geometry is based on the slab1.0, a three-dimensional representation of the Alaska-Aleutian subduction zone (Hayes et al., 2012) (Figure 2.1). The Aleutian slab geometry based on slab1.0 is digitized about every 35 km in the along-strike direction and about every 5 km in the downdip direction. The locations of the irregular grid of nodes on the fault surface are specified by their latitude, longitude and depth producing a continuous fault geometry. The coupling fraction ϕ (ratio of the slip deficit rate to the long-term slip rate) is estimated at each node subject to spatial smoothing as described below. The fault slip

rate and rake are determined by the relative block motions, so the single parameter ϕ fully accounts for the slip deficit rate.

We place bounds on the allowed values of ϕ (slip deficit fraction) and estimate the slip deficit distribution subject to additional smoothing constraints. Negative values of ϕ imply an excess of slip (overslip), where the slip rate exceeds the plate motion rate and would indicate the presence of a slow slip event. Slip rates during SSE at other subduction zones can be many times the plate convergence rate. For example in Cascadia a typical average rate is about 500 mm/yr (~1 cm/week) which is more than 10 times the convergence rate. To find out whether or not negative slip deficit rates are required in our region, we apply several different bounds on the coupling ratio ϕ: [-100, 1] (Figure 2.12a), [-2, 1] (Figure 2.15a or 2.12c), [-1, 1] (Figure 2.12b) and [0, 1] (Figure 2.15b) where the brackets indicate minimum and maximum values allowed. Comparing the slip distributions from these different ϕ ranges (Figure 2.12), we find that minimum slip deficit rate in the setting of ϕ: [-100, 1] was almost the same with the one obtained by restricting ϕ to the range [-2, 1] for all reasonable amounts of smoothing. The minimum ϕ value from ϕ: [-2, 1] tended to be smaller than the one from ϕ: [-1, 1] although differences in these slip distributions are mainly in areas of poor model resolution. We also find that ϕ values observed in other SSEs in Alaska (Ohta et al., 2006) were close to -1. Therefore a ϕ range of [-2, 1] allows for reasonable slip rates for the long-term SSEs observed here. In addition to fixing the allowable ϕ range as [-2, 1], we also fix the coupling ratio to 0 at the deepest nodes (deeper than 70 km) on the fault because we assume fully slip occurs at these depths. ϕ values at the shallowest nodes are not constrained. We use a starting value of zero for all ϕ values.

The estimation of the slip distribution as we pose it is mixed-determined, so we apply Laplacian smoothing with the same smoothing factors in both the along-strike and down-dip directions. We find the optimal trade-off between the data misfit based on the weighted residuals $r^T W r$ and the model roughness defined by Laplacian of the slip distribution, and minimize the sum of these two quantities F (Equation 2.2).

$$F = \mathrm{r}^T \cdot \mathrm{W} \cdot \mathrm{r} + \frac{A \cdot \left(\frac{\partial^2 \phi}{\partial x^2} + \frac{\partial^2 \phi}{\partial w^2}\right)}{n} \quad (2.2)$$

The first term in the Equation 2.2 includes the residuals r, and W is the weight matrix, the inverse of the data covariance matrix. The second term will be called the roughness of the model, where

A is the smoothing factor (weight) for both along-strike and downdip directions, ϕ is the locking fraction, x is along strike, and w is along the dip direction, and n is the number of free nodes on the fault surface. Varying the smoothing factor A generates a series of solutions where the curvature of the locking pattern is damped (Figure 2.13). After analyzing the trade-off curves for each time period, we find that the optimal ranges of the smoothing factor are similar for all four time periods. Thus we choose the same preferred smoothing factor for four time periods, $A = 1 \cdot 10^7$.

2.5 Results

2.5.1 Model Prediction vs. Observed Velocity Data in the four time periods

For each time period, we fix the angular velocities of all blocks and estimate the fault slip deficit distributions using TDEFNODE, with the slab geometry and smoothing given in the previous section. Figure 2.14 shows the observed and calculated GPS velocities for each time period using the ϕ range [-2, 1]. The model fits the velocities well in general, except for within Prince William Sound (for all time periods). The residuals in Prince William Sound will be discussed at the end of the next section.

2.5.2 Slip distribution in each time period

We estimate locking for each time period with two different limiting ranges of the locking fraction (ϕ): [-2, 1] and [0, 1]. Slip rates faster than the plate convergence rate ($\phi < 0$) are interpreted as slow slip events, while ϕ values that change but remain positive may correspond to SSE or temporal changes of the locking. Figures 2.15-2.18 show the fault slip deficit distributions and residuals for both ranges of ϕ for each time period. The distribution of slip deficit is similar in all time periods for the shallow parts of the fault (at least below the areas where there are data and hence resolution). However, while the first order pattern is similar through time, there are large differences between the periods at the downdip limit of the locked region. To test whether slip rates faster than the plate convergence rate are required to satisfy the data, we calculate and compare the sum of squares of the weighted residuals (variance) between the two different solutions for each time period, using data from the sites in the area that shows a significant change in the slip deficit rate (Table 2.7). The differences in misfit when the bounds on ϕ were changed were large for periods 1 and 3, but small for periods 2 and 4.

Based on the residual variance in the same selected area (red box in Figures 2.15-2.18), negative slip deficit rates identified in period 1 (1992.0-2004.8) and period 3 (2009.85-2011.81)

fit better compared to a model with only positive slip deficit rates. For periods 1 and 3, the variances of residuals are reduced by about 64% and 74% respectively by allowing negative ϕ values in the red box area (Figures 2.15-2.18). For the other two time periods, the differences in variance are much smaller which are both less than 20%. For this paper, we consider the >50% reduction in misfit for periods 1 and 3 to be significant, requiring that slip on the interface exceeded the rate of plate motion. This significant overslip requires the occurrence of slow slip events during period 1 and period 3 (Ochi & Kato, 2013). The lower Cook Inlet slow slip event during period 1 lasted at least 9 years, given that our observations in that area began in 1995, and the pattern of site velocities was nearly constant from 1995 to 2004. We discuss the long duration of the slow slip event, the slip distribution pattern and locking distribution on the fault in section 2.6. For periods 2 and 4, allowing slip to be faster than plate motion does improve the fit to the data, but the improvement is much less convincing in the Lower Cook Inlet area. In particular, in period 4 the improvement in misfit in the Lower Cook Inlet area is only 7% if we allow slip faster than plate motion.

The blue box in Figure 2.15, outlines the area of the known 1998-2001 Upper Cook Inlet SSE, is drawn based on the model of Ohta et al. (2006). The time periods chosen in this study are based on the observed changes in motion in lower Cook Inlet, which are not synchronous with the SSEs in Upper Cook Inlet. For example the 1998-2001 SSE lies within our period 1, but is averaged together with an equal or greater length of time with no SSE. As a result, we do not recover the full amplitude of the SSE. The later 2009-2013 SSE (Fu et al., 2015; Fu & Freymueller, 2013) is divided across three of our time periods, and as a result it has almost no impact on period 2 and a reduced impact on period 4, which includes two years of data after the SSE. It can still be clearly seen in Figures 2.17a and 2.18a. An inversion for a time series of slip deficit based on the GPS time series, rather than velocities, will be needed to study both regions at the same time and to assess the temporal relationship between nearby events more fully.

Observed velocities near Prince William Sound are systematically under-predicted for all time periods even though ϕ is at its maximum value (fully locked) in this area. We test two alternate models to evaluate two possible explanations for these systematic residuals: (a) our assumed plate geometry is too deep, and (b) the sites in Prince William Sound lie on a block separate from PENN. The region just to the east of our study area has several upper plate blocks (Elliott et al., 2013), but none of them can explain the residuals. Making the subduction geometry

shallower using the geometric model of Suito & Freymueller (2009) decreases the misfit in Prince William Sound by ~24% but results in only small changes elsewhere (this model of the plate interface is as much as 10-15 km shallower than Slab 1.0 along a cross-section passing through Prince William Sound). Adding a new block for Prince William Sound produces a larger improvement in the misfit in that area, ~35%, but again very small changes in the model elsewhere. Adding a block for Prince William Sound does not change the estimated slip deficit distribution except immediately over Prince William Sound, but making the plate interface much shallower reduces the size of the estimated locked area in general and reduces the magnitude of inferred forward slip in the slow slip events. We retain the original geometry and block model for the results shown here, but note that the inferred moment magnitudes of all SSEs in the region from this study, Wei et al. (2012) and Fu & Freymueller (2013) might be overestimates if the active plate interface is much shallower than Slab 1.0.

2.5.3 Model Resolution

To reveal the sensitivity and resolution of our inversion method, we conduct a synthetic checkerboard test. We run a forward model with starting ϕ values of either one or zero in a checkerboard pattern (Figure 2.19a) and add random errors with the same variance as those of the observed velocities to the calculated velocities at each site. We then invert the synthetic data using the same inversion settings as our best inversion models. The recovered model (Figure 2.19b) reproduces the test model well for the area where GPS stations are most dense, on land and immediately offshore. Model resolution is good for the Lower Cook Inlet area, but minimal in the near-trench region. The original model is recovered faithfully for the region of slow slip, at the downdip end of the locked zone. The lack of resolution near the trench, and offshore in general, is not surprising given the long distance from the shoreline to the trench. However, the onshore part of the seismogenic zone is resolved well.

2.6 Discussion

2.6.1 Interseismic slip deficit distribution and reconstruction of slip history over the last 20 years

The slip deficit rate distribution for period 1 based on ϕ in the range [-2, 1] in Figure 2.15 shows two significant patches of overslip: one is below the upper Cook Inlet area, known to be the area of a large 1998-2001 SSE (Ohta et al., 2006); the other one is mainly over the depth range of 36-60 km in the Lower Cook Inlet area. These two overslip patches indicate two separate SSEs during period 1. Figure 2.17 shows the slip deficit rate distribution for the two different ϕ ranges

for period 3, which indicates an area of overslip over the depth range of 36-56 km in the Lower Cook Inlet area, also presumed to be a ~2 year-long SSE (Wei et al., 2012). Period 2 (Figure 2.16) has a small area of overslip in Lower Cook Inlet, in the same place as the SSE in period 1, which could be a remnant of that SSE. However, the model in which only positive slip deficit is allowed only increases the misfit by 20%, so the evidence for slip faster than plate motion is less clear than for periods 1 and 3. Period 4 (Figure 2.18) has no active SSE in Lower Cook Inlet, but a clear area of overslip in Upper Cook Inlet, which is the SSE identified by Fu & Freymueller (2013). The slip deficit rate distribution in period 4 tends to be better determined than the distribution in period 2 because of the much better data constraints. Changes in the slip pattern can be seen more clearly by differencing the slip deficit distributions of two time periods. We adopt period 4 as the best estimate of the steady deformation (no SSEs in Lower Cook Inlet), and subtract its slip deficit rate distribution from that of the SSE periods (periods 1 and 3) to isolate the changes in the slip deficit distribution related to the SSEs (Figures 2.20 and 2.21). Here we focus mainly on the newly discovered SSE in Lower Cook Inlet as the Upper Cook Inlet events were studied recently (Fu et al., 2015; Fu & Freymueller, 2013). As noted earlier, our division of the time series into 4 periods based on the velocity changes in Lower Cook Inlet is not ideal for the study of the Upper Cook Inlet SSEs, because the timing of events in the two regions is different.

Considering the model resolution limits, the areas of the SSEs in periods 1 and 3 may be the same; certainly there is significant overlap between the two slip regions (Figure 2.20). Both are located underneath the southwestern Kenai Peninsula, with the updip and downdip limits being close to the Pacific and Cook Inlet shorelines, respectively. The earlier event may extend slightly farther to the northeast, while the later event may extend slightly farther to the southwest.

Averaged over a ~9-year long period, the earlier SSE (Figures 2.15, 2.20) has a peak slip rate of ~110 mm/yr including the long-term relative average plate motion rate (55 mm/yr), and the slip rate averaged over its total slip area of 13418 km^2 was 82 mm/yr. Over its ≥ 9-year duration, the cumulative geodetic moment of this SSE was $4.97 \times 10^{20} N \cdot m$ (M_w ~7.8), which is a minimum value as we can't constrain the start time of the event. This SSE involve slip equivalent to 14 years of plate motion using the average slip rate. During the non-SSE time period (period 4: 2011.81-2014.87), the region of largest slip during the SSE has an average slip deficit rate of only ~20 mm/yr (range 10-30 mm/yr). If that is representative of the rate of slip deficit between SSEs, then the slip for a 9 year-long SSE will be equivalent to ~38 years of steady deformation, which

makes it possible that this event accounted for all of the accumulated slip deficit since the 1964 earthquake. On the other hand, the area between the two SSEs in Figure 2.20 (yellow coloring) is the result of a change from completely locked in period 1 to partially locked in period 4. This may be related to the trade-offs between SSEs and locking in the slip distribution, although even models that allow only positive slip deficit show some feature there (e.g., Figure 2.16b).

The SSE in period 3 has a peak slip rate of ~120 mm/yr and an average slip rate of 91 mm/yr over its 2-year duration. The geodetic moment of this SSE is $6.98 \times 10^{19} N \cdot m$ (M_w ~7.2). It thus accounts for about 4 years of plate motion or close to a decade of slip deficit accumulation. Although uncertainties remain large, the magnitude of slip in the period 3 SSE is similar to the total slip deficit in the region during period 2, and we propose that the duration of this second SSE was limited by the accumulated slip deficit after the first SSE.

Over most of the megathrust within the 1964 earthquake rupture area, the pattern of slip deficit remains the same for all four time periods, although model resolution is poor trenchward of the Pacific coast. In particular, the first order pattern of along-strike variations in the downdip end of the main locked zone has not changed over the ~20 years of GPS data. However, the areas of slow slip immediately downdip of that show large changes in slip rates with time. The slip rates in the area of the lower Cook Inlet SSEs change abruptly from ~95-110 mm/yr in period 1 to ~25-55 mm/yr in period 2, which is smaller than the plate convergence rate (red box area in Figures 2.15 and 2.16). Then the slip rates change back to ~85-120 mm/yr in the next SSE (period 3) and finally change back to ~25-45 mm/yr in time period 4 (red box area in Figures 2.17 and 2.18). These slip rate changes are relatively abrupt. Also the slip rates seem to be relatively constant during the slow slip events, as evidenced by nearly linear time series, rather than varying continually with time as in the Upper Cook Inlet SSEs. This suggests the possibility of some mechanical rate limit for slow slip in this area, although the mechanism that would lead to this is unclear. Note that the bounds on ϕ in the inversion would have allowed slip at up to 3 times the rate of plate motion, so we do not think this result is an artifact of the inversion. Updip of the SSEs we have identified here, there have been no observable significant changes of the locking fraction or slip deficit rates in the shallow zone. On parts of the model that have good resolution, the interface has remained completely locked over the last 20 years.

The red-orange areas in figures 2.15-2.18 represent the completely locked area and the yellow marks the transition from the completely to partially locked which we refer to as the locking

depth. There are clear along-strike variations in the depth of the transition in all four time periods. For time period (period 4), the locking depth is ~45 km in the Prince William Sound area, shallows to ~35 km under the Kenai Peninsula, and shallows again to ~25 km under the Kodiak Island (Figure 2.18). This is inversely correlated to the slab dip angle, in that the shallowest slab dip corresponds to the deepest locking depth, leading to a dramatic widening of the locked zone from southwest to northeast. The shallow-dipping slab corresponds to the subduction of the Yakutat block (Eberhart-Phillips et al., 2006).

2.6.2 Duration and magnitude scaling of the Lower Cook Inlet slow slip events

Moment magnitudes for the two Lower Cook Inlet SSEs were computed in the previous section. We also calculate the moments of these SSEs based on differences of slip deficit rates between periods 1 and 4, between periods 3 and 4; and slip deficit rates inverted from differences of velocities between periods 1 and 4 and periods 3 and 4.

Ide et al. (2007) found a linear scaling between the log SSE duration (T) and the log equivalent moment (M_o) ($M_o \propto \mathrm{T}$) (Figure 2.22), which is different from that of normal earthquakes where $M_o \propto T^3$. From the two observed SSEs in the Lower Cook Inlet in this study and two previous observed SSEs in the Upper Cook Inlet, all four SSEs are located within the orange shaded area that marks the scaling relation $M_o \propto T$ proposed by Ide et al. (2007). All four Alaska events lie near the upper boundary of that area (Figure 2.22), and the best fit line based only on the Alaska SSEs has $M_o \propto T^{1.3}$. Compared with all global examples of SSEs, the newly observed 9 year long period SSE appears to be the longest SSE recorded geodetically so far. Meade & Loveless (2009) suggested that very long slow slip events would be difficult to distinguish from partial locking, because the slip rates would be comparable to or lower than plate motion rates. However the 9-year SSE here has slip rates in excess of plate rates which make it observable geodetically but well within the slip rates suggested by Meade & Loveless (2009) for an event of this duration.

Evidence is increasing for the existence of decadal-scale or longer slow slip events or time variations in locking in multiple subduction zones. Shennan & Hamilton (2006)presented evidence for a possible slow event lasting 10-15 years that immediately preceded the 1964 Alaska earthquake. If the subsidence they inferred from changes in diatom assemblages resulted from a SSE, the slip would have occurred further updip at shallower depth than any of the SSE observed geodetically (Fu & Freymueller, 2013; Ohta et al., 2006; Wei et al., 2012). In the Sumatra

subduction zone, coral paleo-geodesy provides evidence for significant changes in uplift/subsidence rates over time (Meltzner et al., 2010, 2012). Recent work has shown that a ~15 year-long change in the uplift pattern in the Banyak Islands can be explained by the occurrence of a very long slow slip event (Meltzner et al., 2015; Tsang et al., 2015). Scaling laws (Ide et al., 2007; Meade & Loveless, 2009) do not suggest any clear upper limit for the duration or magnitude of slow slip events, and it is possible that as the time span of precise geodetic observations increases, longer and longer transient events may be found.

2.7 Conclusions

GPS time series for sites in Lower Cook Inlet, Alaska, show changes in velocity three times within the span 1995 to 2014; in late 2004, ~2010, and late 2011. The exact timing of the change in 2004 is weakly constrained because only two continuous GPS sites were operating at the time. However, the ~2010 and late 2011 velocity changes were abrupt, with the timing of the change determined within a few weeks at each site. Unlike the other slow slip events observed in Alaska, slip rates appear to be relatively constant during these slow slip events. The timing of each velocity change had a spatial progression, with the velocity changes propagating in either the updip or downdip direction.

We develop an improved block model for the region, which combines the Kenai Peninsula and Alaska Peninsula as a Peninsula block (PENN), along with Southern Alaska (SOAK) and Bering (BRNG) blocks. We estimate the angular velocity of the PENN block and a nominal average plate coupling variation simultaneously using a combination of periods 1 and 4, which have the best data constraints. We find that a single angular velocity fit data from all time periods well.

We then estimate the slip deficit rate distribution for the four time periods with two different limiting ranges of the locking fraction (ϕ): [-2, 1] and [0, 1]. The data require negative slip deficit rates in the Lower Cook Inlet area in periods 1 and 3, which indicates that slip rates were faster than plate convergence rates during these two time periods. The SSE in period 1 lasted at least 9 years, as it was already underway when our observations in that area begin in 1995. Another slow slip event in the same area lasted almost 2 years from the end of 2009 to the end of 2011.

The SSEs started and ended abruptly, within a period of a few months. The timing of velocity changes at individual sites suggests that at the start of these SSEs, the plate interface began to creep first at the downdip end, with the slip event propagating updip over a period of several

weeks to a few months. Then, at the end of each event, the plate interface began to lock up first at the updip end, with the cessation of slip propagating downdip.

The 9-year long SSE in period 1 and the ~2 year-long SSE in period 3 were both located at the same depth range of 40 to 60 km, at the downdip end of the locked zone. We find that the locking depth in the non-SSE time period is inversely correlated with the slab dip, with a deeper locking depth of ~45 km found in the Prince William Sound where the slab dip angle is shallowest. In the area of the Lower Cook Inlet slow events, between events the interface is fully locked to a depth of ~35 km, and then partially locked to a depth of ~60 km.

2.8 Acknowledgments

We appreciate Laura Wallace, David Schmidt and another anonymous reviewer for providing helpful comments that significantly improve the manuscripts. We acknowledge EarthScope for the Plate Boundary Observatory (PBO) data, and UNAVCO for operations of the PBO. All GPS data used in this work are archived at the UNAVCO or NGS/CORS archives. This research was supported by NSF award EAR-1215933 to the University of Alaska Fairbanks. We use the Generic Mapping Tools (GMT) to draw the figures.

2.9 References

Altamimi, Z., X. Collilieux, and L. Métivier (2011), ITRF2008: an improved solution of the international terrestrial reference frame, *Journal of Geodesy*, *85*(8), 457-473.

Argus, D. F., R. G. Gordon, M. B. Heflin, C. Ma, R. J. Eanes, P. Willis, W. R. Peltier, and S. E. Owen (2010), The angular velocities of the plates and the velocity of Earth's centre from space geodesy, *Geophysical Journal International*, *180*(3), 913-960.

Brocher, T. M., G. S. Fuis, M. A. Fisher, G. Plafker, M. J. Moses, J. J. Taber, and N. I. Christensen (1994), Mapping the megathrust beneath the northern Gulf of Alaska using wide-angle seismic data, *Journal of Geophysical Research: Solid Earth (1978–2012)*, *99*(B6), 11663-11685.

Cohen, S. C., and J. T. Freymueller (2004), Crustal deformation in the southcentral Alaska subduction zone, *Advances in geophysics*, *47*, 1-63.

Cross, R. S., and J. T. Freymueller (2008), Evidence for and implications of a Bering plate based on geodetic measurements from the Aleutians and western Alaska, *Journal of Geophysical Research: Solid Earth (1978–2012)*, *113*(B7).

DeMets, C., B. Márquez-Azúa, and E. Cabral-Cano (2014), A new GPS velocity field for the Pacific Plate-Part 1: constraints on plate motion, intraplate deformation, and the viscosity of Pacific basin asthenosphere, *Geophysical Journal International*, *199*, 1878-1899.

Dragert, H., K. Wang, and T. S. James (2001), A silent slip event on the deeper Cascadia subduction interface, *Science*, *292*(5521), 1525-1528.

Eberhart-Phillips, D., D. H. Christensen, T. M. Brocher, R. Hansen, N. A. Ruppert, P. J. Haeussler, and G. A. Abers (2006), Imaging the transition from Aleutian subduction to Yakutat collision in central Alaska, with local earthquakes and active source data, *Journal of Geophysical Research: Solid Earth (1978–2012)*, *111*(B11).

Elliott, J., J. T. Freymueller, and C. F. Larsen (2013), Active tectonics of the St. Elias orogen, Alaska, observed with GPS measurements, *Journal of Geophysical Research: Solid Earth*, *118*(10), 5625-5642.

Fletcher, H. J. (2002), Crustal deformation in Alaska measured using the Global Positioning System, University of Alaska Fairbanks.

Freed, A. M., R. Bürgmann, E. Calais, J. Freymueller, and S. Hreinsdóttir (2006), Implications of deformation following the 2002 Denali, Alaska, earthquake for postseismic relaxation processes and lithospheric rheology, *Journal of Geophysical Research: Solid Earth (1978–2012)*, *111*(B1).

Freymueller, J. T., H. Woodard, S. C. Cohen, R. Cross, J. Elliott, C. F. Larsen, S. Hreinsdottir, and C. Zweck (2008), Active deformation processes in Alaska, based on 15 years of GPS measurements, *Active tectonics and seismic potential of Alaska*, *179*, 1-42.

Fu, Y., and J. T. Freymueller (2013), Repeated large Slow Slip Events at the southcentral Alaska subduction zone, *Earth and Planetary Science Letters*, *375*, 303-311.

Fu, Y., J. T. Freymueller, and T. Jensen (2012), Seasonal hydrological loading in southern Alaska observed by GPS and GRACE, *Geophysical Research Letters*, *39*(15).

Fu, Y., Z. Liu, and J. T. Freymueller (2015), Spatiotemporal variations of the slow slip event between 2008 and 2013 in the southcentral Alaska subduction zone, *Geochemistry, Geophysics, Geosystems*.

Furumoto, A. S. (1965), Analysis of Rayleigh wave, Part II in source mechanism study of the Alaska earthquake and tsunami of March 27, 1964*Rep.*, Report HIG-65-17, Honolulu: University of Hawaii, Institute of Geophysics, December, 31-42.

Hayes, G. P., D. J. Wald, and R. L. Johnson (2012), Slab1. 0: A three-dimensional model of global subduction zone geometries, *Journal of Geophysical Research: Solid Earth (1978–2012)*, *117*(B1).

Ide, S., G. C. Beroza, D. R. Shelly, and T. Uchide (2007), A scaling law for slow earthquakes, *Nature*, *447*(7140), 76-79.

Johnson, K. M., R. Bürgmann, and J. T. Freymueller (2009), Coupled afterslip and viscoelastic flow following the 2002 Denali Fault, Alaska earthquake, *Geophysical Journal International*, *176*(3), 670-682.

Kobayashi, A. (2014), A long-term slow slip event from 1996 to 1997 in the Kii Channel, Japan, *Earth, Planets and Space*, *66*(1), 1-7.

Kostoglodov, V., S. K. Singh, J. A. Santiago, S. I. Franco, K. M. Larson, A. R. Lowry, and R. Bilham (2003), A large silent earthquake in the Guerrero seismic gap, Mexico, *Geophysical Research Letters*, *30*(15).

Lahr, J. C., and G. Plafker (1980), Holocene Pacific–North American plate interaction in southern Alaska: Implications for the Yakataga seismic gap, *Geology*, *8*(10), 483-486.

McCaffrey, R. (2002), Crustal block rotations and plate coupling, *Plate boundary zones*, 101-122.

McCaffrey, R. (2009), Time-dependent inversion of three-component continuous GPS for steady and transient sources in northern Cascadia, *Geophysical Research Letters*, *36*(7).

Meade, B. J., and J. P. Loveless (2009), Predicting the geodetic signature of MW≥ 8 slow slip events, *Geophysical Research Letters*, *36*(1).

Meltzner, A. J., K. Sieh, H.-W. Chiang, C.-C. Wu, L. L. Tsang, C.-C. Shen, E. M. Hill, B. W. Suwargadi, D. H. Natawidjaja, and B. Philibosian (2015), Time-varying interseismic strain rates and similar seismic ruptures on the Nias–Simeulue patch of the Sunda megathrust, *Quaternary Science Reviews*, *122*, 258-281.

Meltzner, A. J., K. Sieh, H. W. Chiang, C. C. Shen, B. W. Suwargadi, D. H. Natawidjaja, B. Philibosian, and R. W. Briggs (2012), Persistent termini of 2004-and 2005-like ruptures of the Sunda megathrust, *Journal of Geophysical Research: Solid Earth (1978–2012)*, *117*(B4).

Meltzner, A. J., K. Sieh, H. W. Chiang, C. C. Shen, B. W. Suwargadi, D. H. Natawidjaja, B. E. Philibosian, R. W. Briggs, and J. Galetzka (2010), Coral evidence for earthquake recurrence and an AD 1390–1455 cluster at the south end of the 2004 Aceh–Andaman rupture, *Journal of Geophysical Research: Solid Earth (1978–2012)*, *115*(B10).

Nishimura, T., T. Matsuzawa, and K. Obara (2013), Detection of short-term slow slip events along the Nankai Trough, southwest Japan, using GNSS data, *Journal of Geophysical Research: Solid Earth*, *118*(6), 3112-3125.

Ochi, T., and T. Kato (2013), Depth extent of the long-term slow slip event in the Tokai district, central Japan: A new insight, *Journal of Geophysical Research: Solid Earth*, *118*(9), 4847-4860.

Ohta, Y., J. T. Freymueller, S. Hreinsdóttir, and H. Suito (2006), A large slow slip event and the depth of the seismogenic zone in the south central Alaska subduction zone, *Earth and Planetary Science Letters*, *247*(1), 108-116.

Okada, Y. (1985), Surface deformation due to shear and tensile faults in a half-space, *Bulletin of the seismological society of America*, *75*(4), 1135-1154.

Peng, Z., and J. Gomberg (2010), An integrated perspective of the continuum between earthquakes and slow-slip phenomena, *Nature Geoscience*, *3*(9), 599-607.

Press, W. H. (1989), *Numerical recipes in Pascal: the art of scientific computing*, Cambridge University Press.

Savage, J. (1983), A dislocation model of strain accumulation and release at a subduction zone, *J. geophys. Res*, *88*(6), 4984-4996.

Schwartz, S. Y., and J. M. Rokosky (2007), Slow slip events and seismic tremor at circum-Pacific subduction zones, *Reviews of Geophysics*, *45*(3).

Sella, G. F., S. Stein, T. H. Dixon, M. Craymer, T. S. James, S. Mazzotti, and R. K. Dokka (2007), Observation of glacial isostatic adjustment in "stable" North America with GPS, *Geophysical Research Letters*, *34*(2).

Shennan, I., and S. Hamilton (2006), Coseismic and pre-seismic subsidence associated with great earthquakes in Alaska, *Quaternary Science Reviews*, *25*(1), 1-8.

Suito, H., and J. T. Freymueller (2009), A viscoelastic and afterslip postseismic deformation model for the 1964 Alaska earthquake, *Journal of Geophysical Research: Solid Earth (1978–2012)*, *114*(B11).

Szeliga, W., T. I. Melbourne, M. M. Miller, and V. M. Santillan (2004), Southern Cascadia episodic slow earthquakes, *Geophysical Research Letters*, *31*(16).

Tsang, L. L., A. J. Meltzner, B. Philibosian, E. M. Hill, J. T. Freymueller, and K. Sieh (2015), A 15-year slow slip event on the Sunda megathrust offshore Sumatra, *Geophysical Research Letters*.

Wallace, L. M., and J. Beavan (2010), Diverse slow slip behavior at the Hikurangi subduction margin, New Zealand, *Journal of Geophysical Research: Solid Earth (1978–2012)*, *115*(B12).

Wei, M., J. J. McGuire, and E. Richardson (2012), A slow slip event in the south central Alaska Subduction Zone and related seismicity anomaly, *Geophysical Research Letters*, *39*(15).

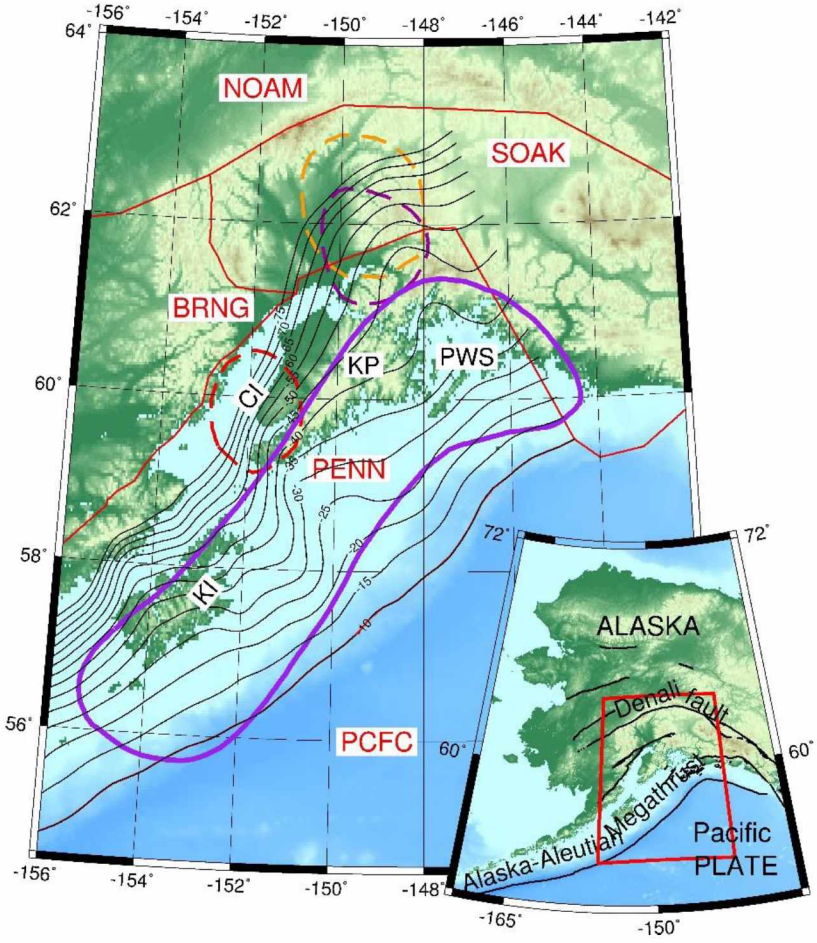

Figure 2.1 Topographic map and tectonic setting (inset) and study area in south-central Alaska (red outline in inset map). Black solid lines are plate interface depth contours (in km) from Slab 1.0 (Hayes et al., 2012). Red solid lines show the boundaries of blocks (named in red). Purple outline shows the approximate rupture extent of the 1964 earthquake from Furumoto (1965). Purple dashed outline shows the 1998-2001 slow slip event (Ohta et al., 2006); orange dashed outline shows the 2009-2013 slow slip event (Fu and Freymueller, 2013); red dashed outline shows the 2010-2011 slow slip event (Wei et al., 2012). NOAM: North American plate; SOAK: Southern Alaska Block; BRNG: Bering plate; PENN: Peninsula block; PCFC: Pacific plate; CI: Cook Inlet; KP: Kenai Peninsula; PWS: Prince William Sound; KI: Kodiak Island.

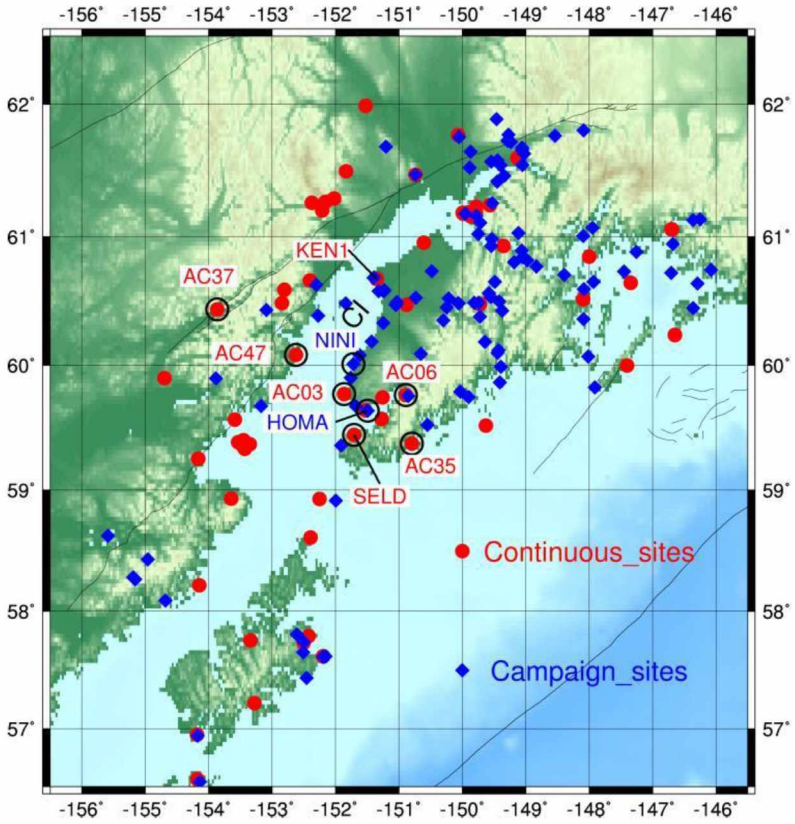

Figure 2.2 Continuous (red) and campaign GPS sites (blue) in the study area.The sites SELD and KEN1 are labeled, and the other sites shown in Figure 2.3a are circled with outlines and also labeled.

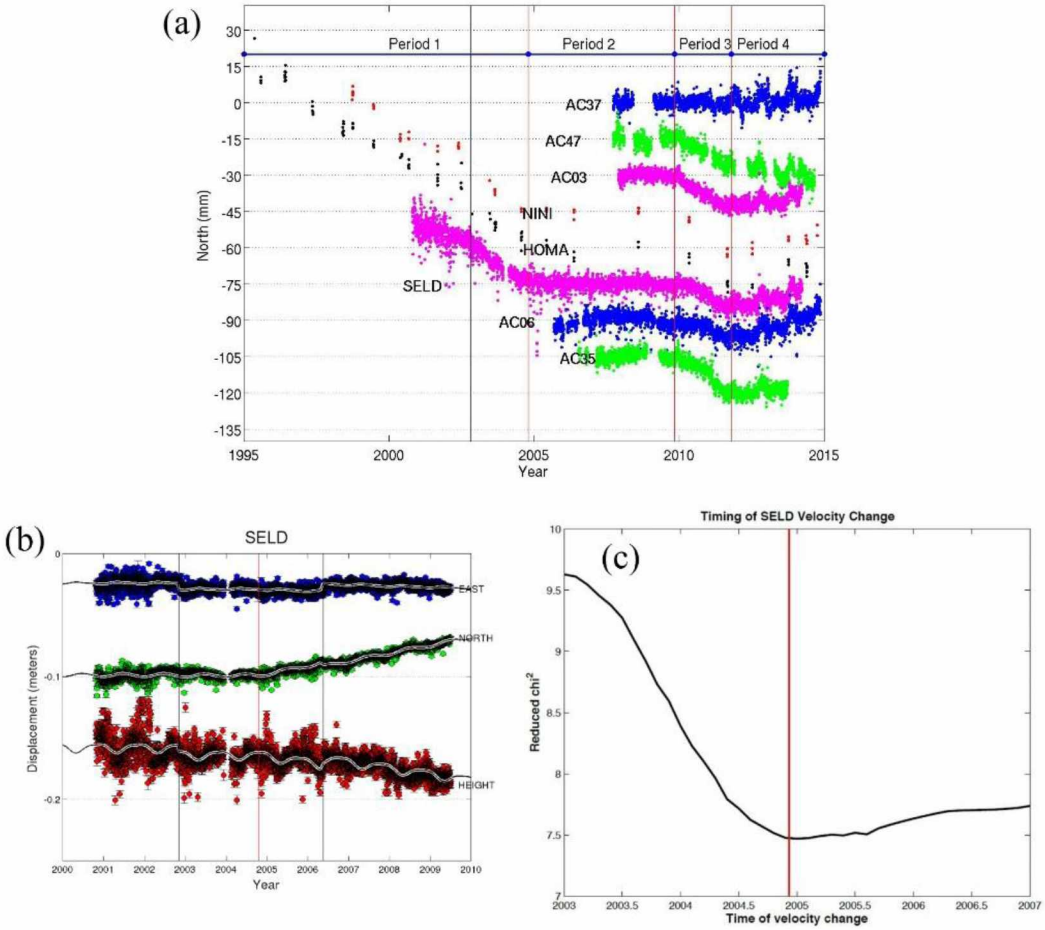

Figure 2.3 Example of GPS time series in Lower Cook Inlet. (a) North components of time series (detrended using the average velocity in 2004-2010) from a sample of GPS stations, ordered in a trench-normal profile (black outlines in Figure 2.2). Red lines show the dates of velocity changes. The 2002 Denali fault earthquake (black solid line) caused an offset at these sites, but mainly in the east component (not shown). The east component shows much smaller changes in trend than the north component. Period 1: 1992–~2004; Period 2: ~2004 - ~2010; Period 3: ~2010 - ~2011; Period 4: ~2011 – ~2015; (b) Seldovia (SELD) time series used for estimation of timing of the velocity change at about 2004, detrended based on pre-2004.8 data. The red lines shows the estimated time of the velocity change, while the black lines show the times of offsets. The black-white curve shows the estimated model fit to the time series; (c) Estimation of timing of SELD velocity change at 2004.8. The reduced chi-square of the least square fit is plotted as a function of the assumed time of the velocity change. The best fit timing of the velocity change is shown by the red line.

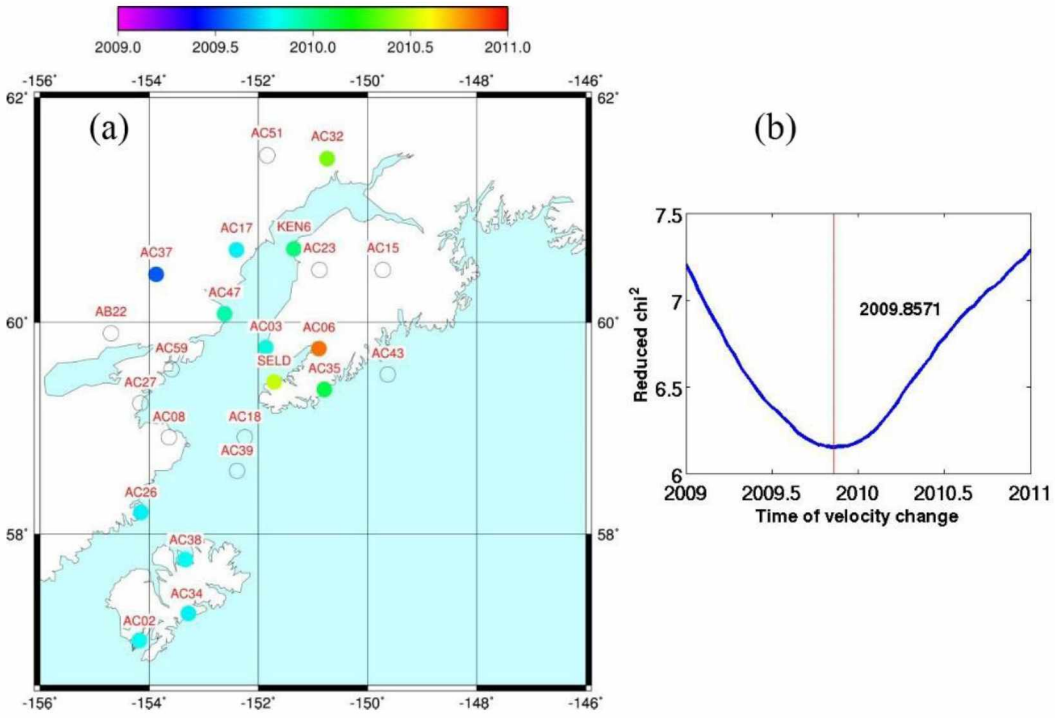

Figure 2.4 The spatial distribution of timing of velocity change for the continuous sites (a) and the general result for timing of velocity change at ~2010 (b) based on absolute difference of misfit for significant sites.

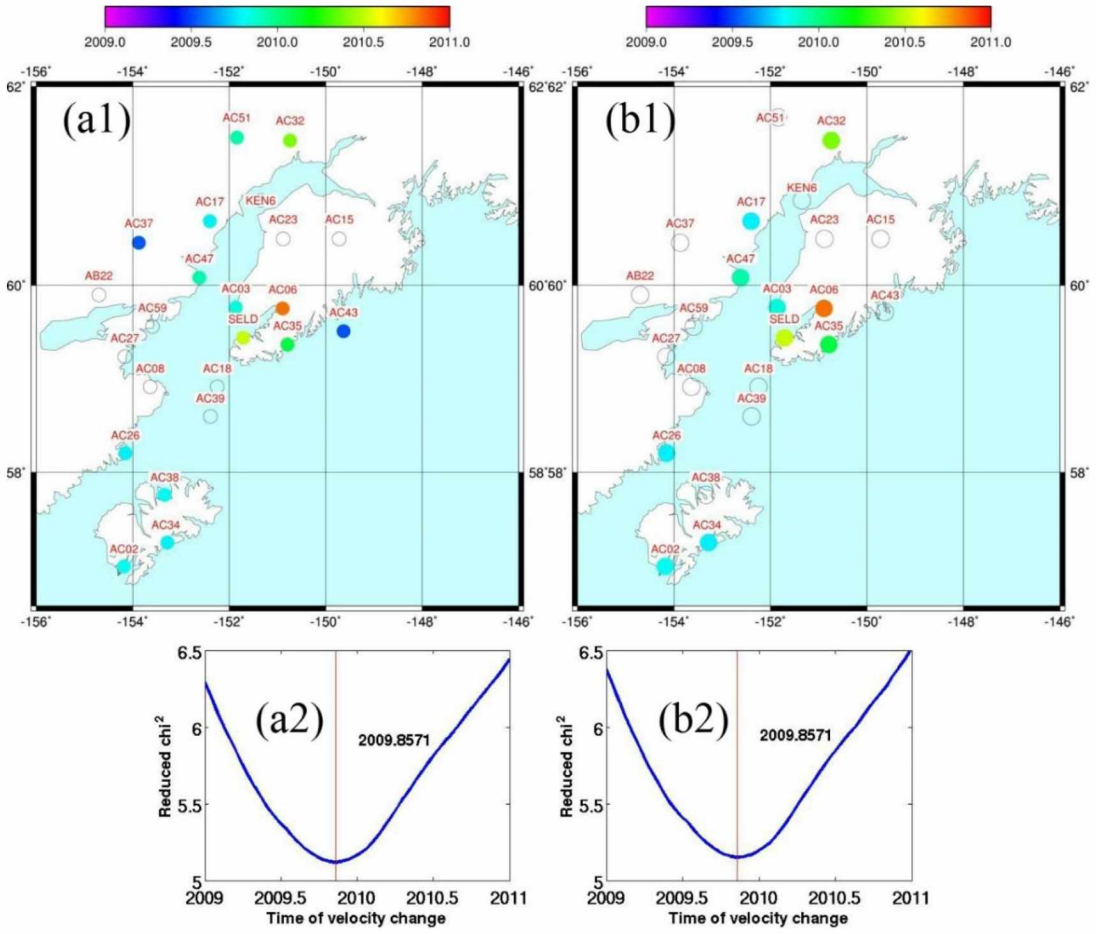

Figure 2.5 Comparison of the other two criteria used to determine which sites had significant velocity changes, for comparison to Figure 2.4.Panel a1 shows the spatial distribution of timing of velocity change and panel a2 shows the timing of velocity change at ~2010 using the relative difference of misfit to choose sites. Panel b1 shows the spatial distribution of timing of velocity change and panel b2 shows the timing of velocity change at ~2010 based on the size of velocity change. Results are similar to Figure 2.4.

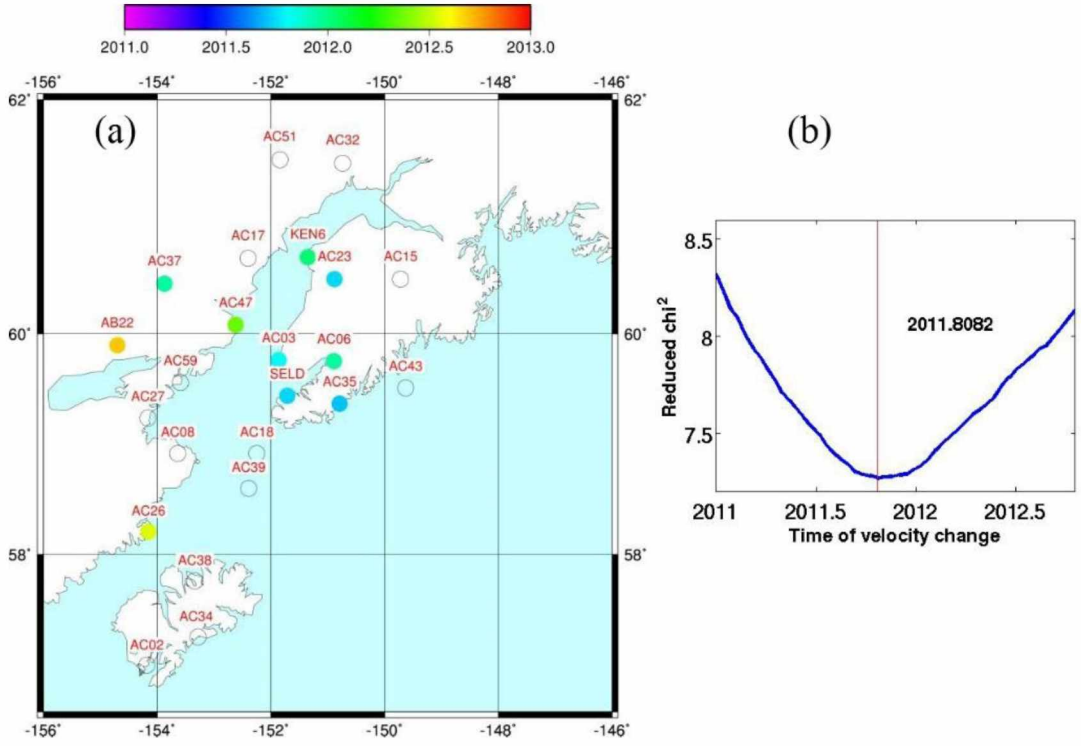

Figure 2.6 The spatial distribution of timing of velocity change for the continuous sites (a) and the general result for the timing of velocity change at ~2011 (b).

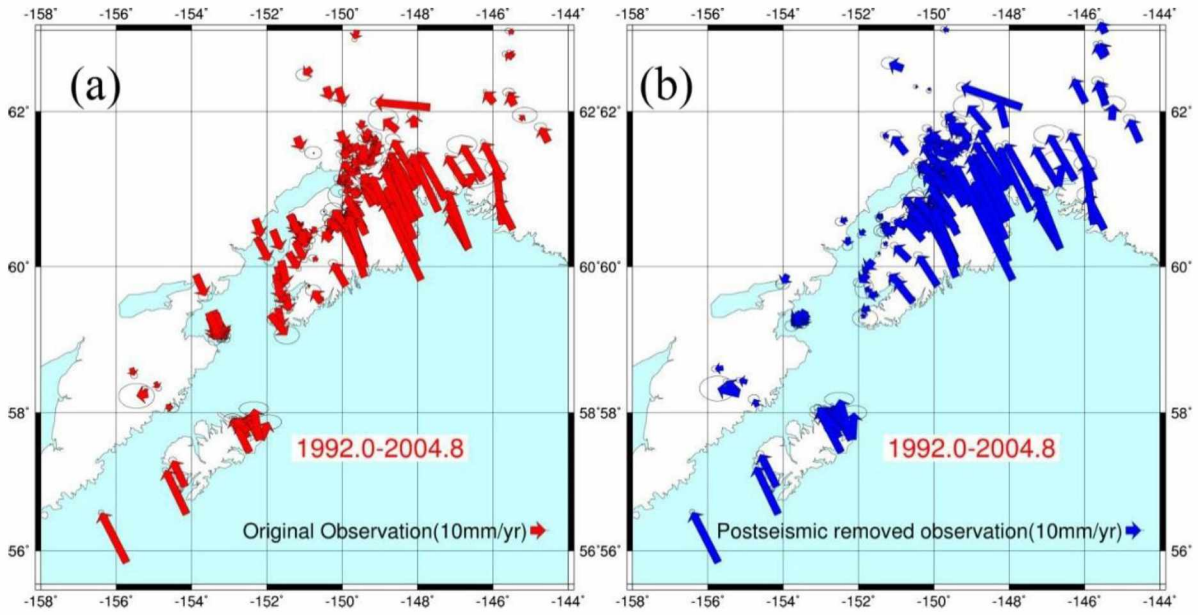

Figure 2.7 Comparison between original GPS velocity data (left) and GPS velocity data with postseismic effect corrected for period 1: 1992.0-2004.8 (a, b).

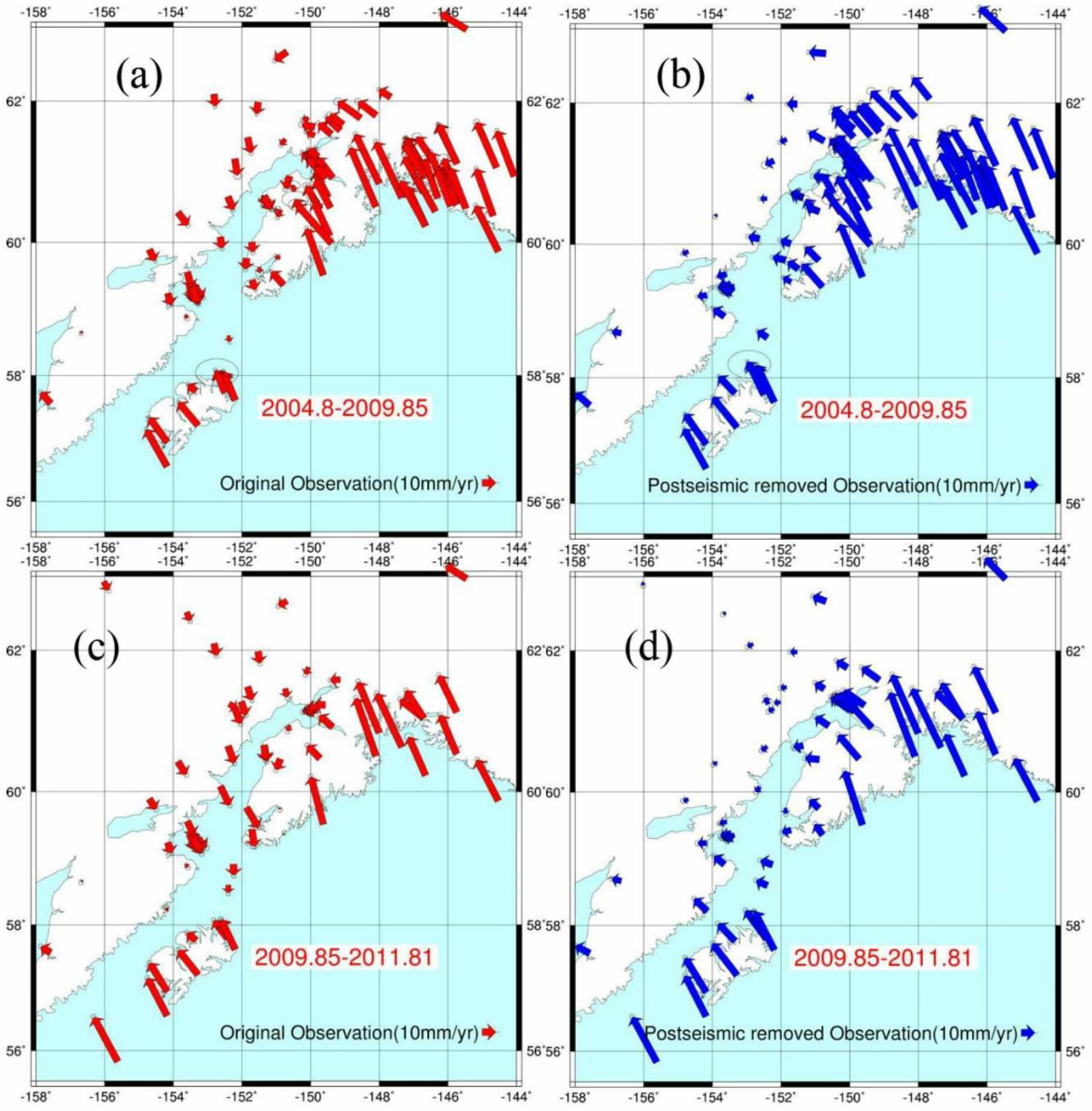

Figure 2.8 Comparison between the original GPS velocity data and GPS velocity data with postseismic effect corrected for periods 2 (a, b), 3 (c, d) and 4 (e, f).

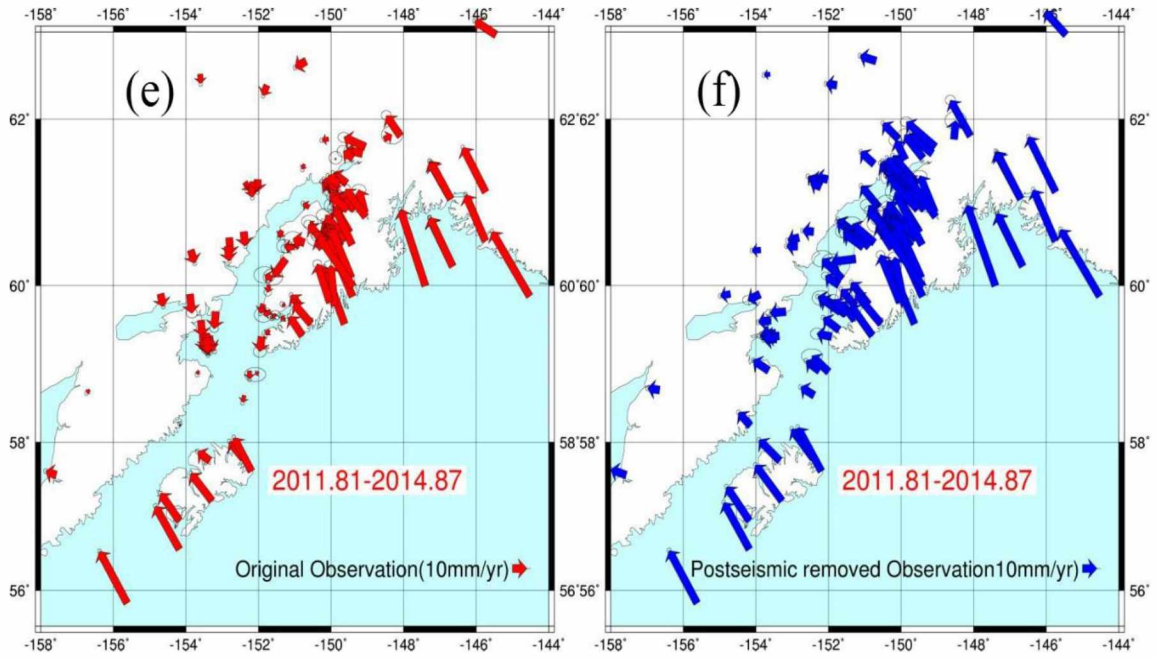

Figure 2.8 cont.

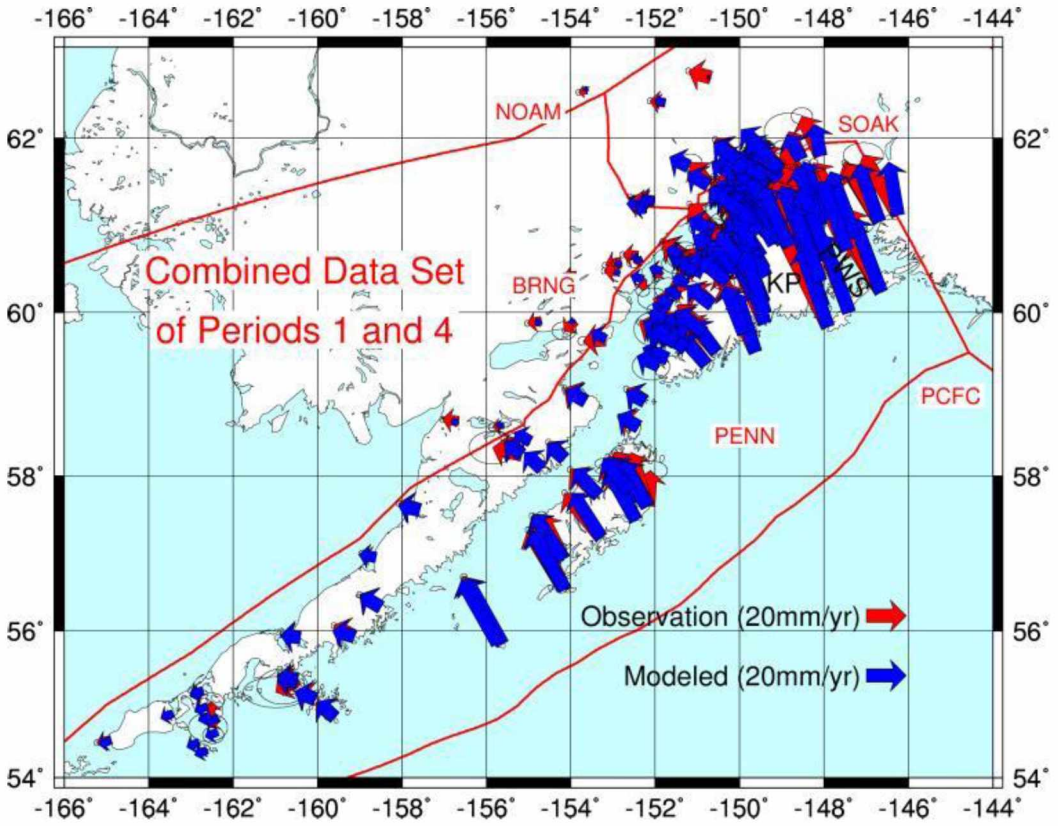

Figure 2.9 We used data from our main study area and also from the Alaska Peninsula in estimating the pole of rotation in the PENN (Peninsula) block.Figure 2.9 shows the observations and model predictions from this inversion.

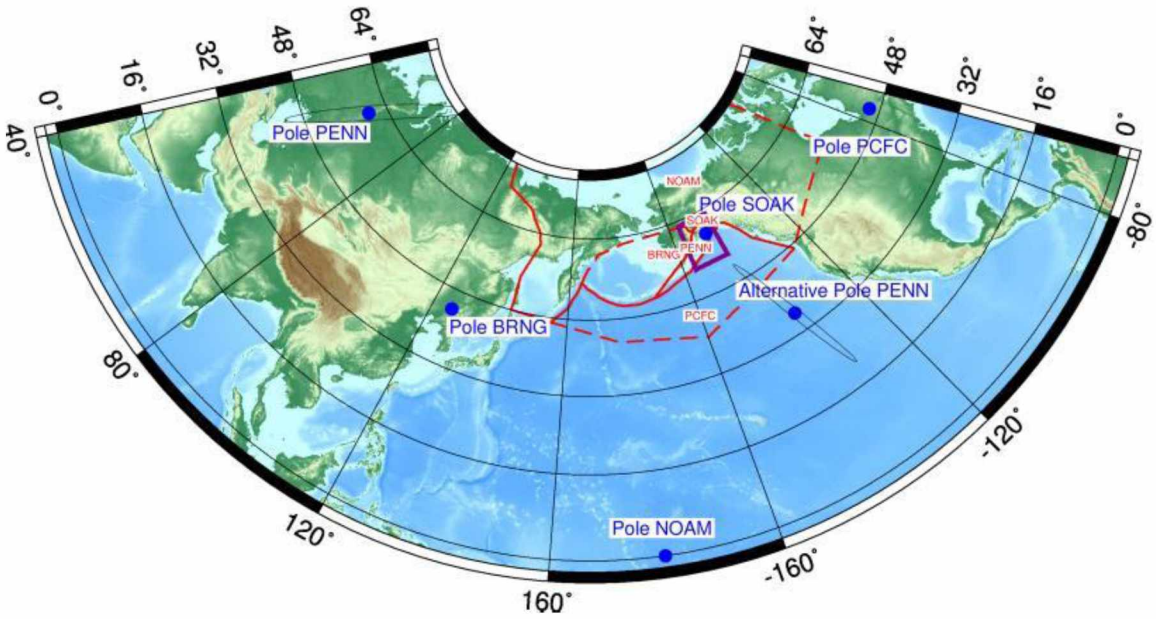

Figure 2.10 The location of poles (blue dots) for all the blocks.The red solid and dashed lines show the block boundaries. The purple rectangle shows the main study area. The alternate pole for PENN, based only on data from the main study area, is located in the eastern Pacific.

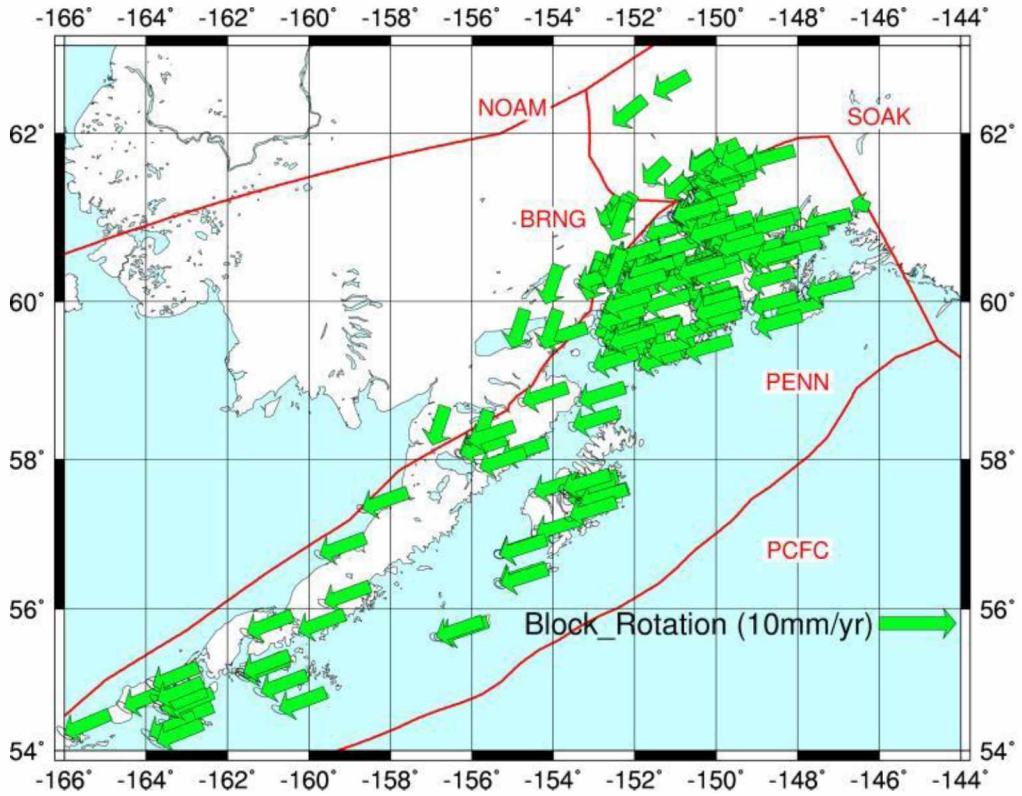

Figure 2.11 Predicted rotation velocities based on the pole estimated by inversion of the combination of data from periods 1 and 4. Red solid lines show the block boundaries. Sites on the Kenai Peninsula and Alaska Peninsula move almost uniformly towards the southwest.

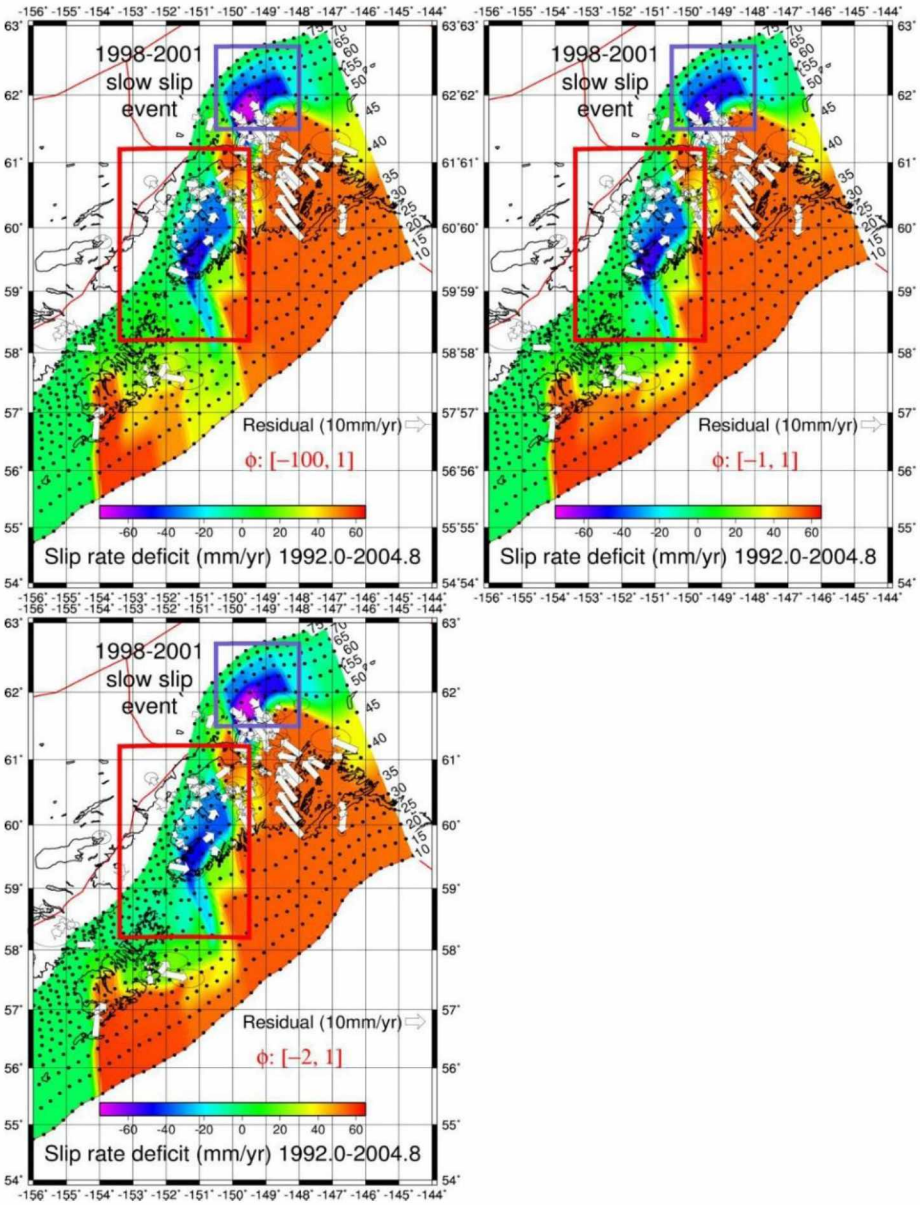

Figure 2.12 Slip distribution result with different ϕ ranges of period 1. Figure 2.12a shows the slip distribution result with ϕ range: [-100, 1] and smoothing factor 1e7. Figure 2.12b shows the slip distribution result with ϕ range: [-1, 1] and smoothing factor 1e7. Figure 2.12c shows the slip distribution result with ϕ range: [-2, 1] and smoothing factor 1e7. All three models show similar results, and we used the ϕ range [-2, 1] for all other inversions.

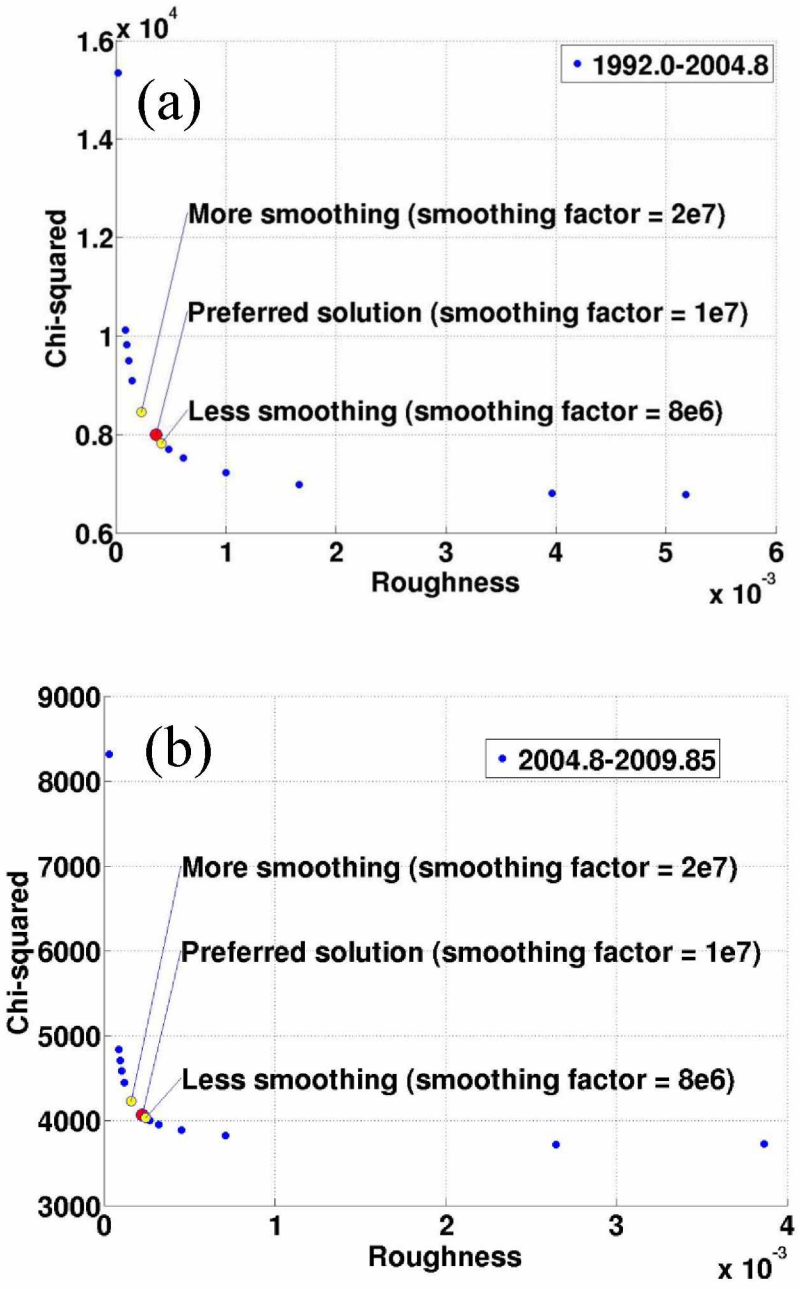

Figure 2.13 The trade-off curves between Chi-squared value of data and roughness for four time periods.(a) Period1: 1992.0-2004.8; (b) Period 2: 2004.8-2009.85; (c) Period 3: 2009.85-2011.81; (d) Period 4: 2011.81-2014.87. The preferred solution for smoothing factor is 1e7.

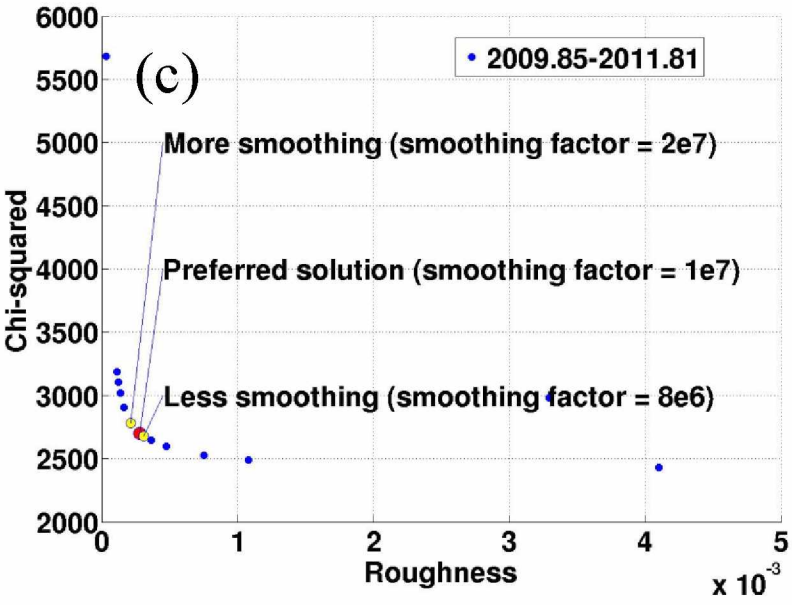

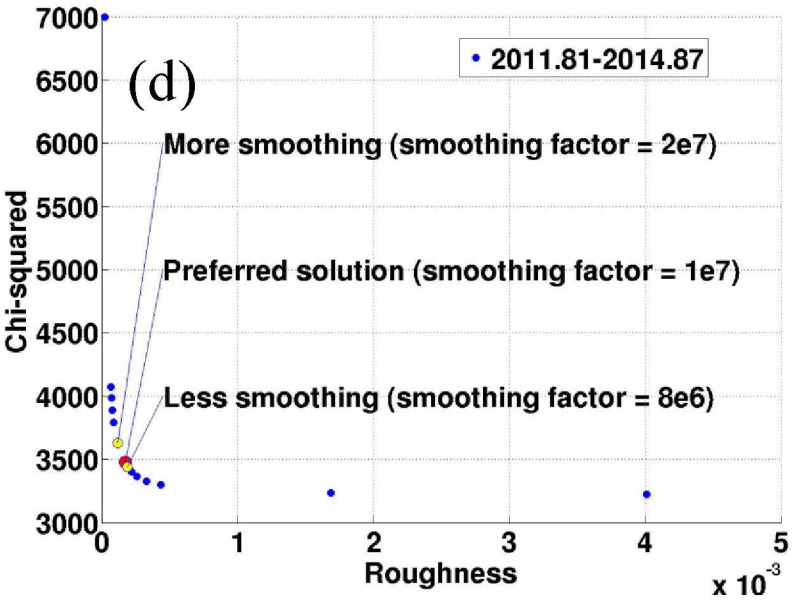

Figure 2.13 cont.

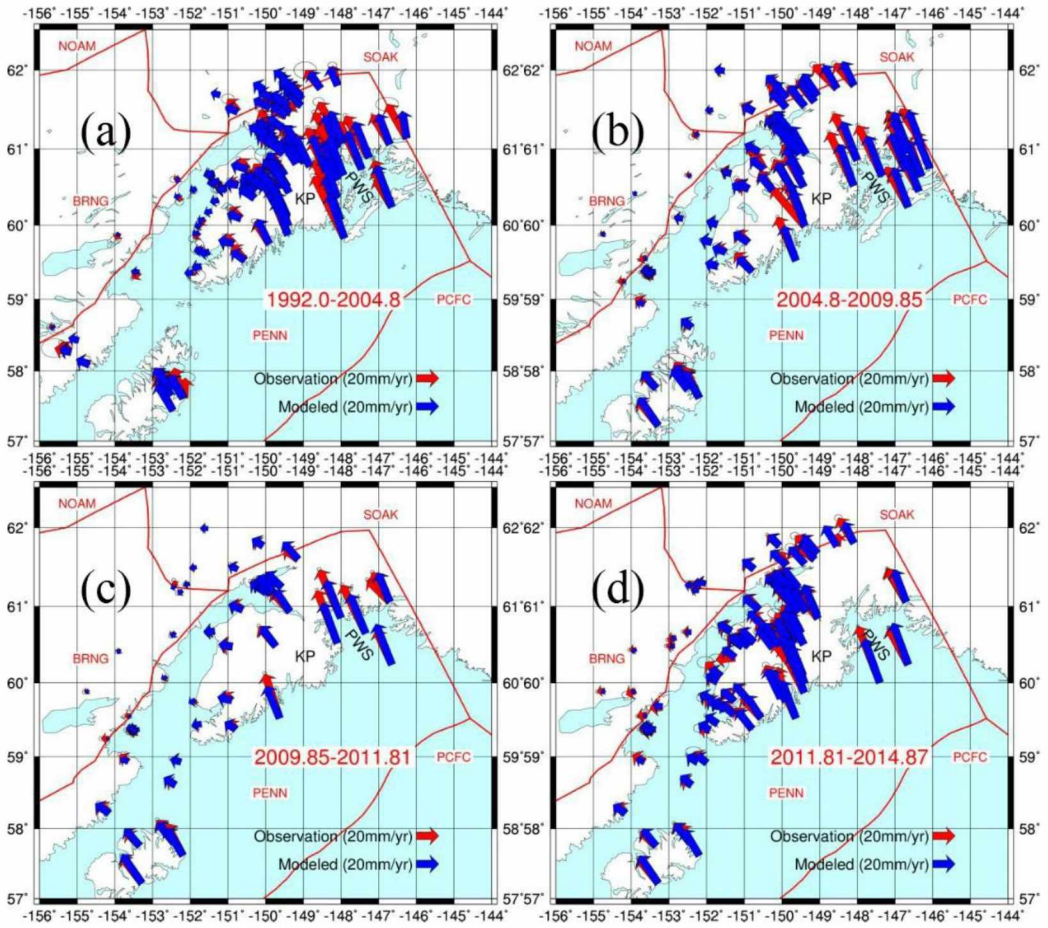

Figure 2.14 Comparison between the predicted (blue) and observed (red) velocities for each time period. (a) Period 1 (1992.0-2004.8) (b) Period 2 (2004.8-2009.85) (c) Period 3 (2009.85-2011.81) (d) Period 4 (2011.81-2014.87). PWS: Prince William Sound, KP: Kenai Peninsula.

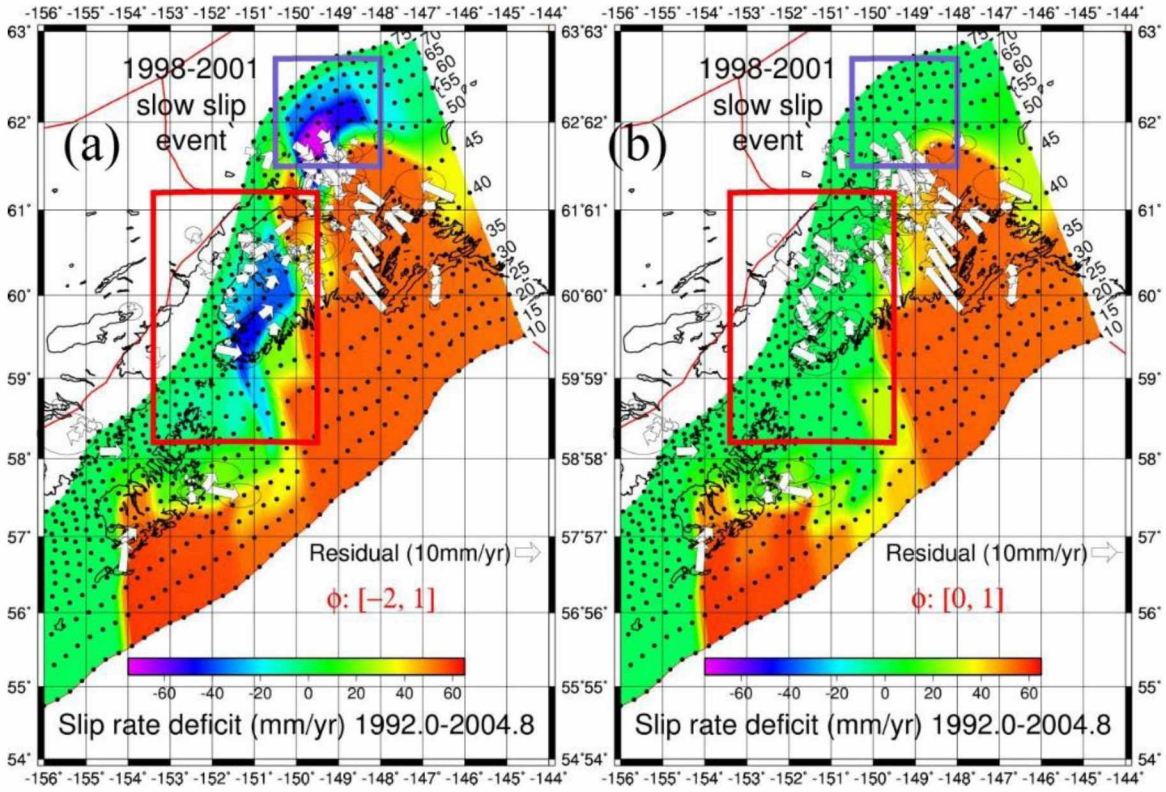

Figure 2.15 Slip deficit rate distribution and residual of GPS velocities (white arrows) with the node geometry for ϕ in the range [-2, 1] (a) and ϕ [0, 1] (b) during the period 1 (1992.0-2004.8). The red box marks the region affected by the temporal changes in slip deficit. Contours including black points (nodes) show the depth of the subduction zone. The blue box marks the area where displacements from the 1998-2001 slow slip event are large, based on Ohta et al. (2006).

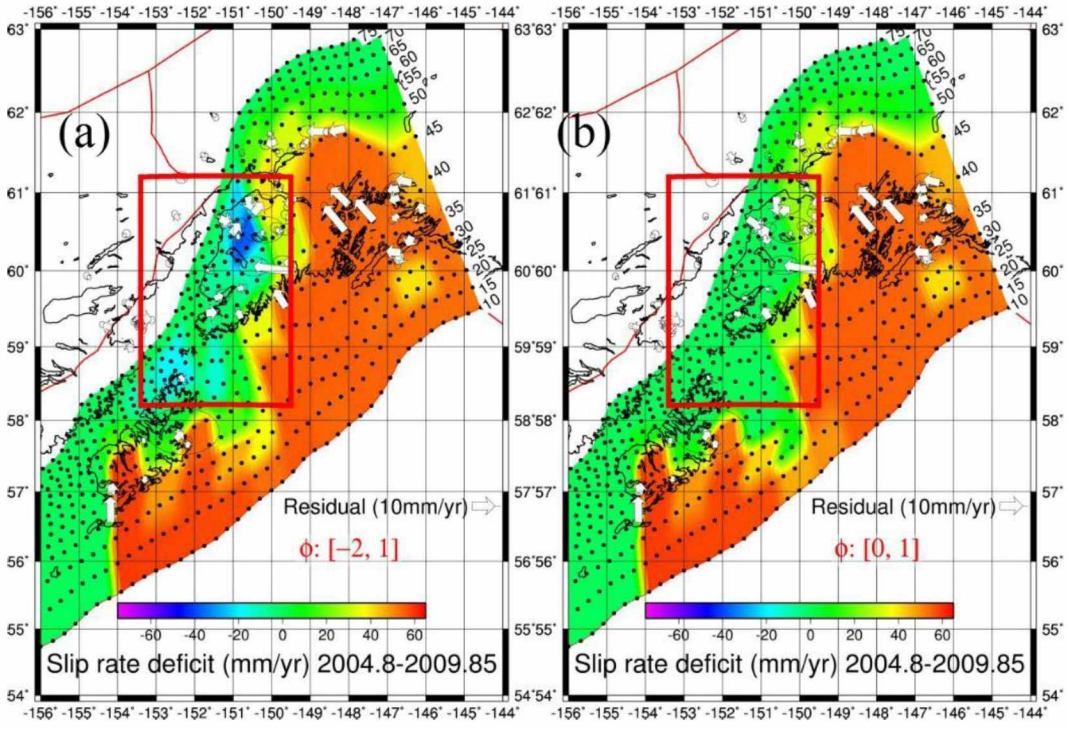

Figure 2.16 Slip deficit rate distribution and residual of GPS velocities with the node geometry for ϕ [-2, 1] (a) and ϕ [0, 1] (b) during the period 2 (2004.8-2009.85). The red box, arrows and contours are the same as in Figure 2.15.

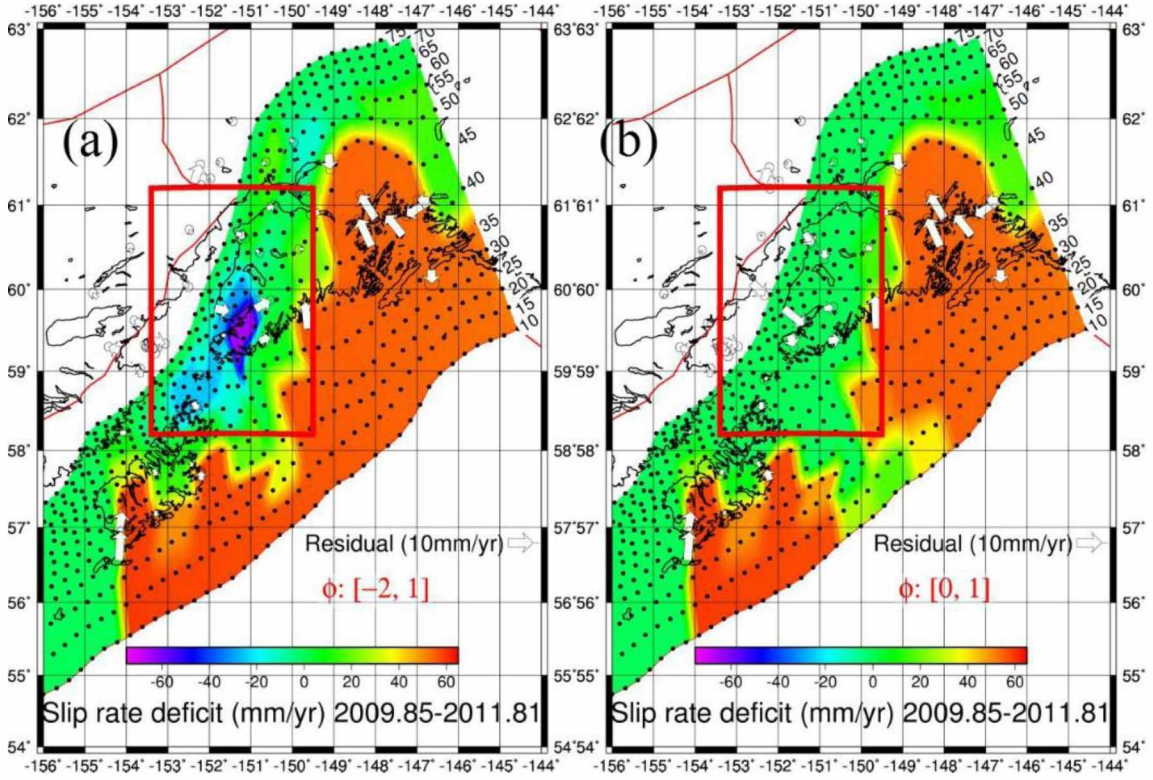

Figure 2.17 Slip deficit rate distribution and residual of GPS velocities with the node geometry for ϕ [-2, 1] (a) and ϕ [0, 1] (b) during the period 3 (2009.85-2011.81). The red box, arrows and contours are the same as in Figure 2.15.

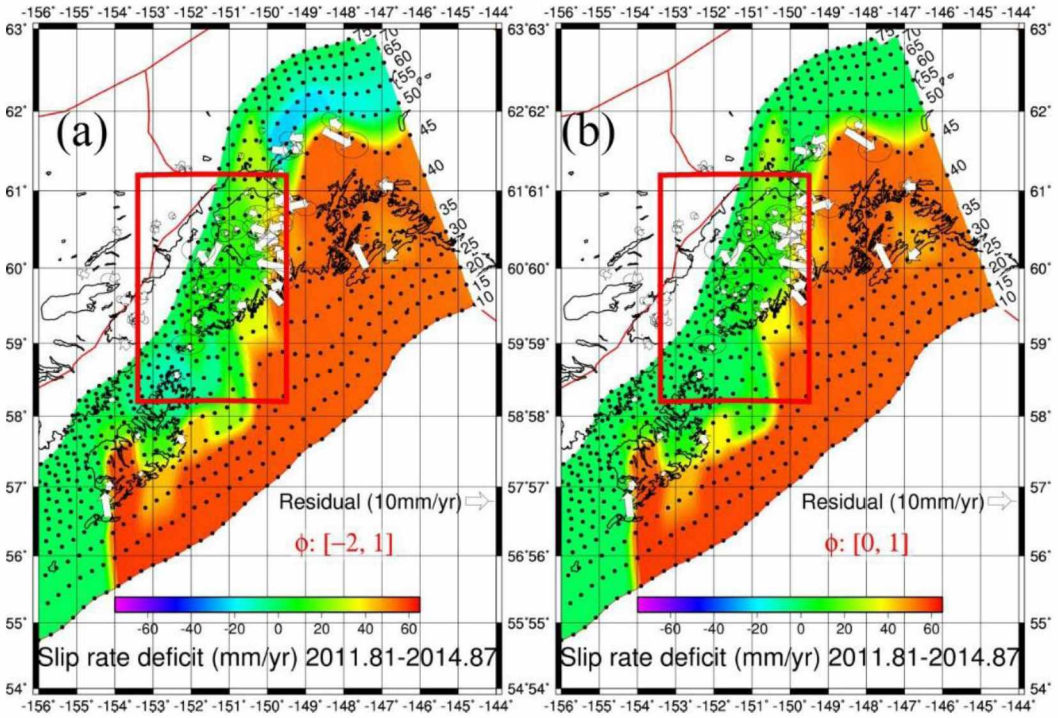

Figure 2.18 Slip deficit rate distribution and residual of GPS velocities with the node geometry for ϕ [-2, 1] (a) and ϕ [0, 1] (b) during the period 4 (2011.81-2014.87). The red box, arrows and contours are the same as in Figure 2.15.

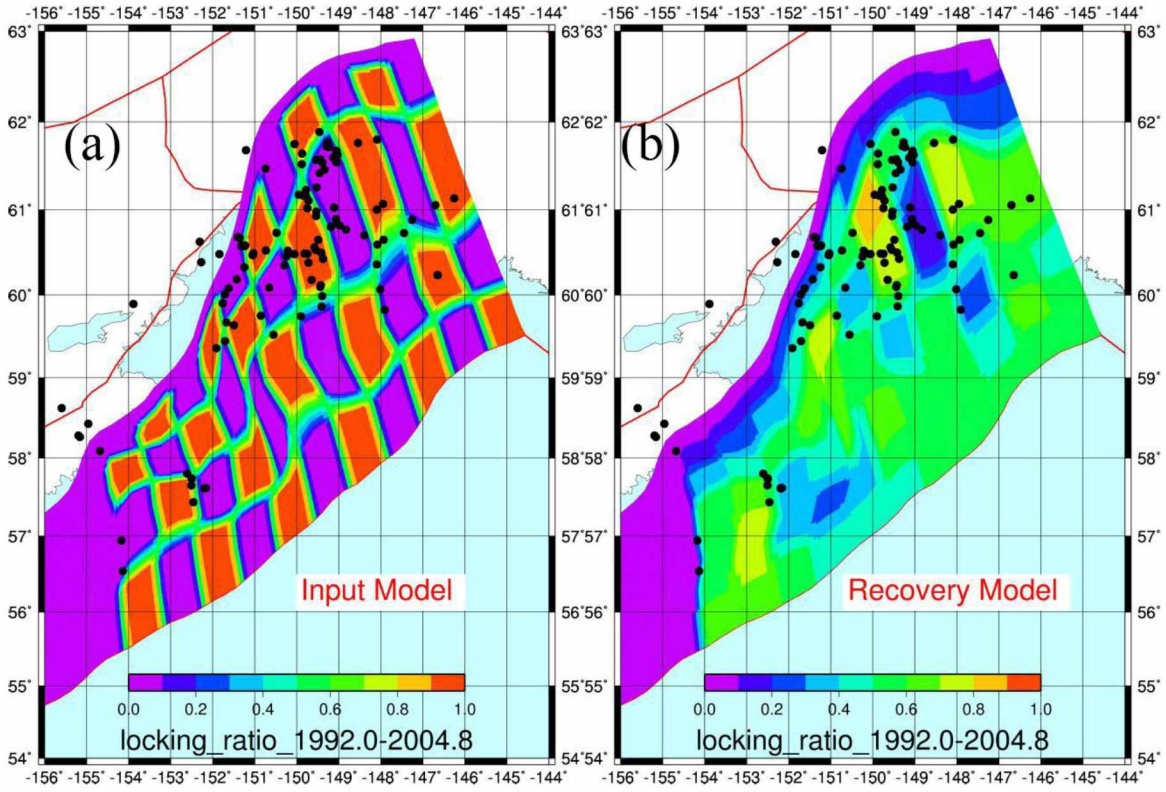

Figure 2.19 Model resolution from the checkerboard test. Figure 2.19a shows the input model in the checkerboard test. Figure 2.19b shows recovery model in the checkerboard test, with a starting model in the inversion that was fully locked.

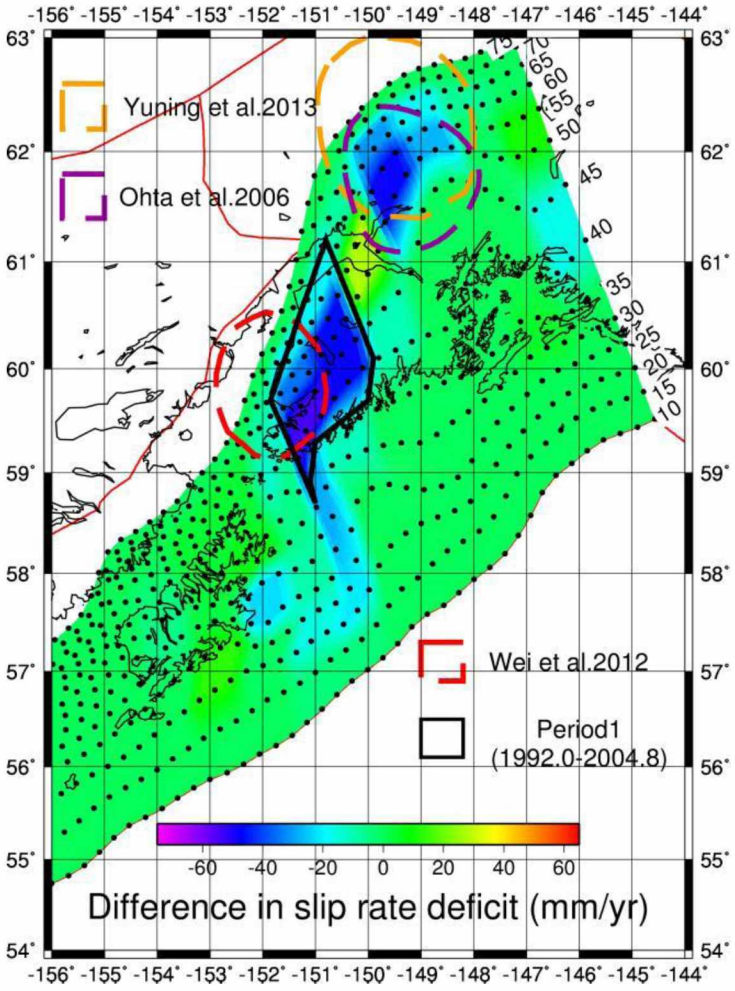

Figure 2.20 Inferred slip deficit rate distribution for the proposed 9-year-long slow slip event (thick black polygon) in period 1 (1992.0-2004.8). The orange dashed circle shows the slow slip event proposed by Fu and Freymueller (2013). The purple dashed circle shows the 1998-2001 slow slip event (Ohta et al., 2006). The red dashed circle shows the slow slip event proposed by Wei et al. (2012). The difference between the two model periods (period 1 and period 4 (2011.81-2014.87)) is shown using the same color scale as Figures 2.15-2.18.

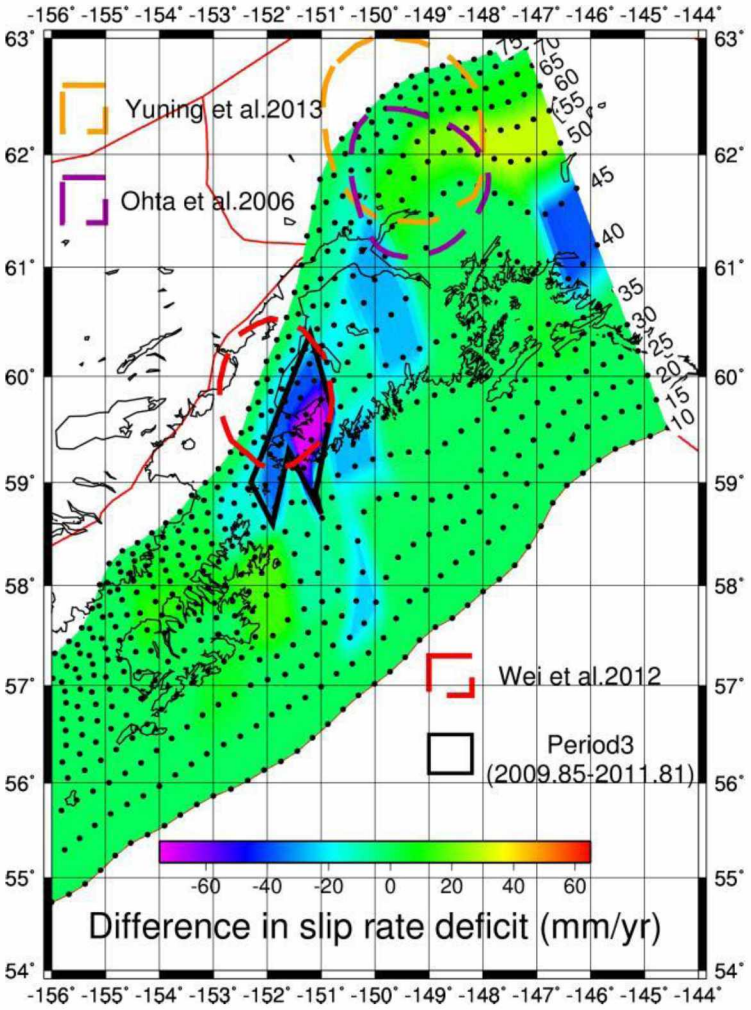

Figure 2.21 Inferred slip deficit rate distribution for the newly observed ~2 year long period slow slip event (thick black polygon) in period 3 (2009.85-2011.81). The orange, red and purple dashed circles as in Figure 2.20. The difference between the two model periods (period 3 and period 4 (2011.81-2014.87)) is shown using the same color scale as Figures 2.15-2.18.

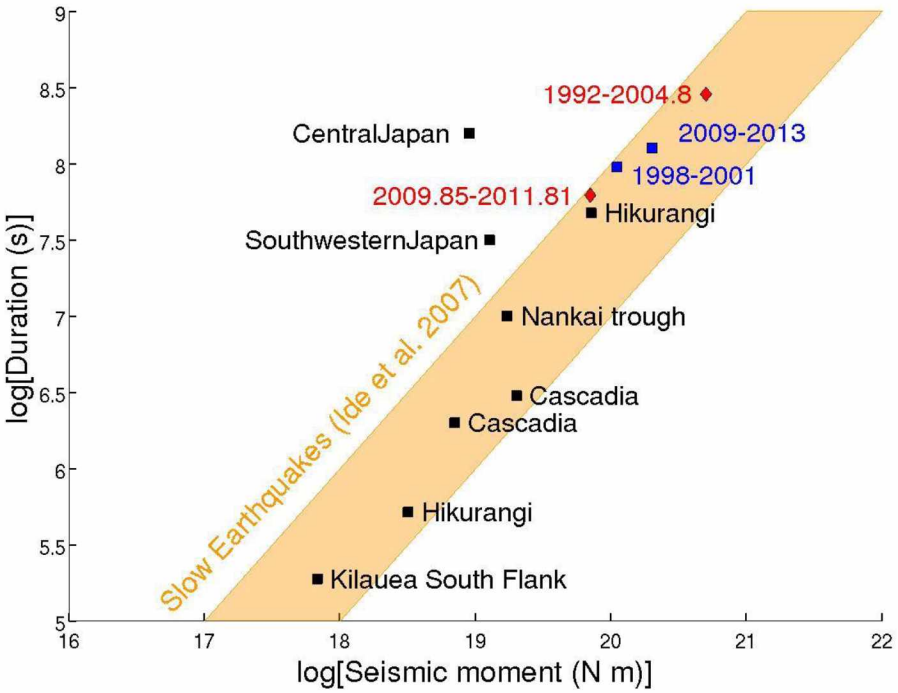

Figure 2.22 Moment versus duration of slow slip events in the Lower Cook Inlet in periods 1 and 3 compared to some at other subduction zones. The red diamonds shows the Lower Cook Inlet SSEs (this study), and the blue squares show the Upper Cook Inlet SSEs, 1998-2001 (Ohta et al., 2006), and 2009-2013 (Fu and Freymueller, 2013). Black squares show SSEs at other subduction zones (Ide et al., 2007; Kobayashi, 2014; Ochi and Kato, 2013; Wallace and Beavan, 2010). The scaling relation for slow earthquakes as drawn by (Ide et al., 2007), $M_o \propto T$, is shown by an orange shaded area.

Table 2.1 GPS site locations ("Longitude, Latitude"), velocities ("Ve, Vn") and associated uncertainties ("Se, Sn") in the horizontal ("east and north") component, the correlations ("Rho") and names ("Site") for time period 1 (1992.0-2004.8). The units of Ve, Vn, Se and Sn are all mm/yr.

Longitude	Latitude	Ve	Vn	Se	Sn	Rho	Site
210.8677	61.5982	-9.95	-5.89	0.60	0.67	0.000	ATWC
206.6461	59.3703	-6.58	-5.80	0.50	0.59	0.000	AUGL
213.3530	60.2375	-15.25	25.05	0.81	0.72	0.000	CHI1
213.3534	60.2375	-15.89	33.06	0.45	0.55	0.000	CHI3
213.3535	60.2377	-16.00	41.45	0.57	0.60	0.000	CHI4
210.1551	61.1658	-15.19	7.50	0.50	0.58	0.000	CMJV
207.8066	57.6177	-12.76	22.80	0.43	0.54	0.000	KDK1
208.6498	60.6751	-4.47	-0.89	0.43	0.54	0.000	KEN1
207.4986	57.7351	-9.96	16.10	0.48	0.57	0.000	KODK
213.3032	61.0563	-16.04	26.38	0.45	0.55	0.000	POT3
208.2933	59.4457	-5.80	-1.80	0.53	0.60	0.000	SELD
210.2198	61.2292	-12.90	18.57	0.78	0.80	0.000	ZAN1
210.2224	61.1601	-15.70	10.84	1.32	0.93	0.000	1000
209.4486	59.5249	-11.28	14.16	2.06	1.52	0.000	2201
210.4571	61.5712	-18.71	5.01	1.18	0.96	0.000	4A1A
205.8254	56.9411	-10.85	21.62	1.08	0.90	0.000	AHKI
210.9361	60.8931	-14.04	19.84	1.30	0.93	0.000	ALAS
212.7456	60.8841	-21.03	37.13	0.89	0.81	0.000	ANCR
208.3234	59.6737	-4.40	2.17	2.54	2.78	0.000	B86
209.7522	60.4554	-11.50	10.85	1.20	0.97	0.000	BEAR
204.8085	58.2811	-8.18	7.65	0.71	0.68	0.000	BKDM
208.7943	61.6830	-3.89	1.52	0.63	0.65	0.000	BLGA
210.9474	61.5459	-6.76	3.67	1.81	1.24	0.000	BODE
209.1481	59.7551	-8.43	7.08	0.63	0.63	0.000	BRAD
210.8152	60.8043	-12.56	21.40	0.59	0.63	0.000	C85G
207.8421	57.6187	1.04	17.93	3.45	1.98	0.000	CHIN
211.9871	60.0685	-23.78	53.26	0.63	0.65	0.000	CHNG
211.4632	61.7647	-13.65	16.39	4.11	2.98	0.000	CKLN
207.4938	57.6522	-11.99	16.34	1.86	1.35	0.000	CLAM
212.0529	61.0704	-21.61	36.77	2.02	1.49	0.000	COGH
210.2791	60.3830	-16.60	23.17	1.81	1.32	0.000	CPLK
210.2545	60.4894	-13.47	18.05	0.57	0.61	0.000	CPR
208.9700	60.4969	-6.79	-1.65	2.20	1.35	0.000	D79
210.5121	60.6540	-13.10	20.02	0.54	0.60	0.000	DAHL
205.3177	58.0880	-2.41	4.87	1.51	1.21	0.000	DAKA
208.7721	60.5879	-2.93	-5.78	0.78	0.72	0.000	DIAN
212.5536	60.7315	-20.74	42.73	1.05	0.93	0.000	DIXI

Table 2.1 cont.

Longitude	Latitude	Ve	Vn	Se	Sn	Rho	Site
210.4713	61.2575	-15.34	8.83	0.56	0.60	0.000	EAGL
208.0873	59.3605	2.17	-2.65	3.40	2.42	0.000	EBAY
208.1618	60.4846	-3.23	-3.41	0.70	0.71	0.000	EKG3
210.6587	61.4628	-11.10	2.98	2.20	1.42	0.000	EKLU
211.0243	60.8185	-16.67	23.81	1.80	1.24	0.000	ENDI
211.9173	60.5959	-22.04	45.12	0.81	0.79	0.000	ENUN
210.7650	61.7168	-6.42	6.78	2.00	1.53	0.000	FSHK
210.1176	61.5247	-8.34	4.13	0.68	0.71	0.000	FSHL
211.6081	60.7067	-16.82	38.62	0.85	0.77	0.000	GAIN
210.7103	61.7283	-8.12	3.23	0.62	0.65	0.000	GOVP
210.4185	60.5644	-13.78	19.56	0.97	0.80	0.000	GRAV
208.6804	60.5796	-1.37	-1.79	0.77	0.72	0.000	H81
211.9086	61.0056	-21.00	31.98	0.78	0.71	0.000	HAM
207.7288	60.3903	-0.51	-5.72	1.43	1.18	0.000	HAR3
210.2807	61.1061	-12.90	9.74	1.17	0.88	0.000	HILS
208.5085	59.6390	-6.34	-1.73	0.51	0.57	0.000	HOMA
210.9521	60.8415	-16.05	23.33	1.00	0.83	0.000	INCK
210.4651	60.9831	-12.41	12.27	1.58	1.03	0.000	INDI
210.2544	61.0207	-13.57	8.66	1.22	0.83	0.000	ISLZ
210.3564	60.1830	-17.86	32.95	1.30	0.90	0.000	JANE
208.7587	60.5789	-0.43	-6.71	0.81	0.76	0.000	KIRT
206.1135	59.8957	-3.24	-6.08	1.92	1.44	0.000	KNUT
207.5027	57.7399	-13.35	15.47	0.56	0.58	0.000	KOD2
209.7841	60.5243	-10.63	11.27	1.05	0.80	0.000	M78
207.8039	57.6140	-7.91	27.04	3.98	1.85	0.000	MCGA
209.3464	60.0888	-9.97	9.71	1.06	0.89	0.000	MENA
210.9440	61.6756	-9.36	6.63	1.13	0.82	0.000	MOS2
212.0922	59.8248	-27.26	55.08	1.12	0.93	0.000	MOTG
209.5173	60.7352	-7.88	9.22	0.89	0.77	0.000	MPEN
210.9730	61.6292	-5.41	4.04	1.65	1.35	0.000	MSB2
209.2631	61.4734	-8.92	11.47	2.32	1.71	0.000	MSUN
208.5702	60.1877	-1.38	-1.05	0.71	0.68	0.000	N82
204.4094	58.6259	-5.50	-0.63	0.91	0.80	0.000	NARM
208.6008	60.6830	-1.40	-2.10	0.90	0.76	0.000	NIK
208.6085	60.6853	-1.93	-3.18	0.65	0.64	0.000	NIK2
208.2842	60.0085	-4.61	-4.01	0.76	0.70	0.000	NINI
204.8399	58.2653	-14.64	3.55	4.85	3.37	0.000	NOVR
210.5490	61.4209	-14.19	5.08	2.07	1.71	0.000	NWOD
210.1003	59.7484	-12.97	20.23	1.23	0.90	0.000	NWP

Table 2.1 cont.

Longitude	Latitude	Ve	Vn	Se	Sn	Rho	Site
210.4529	60.5348	-12.87	21.68	2.13	1.58	0.000	P118
207.5422	57.4360	-15.17	28.58	2.24	1.14	0.000	PASA
210.8841	61.0282	-16.12	18.63	1.45	1.14	0.000	POOR
209.9359	60.4870	-14.60	16.29	1.33	1.09	0.000	POPL
209.9442	60.4850	-13.08	13.38	1.43	1.43	0.000	POPZ
210.5385	61.8883	-6.39	3.98	1.02	0.85	0.000	PRSP
211.1704	60.7712	-15.41	28.73	0.57	0.63	0.000	PRTG
211.9106	61.8046	-4.68	17.72	1.64	1.19	0.000	PURI
207.6963	60.6299	-4.61	-1.81	1.35	1.11	0.000	QRRY
210.6041	61.5424	-9.92	1.81	0.65	0.65	0.000	REED
210.5928	59.8652	-16.97	41.79	0.76	0.71	0.000	RGGI
212.0671	60.6537	-22.00	44.72	0.90	0.79	0.000	ROC
210.5582	61.5805	-5.88	-1.36	3.36	1.86	0.000	S1
210.1294	61.6443	-5.72	5.05	1.16	0.88	0.000	S103
209.2686	60.5297	-8.15	4.44	0.78	0.70	0.000	S79R
205.8641	56.5403	-15.03	31.63	0.80	0.72	0.000	SITK
207.3906	57.8023	-11.91	12.80	0.97	0.90	0.000	SKI
209.7042	60.3529	-12.36	13.93	1.48	1.18	0.000	SKLK
208.9478	60.4752	-2.12	3.13	1.14	0.95	0.000	SXQC
208.9583	60.4759	-8.51	0.15	2.21	1.63	0.000	SXQD
210.9425	61.6573	-8.60	10.82	2.52	1.56	0.000	T18N
210.5714	60.1192	-16.10	34.38	0.73	0.69	0.000	T19
210.7304	61.7729	-9.20	4.38	1.66	1.09	0.000	T20N
211.9098	60.3627	-22.92	50.25	0.67	0.67	0.000	THIN
210.5797	60.5015	-15.24	24.75	0.52	0.60	0.000	TRLK
210.4567	60.9305	-13.07	13.84	0.85	0.81	0.000	TURN
210.6293	60.4286	-18.37	33.17	4.95	3.59	0.000	U76
210.5576	60.0985	-13.60	33.71	0.55	0.59	0.000	UAMF
205.0391	58.4290	-5.39	1.44	0.83	0.70	0.000	UNAM
210.1881	60.4906	-16.93	21.58	2.50	1.90	0.000	V77
210.0472	61.1745	-9.08	8.02	1.24	0.87	0.000	VDUS
213.7488	61.1328	-17.35	30.23	4.10	2.52	0.000	VDZW
208.7560	60.3317	-1.92	-2.66	0.87	0.80	0.000	W81
208.2380	59.9019	-5.33	-5.59	1.69	1.22	0.000	W86
210.6098	59.9868	-15.03	40.27	1.42	1.15	0.000	WLKR
209.9476	61.7542	-3.30	2.02	1.26	0.94	0.000	Z22A
208.3807	60.0808	-4.72	-5.94	0.86	0.78	0.000	Z82

Table 2.2 GPS site locations ("Longitude, Latitude"), velocities ("Ve, Vn") and associated uncertainties ("Se, Sn") in the horizontal ("east and north") component, the correlations ("Rho") and names ("Site") for time period 2 (2004.8-2009.85). The units of Ve, Vn, Se, and Sn are all mm/yr.

Longitude	Latitude	Ve	Vn	Se	Sn	Rho	Site
205.3017	59.8993	-4.58	-1.98	0.52	0.60	0.000	AB22
205.8170	56.9506	-15.68	22.37	0.49	0.58	0.000	AC02
208.1355	59.7706	-9.54	2.19	0.68	0.75	0.000	AC03
209.1094	59.7636	-10.02	10.02	0.48	0.58	0.000	AC06
206.3553	58.9288	-8.21	5.99	0.70	0.74	0.000	AC08
212.0004	60.8487	-21.16	41.94	0.64	0.70	0.000	AC14
210.2760	60.4813	-15.60	24.86	0.48	0.58	0.000	AC15
211.9068	60.5182	-22.22	47.85	0.61	0.69	0.000	AC16
207.5961	60.6639	-5.04	-0.26	0.53	0.62	0.000	AC17
210.6475	60.9292	-17.84	24.34	0.47	0.57	0.000	AC20
209.1221	60.4751	-9.70	3.51	0.60	0.68	0.000	AC23
203.3472	58.6816	-7.12	1.17	0.52	0.61	0.000	AC24
205.8371	59.2525	-6.90	-0.99	0.46	0.56	0.000	AC27
209.2631	61.4731	-11.31	6.61	0.54	0.63	0.000	AC32
206.7208	57.2200	-17.96	22.14	0.52	0.61	0.000	AC34
209.2067	59.3758	-14.87	16.82	0.52	0.61	0.000	AC35
209.3916	60.9553	-11.46	1.33	0.74	0.80	0.000	AC36
206.1346	60.4397	-1.38	-1.83	0.68	0.73	0.000	AC37
206.6581	57.7537	-11.94	12.54	0.47	0.57	0.000	AC38
207.6059	58.6097	-7.41	5.06	0.51	0.60	0.000	AC39
210.3713	59.5213	-16.33	38.88	0.62	0.70	0.000	AC43
205.8190	56.5645	-16.35	29.43	0.52	0.61	0.000	AC45
208.4760	61.9863	-7.58	-0.06	0.52	0.61	0.000	AC46
207.3761	60.0814	-8.38	1.66	0.68	0.73	0.000	AC47
212.6570	60.6459	-21.65	44.94	0.63	0.70	0.000	AC48
208.1646	61.4981	-5.14	-2.17	0.64	0.71	0.000	AC51
209.9310	61.7690	-10.68	9.13	0.52	0.61	0.000	AC53
206.4148	59.5672	-7.10	-2.30	0.46	0.56	0.000	AC59
207.5746	57.7907	-13.94	21.45	0.52	0.61	0.000	AC67
206.5392	59.3585	-7.64	-1.52	0.52	0.61	0.000	AV01
206.5716	59.3330	-7.88	-1.60	0.52	0.61	0.000	AV02
206.5553	59.3626	-5.00	-2.99	0.54	0.62	0.000	AV04
206.6453	59.3706	-7.88	-1.35	0.53	0.62	0.000	AV11
206.4650	59.3859	-7.90	-1.30	0.53	0.62	0.000	AV16

Table 2.2 cont.

Longitude	Latitude	Ve	Vn	Se	Sn	Rho	Site
206.5486	59.4040	-8.59	-1.31	0.54	0.62	0.000	AV17
206.5632	59.3804	-1.83	-0.41	0.53	0.62	0.000	AV18
206.5857	59.3549	-6.11	-3.98	0.54	0.62	0.000	AV19
206.5718	59.3474	-6.69	-2.59	0.55	0.62	0.000	AV20
210.1368	61.1557	-14.71	14.97	0.50	0.59	0.000	ACCU
210.0032	61.1824	-14.22	17.22	0.49	0.58	0.000	ANC1
210.8677	61.5977	-16.07	19.42	0.45	0.56	0.000	ATW2
213.3534	60.2375	-14.58	29.74	0.55	0.64	0.000	CHI3
213.3535	60.2377	-15.16	31.45	0.55	0.63	0.000	CHI4
213.3534	60.2375	-19.88	35.75	1.13	1.01	0.000	CHI5
207.8066	57.6177	-13.15	24.50	0.57	0.65	0.000	KDK1
207.8061	57.6176	-13.21	25.22	0.57	0.65	0.000	KDK2
208.6498	60.6751	-9.20	3.77	0.55	0.64	0.000	KEN1
208.6498	60.6748	-7.67	2.50	0.57	0.64	0.000	KEN2
208.6498	60.6751	-2.75	-0.45	0.65	0.71	0.000	KEN5
208.6498	60.6748	-3.62	0.30	0.69	0.73	0.000	KEN6
207.8066	57.6177	-13.79	26.43	0.60	0.68	0.000	KOD5
207.8061	57.6176	-12.86	27.26	0.61	0.68	0.000	KOD6
207.4986	57.7351	-10.62	22.05	6.36	4.11	0.000	KODK
213.3032	61.0563	-15.98	29.02	0.55	0.63	0.000	POT3
213.3026	61.0563	-15.39	28.36	0.55	0.63	0.000	POT4
213.3032	61.0563	-16.56	27.37	0.65	0.71	0.000	POT5
213.3026	61.0563	-16.67	27.70	0.65	0.71	0.000	POT6
208.2933	59.4457	-5.97	3.53	0.46	0.56	0.000	SELD
207.7908	61.2003	-6.36	-3.18	1.13	1.04	0.000	SPCR
210.2149	61.1797	-15.97	16.57	0.52	0.60	0.000	TBON
210.1050	61.1873	-14.05	15.79	0.47	0.56	0.000	TSEA
210.1759	61.1911	-14.24	17.61	0.47	0.57	0.000	UAAG
210.2198	61.2292	-14.72	16.71	0.47	0.56	0.000	ZAN1
213.6404	61.1272	-16.61	26.71	1.43	1.04	0.000	4240
209.7522	60.4554	-11.86	17.29	3.81	2.37	0.000	BEAR
211.4632	61.7647	-21.04	21.17	1.31	1.03	0.000	CKLN
210.2545	60.4894	-15.40	25.12	1.13	0.89	0.000	CPR
210.5121	60.6540	-16.17	27.69	0.92	0.81	0.000	DAHL
210.1176	61.5247	-12.82	13.65	0.79	0.74	0.000	FSHL

Table 2.2 cont.

Longitude	Latitude	Ve	Vn	Se	Sn	Rho	Site
213.7080	60.6396	-11.64	32.27	1.15	0.88	0.000	GRIS
213.2963	60.7230	-16.30	30.32	0.57	0.62	0.000	GULL
208.5085	59.6390	-7.84	5.67	1.30	1.03	0.000	HOMA
210.2544	61.0207	-15.67	20.69	0.93	0.73	0.000	ISLZ
213.3229	60.9434	-16.95	28.75	0.91	0.84	0.000	MIST
210.9440	61.6756	-14.93	17.12	0.87	0.77	0.000	MOS2
209.5173	60.7352	-8.13	14.59	1.92	1.38	0.000	MPEN
213.9236	60.7450	-12.96	32.53	0.85	0.76	0.000	NATI
208.2842	60.0085	-7.75	2.73	0.69	0.68	0.000	NINI
211.9106	61.8046	-17.35	19.70	0.95	0.83	0.000	PURI
210.6041	61.5424	-15.69	18.26	0.67	0.66	0.000	REED
213.6420	60.4478	-15.78	28.55	1.11	0.93	0.000	RUB2
210.1294	61.6443	-16.19	12.25	0.89	0.79	0.000	S103
208.9478	60.4752	-5.47	9.30	1.08	0.92	0.000	SXQC
210.5797	60.5015	-16.53	28.48	1.26	1.03	0.000	TRLK
210.4567	60.9305	-15.03	18.52	0.68	0.69	0.000	TURN
210.5576	60.0985	-16.03	30.68	1.75	1.15	0.000	UAMF
210.6098	59.9868	-29.01	33.60	2.71	1.68	0.000	WLKR

Table 2.3 GPS site locations ("Longitude, Latitude"), velocities ("Ve, Vn") and associated uncertainties ("Se, Sn") in the horizontal ("east and north") component, the correlations ("Rho") and names ("Site") for time period 3 (2009.85-2011.81). The units of Ve, Vn, Se, and Sn are all mm/yr.

Longitude	Latitude	Ve	Vn	Se	Sn	Rho	Site
205.3017	59.8993	-3.95	-1.41	0.71	0.76	0.000	AB22
205.8170	56.9506	-15.38	25.09	0.69	0.74	0.000	AC02
208.1355	59.7706	-0.01	-4.42	0.67	0.74	0.000	AC03
209.1094	59.7636	-6.85	6.53	0.69	0.75	0.000	AC06
206.3553	58.9288	-7.62	6.33	0.72	0.76	0.000	AC08
212.0004	60.8487	-19.10	42.91	0.73	0.77	0.000	AC14
210.2760	60.4813	-15.16	17.79	0.70	0.75	0.000	AC15
211.9068	60.5182	-18.23	46.94	0.68	0.74	0.000	AC16
207.5961	60.6639	-4.17	-3.23	0.68	0.74	0.000	AC17
207.7505	58.9260	-9.01	3.12	0.69	0.75	0.000	AC18
210.6475	60.9292	-16.67	18.27	0.72	0.76	0.000	AC20
209.1221	60.4751	-10.64	1.01	0.68	0.74	0.000	AC23
203.3472	58.6816	-6.92	1.51	0.68	0.74	0.000	AC24
205.8497	58.2146	-9.45	9.42	0.69	0.74	0.000	AC26
205.8371	59.2525	-6.87	-0.21	0.71	0.75	0.000	AC27
209.2631	61.4731	-6.76	4.50	0.68	0.74	0.000	AC32
206.7208	57.2200	-18.07	23.24	0.69	0.74	0.000	AC34
209.2067	59.3758	-5.47	7.93	0.69	0.75	0.000	AC35
209.3916	60.9553	-9.94	6.57	0.68	0.74	0.000	AC36
206.1346	60.4397	-2.69	-2.04	0.68	0.74	0.000	AC37
206.6581	57.7537	-12.29	12.99	0.71	0.76	0.000	AC38
207.6059	58.6097	-8.39	3.75	0.67	0.74	0.000	AC39
210.3713	59.5213	-13.11	39.54	0.67	0.74	0.000	AC43
210.4329	61.2422	-15.27	11.04	0.68	0.74	0.000	AC44
205.8190	56.5645	-15.45	29.88	0.69	0.75	0.000	AC45
208.4760	61.9863	-5.24	-0.03	0.67	0.74	0.000	AC46
207.3761	60.0814	-2.72	-4.01	0.69	0.75	0.000	AC47
212.6570	60.6459	-20.95	43.16	0.67	0.74	0.000	AC48
208.1646	61.4981	-4.62	-0.73	0.67	0.74	0.000	AC51
209.9310	61.7690	-8.09	5.05	0.68	0.74	0.000	AC53
206.4148	59.5672	-5.28	-1.19	0.68	0.74	0.000	AC59
207.5746	57.7907	-15.14	20.88	0.69	0.75	0.000	AC67
206.5392	59.3585	-6.74	-1.57	0.70	0.75	0.000	AV01
206.5716	59.3330	-6.51	-0.60	0.69	0.74	0.000	AV02

Table 2.3 cont.

Longitude	Latitude	Ve	Vn	Se	Sn	Rho	Site
206.5553	59.3626	-2.41	-1.49	0.78	0.79	0.000	AV04
206.6453	59.3706	-5.49	-1.54	0.69	0.75	0.000	AV11
206.4650	59.3859	-5.96	-1.42	0.70	0.75	0.000	AV16
206.5486	59.4040	-5.73	-1.04	0.69	0.75	0.000	AV17
206.5632	59.3804	0.46	-0.88	0.70	0.75	0.000	AV18
206.5857	59.3549	-3.97	-3.83	0.76	0.76	0.000	AV19
206.5718	59.3474	-4.73	-1.54	0.72	0.76	0.000	AV20
210.1368	61.1557	-14.89	11.73	0.72	0.76	0.000	ACCU
210.0166	61.1752	-13.99	9.94	0.70	0.76	0.000	ANC2
210.8677	61.5977	-12.94	9.33	0.68	0.75	0.000	ATW2
213.3534	60.2375	-14.08	30.70	1.24	1.08	0.000	CHI5
208.6498	60.6751	-6.27	-2.22	0.71	0.76	0.000	KEN5
208.6498	60.6748	-7.24	-1.11	0.77	0.79	0.000	KEN6
207.8066	57.6177	-14.66	27.31	0.68	0.74	0.000	KOD5
207.8061	57.6176	-14.60	28.36	0.68	0.74	0.000	KOD6
213.3032	61.0563	-20.09	19.72	0.72	0.75	0.000	POT5
213.3026	61.0563	-15.70	26.31	0.69	0.74	0.000	POT6
208.2933	59.4457	-6.78	-1.84	0.69	0.74	0.000	SELD
207.6276	61.2591	-2.17	5.16	0.72	0.76	0.000	SPBG
207.9776	61.2912	-4.59	-0.80	0.69	0.75	0.000	SPCG
207.7908	61.2003	-4.13	-2.34	0.70	0.76	0.000	SPCR
210.2149	61.1797	-15.03	10.45	0.68	0.74	0.000	TBON
210.1050	61.1873	-14.54	9.42	0.68	0.74	0.000	TSEA
210.1759	61.1911	-15.28	10.97	0.68	0.75	0.000	UAAG
210.2198	61.2292	-13.93	9.60	0.68	0.75	0.000	ZAN1

Table 2.4 GPS site locations ("Longitude, Latitude"), velocities ("Ve, Vn") and associated uncertainties ("Se, Sn") in the horizontal ("east and north") component, the correlations ("Rho") and names ("Site") for time period 4 (2011.81-2014.87). The units of Ve, Vn, Se, and Sn are all mm/yr.

Longitude	Latitude	Ve	Vn	Se	Sn	Rho	Site
205.3017	59.8993	-6.98	-1.29	0.55	0.63	0.000	AB22
205.8170	56.9506	-15.63	21.26	0.54	0.62	0.000	AC02
208.1355	59.7706	-10.76	4.64	0.53	0.62	0.000	AC03
209.1094	59.7636	-11.98	13.91	0.53	0.62	0.000	AC06
206.3553	58.9288	-10.62	6.43	0.55	0.63	0.000	AC08
210.2760	60.4813	-18.61	23.70	0.54	0.62	0.000	AC15
207.5961	60.6639	-7.85	0.59	0.53	0.62	0.000	AC17
207.7505	58.9260	-9.27	6.28	0.54	0.62	0.000	AC18
210.6475	60.9292	-19.23	19.82	0.54	0.62	0.000	AC20
209.1221	60.4751	-11.61	10.98	0.53	0.62	0.000	AC23
203.3472	58.6816	-8.22	1.01	0.54	0.62	0.000	AC24
205.8497	58.2146	-8.10	8.41	0.54	0.62	0.000	AC26
209.2631	61.4731	-9.35	7.69	0.54	0.62	0.000	AC32
206.7208	57.2200	-18.33	22.33	0.54	0.62	0.000	AC34
209.2067	59.3758	-15.02	19.02	0.53	0.62	0.000	AC35
209.3916	60.9553	-12.35	13.43	0.53	0.62	0.000	AC36
206.1346	60.4397	-6.10	-0.37	0.54	0.62	0.000	AC37
206.6581	57.7537	-14.30	13.04	0.55	0.63	0.000	AC38
207.6059	58.6097	-9.33	5.27	0.53	0.62	0.000	AC39
210.3713	59.5213	-18.19	40.01	0.53	0.62	0.000	AC43
210.4329	61.2422	-16.64	17.39	0.53	0.62	0.000	AC44
205.8190	56.5645	-17.63	29.08	0.54	0.62	0.000	AC45
209.9310	61.7690	-10.81	9.82	0.53	0.62	0.000	AC53
206.4148	59.5672	-8.80	-1.08	0.54	0.62	0.000	AC59
207.5746	57.7907	-14.67	18.05	0.54	0.62	0.000	AC67
212.5970	59.9979	-19.43	50.10	0.53	0.62	0.000	AC79
206.5392	59.3585	-9.19	-0.43	0.54	0.62	0.000	AV01
206.5716	59.3330	-8.94	-0.56	0.54	0.62	0.000	AV02
206.6453	59.3706	-9.23	-0.77	0.54	0.62	0.000	AV11
206.4650	59.3859	-9.04	-0.79	0.54	0.62	0.000	AV16
206.5486	59.4040	-9.51	-0.62	0.54	0.62	0.000	AV17
206.5632	59.3804	-4.10	-0.70	0.54	0.63	0.000	AV18
206.5718	59.3474	-8.88	-0.08	0.54	0.62	0.000	AV20

Table 2.4 cont.

Longitude	Latitude	Ve	Vn	Se	Sn	Rho	Site
210.0166	61.1752	-14.66	16.18	0.53	0.62	0.000	ANC2
210.8677	61.5977	-16.79	12.09	0.53	0.62	0.000	ATW2
213.3534	60.2375	-17.65	32.38	0.54	0.62	0.000	CHI5
213.3535	60.2377	-17.67	32.81	0.57	0.65	0.000	CHI6
208.4688	59.6417	-10.61	7.69	0.53	0.62	0.000	HDPW
208.6498	60.6751	-9.89	6.85	0.54	0.62	0.000	KEN5
208.6498	60.6748	-10.45	5.50	0.56	0.63	0.000	KEN6
207.8061	57.6176	-16.35	27.19	0.54	0.62	0.000	KOD6
208.7422	59.7461	-9.95	10.42	0.53	0.62	0.000	MCES
208.7278	59.5727	-10.02	11.49	0.53	0.62	0.000	PBAY
213.3032	61.0563	-17.45	29.57	0.53	0.62	0.000	POT5
213.3026	61.0563	-16.43	28.86	0.53	0.62	0.000	POT6
207.1948	60.5908	-8.08	-1.68	0.54	0.62	0.000	RDJH
207.1564	60.4868	-7.88	-0.04	0.53	0.62	0.000	RDWB
208.2933	59.4457	-10.90	7.65	0.54	0.62	0.000	SELD
207.6276	61.2591	-4.85	3.67	0.55	0.63	0.000	SPBG
207.9776	61.2912	-8.42	1.61	0.56	0.64	0.000	SPCG
207.8445	61.2655	-8.63	1.81	0.54	0.62	0.000	SPCP
207.7908	61.2003	-7.41	2.72	0.53	0.62	0.000	SPCR
210.2149	61.1797	-15.75	16.36	0.53	0.62	0.000	TBON
210.1050	61.1873	-15.49	16.75	0.53	0.62	0.000	TSEA
210.1759	61.1911	-14.76	13.26	0.77	0.81	0.000	UAAG
210.2198	61.2292	-15.19	16.56	0.54	0.62	0.000	ZAN1
209.4486	59.5249	-17.61	19.01	1.11	0.94	0.000	2201
210.9361	60.8931	-10.37	22.91	1.97	1.29	0.000	ALAS
208.3234	59.6737	-13.15	8.54	2.53	1.87	0.000	B86
209.7522	60.4554	-10.63	15.00	2.60	1.97	0.000	BEAR
211.4632	61.7647	1.14	11.76	3.00	2.30	0.000	CKLN
210.2791	60.3830	-19.37	24.35	1.36	1.18	0.000	CPLK
210.2545	60.4894	-23.43	15.80	1.33	1.12	0.000	CPR
210.5121	60.6540	-17.02	25.15	2.74	2.12	0.000	DAHL
206.8262	59.6773	-11.02	-0.89	1.21	0.95	0.000	DRYB
208.0061	58.9128	-11.57	9.94	2.97	1.78	0.000	EAMA
208.0873	59.3605	-10.11	1.86	1.82	1.43	0.000	EBAY
210.1176	61.5247	-6.71	12.17	1.83	1.60	0.000	FSHL
210.4185	60.5644	-20.25	23.54	2.60	1.66	0.000	GRAV

Table 2.4 cont.

Longitude	Latitude	Ve	Vn	Se	Sn	Rho	Site
208.5085	59.6390	-9.23	9.50	1.49	1.20	0.000	HOMA
210.9521	60.8415	-19.86	25.79	1.42	1.17	0.000	INCK
210.2544	61.0207	-15.14	16.78	1.31	1.00	0.000	ISLZ
210.3564	60.1830	-15.51	33.02	1.59	1.09	0.000	JANE
206.1135	59.8957	-8.29	-3.78	1.55	1.17	0.000	KNUT
210.9440	61.6756	-20.06	15.55	1.62	1.26	0.000	MOS2
209.5173	60.7352	-10.26	12.76	2.34	1.60	0.000	MPEN
208.2842	60.0085	-9.35	5.77	1.04	0.91	0.000	NINI
210.1003	59.7484	-6.98	30.45	1.79	1.17	0.000	NWP
209.9359	60.4870	-20.45	22.15	1.34	1.13	0.000	POPL
211.9106	61.8046	-13.81	22.26	1.40	1.22	0.000	PURI
210.6041	61.5424	-12.83	14.57	1.72	1.47	0.000	REED
210.5928	59.8652	-20.68	40.84	1.18	1.04	0.000	RGGI
209.2686	60.5297	-15.26	11.59	2.49	1.78	0.000	S79R
208.9478	60.4752	-13.60	9.85	2.18	1.70	0.000	SXQC
208.9583	60.4759	-12.99	8.29	1.31	1.11	0.000	SXQD
210.5797	60.5015	-17.04	30.21	2.16	1.83	0.000	TRLK
210.4567	60.9305	-18.15	18.08	1.35	1.19	0.000	TURN
210.5576	60.0985	-18.30	36.30	1.37	1.05	0.000	UAMF
209.9674	59.7901	-13.31	29.58	1.24	1.00	0.000	UNF
208.7560	60.3317	-16.79	-1.85	2.73	2.05	0.000	W81
210.6098	59.9868	-27.83	36.54	2.02	1.33	0.000	WLKR
208.3807	60.0808	-13.72	12.61	3.00	2.09	0.000	Z82

Table 2.5 Block Poles, Location of Poles and Angular Speed of the block model, relative to the North American plate. Negative rotations are clockwise looking from above.

Block Name	Latitude of Pole	Longitude of Pole	Angular Speed (deg/Ma)	Source
SOAK	59.6000	212.6002	0.7700	[Fletcher, 2002]
PCFC	50.1734	284.1136	-0.7696	[Sella et al., 2007]
BRNG	43.9007	125.6082	-0.0638	[Cross and Freymueller, 2008]
PENN	60.481	58.666	-0.066	This study (section 2.4.2)

Table 2.6 GPS site locations ("Longitude, Latitude"), velocities ("Ve, Vn") and associated uncertainties ("Se, Sn") in the horizontal ("east and north") component, the correlations ("Rho") and names ("Site") for combined data set of periods 1 and 4 in the Alaska. Sites in the Alaska Peninsula will be added into the combined data set from Table 2.1 and Table 2.4 in estimating the pole of rotation in the PENN bock. The units of Ve, Vn, Se and Sn are all mm/yr.

Longitude	Latitude	Ve	Vn	Se	Sn	Rho	Site
197.2928	55.1903	-4.97	-1.86	0.45	0.54	0.000	BAY1
197.2932	55.1904	-5.26	-1.96	0.46	0.55	0.000	BAY2
196.5765	54.8853	-3.77	-1.84	0.57	0.63	0.000	AB06
199.5232	55.3493	-8.76	3.04	0.55	0.62	0.000	AB07
201.4962	56.3073	-10.60	6.46	0.56	0.63	0.000	AB13
199.3053	63.8864	-2.30	-1.03	0.54	0.62	0.000	AB17
198.7134	65.9613	0.79	-2.48	0.54	0.62	0.000	AC07
195.1133	54.5226	-7.08	-1.46	0.57	0.63	0.000	AC10
200.4104	54.8310	-9.44	7.75	0.55	0.63	0.000	AC12
200.8723	55.9211	-10.30	5.53	0.55	0.62	0.000	AC21
199.9508	55.0785	-9.00	4.38	0.55	0.62	0.000	AC28
197.7609	64.6380	0.39	-2.68	0.54	0.62	0.000	AC31
199.5927	55.9087	-8.86	1.51	0.56	0.63	0.000	AC41
195.4334	65.5538	1.49	-3.55	0.55	0.63	0.000	AC50
202.4258	57.5673	-10.56	3.45	0.54	0.62	0.000	AC52
197.2928	55.1903	-5.19	-1.70	0.56	0.63	0.000	BAY5
197.6307	54.6290	-2.15	-1.49	2.17	1.71	0.000	CHRN
197.1990	54.4908	-2.90	-1.83	0.55	0.58	0.000	CROW
197.6448	54.8246	-5.05	-4.74	4.01	2.93	0.000	FAWN
201.3877	56.9639	-6.71	1.71	0.84	0.73	0.000	HEID
199.5048	55.3021	-8.62	3.25	0.48	0.55	0.000	LSDP
197.3810	54.3839	-3.32	-2.20	0.51	0.56	0.000	PETE
197.4770	54.8574	0.28	7.00	2.54	1.76	0.000	REEF
199.5245	55.3530	-10.67	-6.62	6.75	3.16	0.000	SDP1
199.5245	55.3523	-7.47	-3.72	5.15	3.63	0.000	SNDP
197.3953	54.9844	-1.94	1.11	1.51	1.17	0.000	TELE

Table 2.7 The variance for the selected boxes in four time periods.

		ϕ : [-2, 1]	ϕ : [0, 1]	Difference
1992.0 - 2004.8	Variance for blue box $(mm/yr)^2$	1175.66	1931.86	756.19
1992.0 - 2004.8	Variance for red box $(mm/yr)^2$	1227.09	1972.95	745.86
2004.8 - 2009.85	Variance for red box $(mm/yr)^2$	441.932	529.613	87.6810
2009.85 – 2011.81	Variance for red box $(mm/yr)^2$	307.33	536.72	229.39
2011.81 – 2014.87	Variance for red box $(mm/yr)^2$	907.615	971.264	63.6490

Chapter 3

Correlation between Seismicity Rate Changes and Coulomb Stressing Rate Changes due to Slow Slip Events in Lower Cook Inlet, Alaska-Aleutian Subduction Zone[2]

3.1 Abstract

Two long-term slow slip events (SSEs) in Lower Cook Inlet, Alaska were identified by Li et al. (2016). The earlier SSE lasted at least 9 years with Mw~7.8 and had an average slip rate of ~82 mm/yr. The latter SSE occurred over similar area, had a duration of ~2 years with Mw~7.2 and an average slip rate of ~91 mm/yr. In order to test whether these SSEs triggered earthquakes outside the slow slip area, we resolved the Coulomb stressing rate changes on receiver faults using two possible fault geometry definitions: the nodal planes of focal mechanism solutions of past earthquakes, and optimally oriented fault planes. Regions in the shallow slab (30 – 60 km) that experienced significant increase in Coulomb stressing rate due to SSEs slip show an increase in seismicity rate during SSE periods. Significant correlations within the crust (0 – 30 km) and the intermediate slab (60 – 90 km) are not observed, which are attributable to the negligible Coulomb stress changes. We model variations in seismicity rate using the modified rate/state stress transfer model (Dieterich, 1994). This modeling indicates that the SSEs increase stress on adjacent faults, thereby increasing the seismicity rate even though the ratio of the SSE stressing rate to the background stressing rate is small. Each SSE in Alaska brought the megathrust updip of the SSE closer to failure by up to 0.1-0.15 MPa. The areas of significant Coulomb stress changes caused by the Upper and Lower Cook Inlet SSEs do not overlap.

[2] Li, S., J. Freymueller, J. Wang and N. Ruppert, (submitted), Correlation between Coulomb Stress Rate Change imparted by the Slow Slip Events and Seismic Rate Change in Lower Cook Inlet of the Alaska-Aleutian Subduction Zone, *Journal of Geophysical Research: Solid Earth*.

3.2 Introduction

Slow slip events (SSE), which slip slower than regular tectonic earthquakes but faster than steady plate motion, have been identified on the plate interface in many subduction zones (Dragert et al., 2001; Kostoglodov et al., 2003; Li et al., 2016; Ochi & Kato, 2013; Schwartz & Rokosky, 2007; Szeliga et al., 2004; Wallace & Beavan, 2010). Considerable variations have been observed in the duration, location, moment magnitude, slip amount and slip rate of SSEs globally (Li et al., 2016). SSEs play a crucial role in the cycle of strain accumulation and release on subduction megathrusts.

SSEs in Japan (Hirose et al., 2010; Ide, 2012), Cascadia (Rogers & Dragert, 2003), Mexico (Payero et al., 2008), New Zealand (Kim et al., 2011), the San Andreas fault (Nadeau & Dolenc, 2005), Ryukyu subduction zone (Arai et al., 2016) and Costa Rica (Walter et al., 2011) are often accompanied by non-volcanic tremor (NVT) which is seismic waves generated by a small percentage of slip during an SSE, and irregular earthquakes such as low frequency earthquakes (LFE) and very low frequency earthquakes (VLFE). Most of these detected tremors were highly correlated with the SSEs spatially and temporally, and occurred at the downdip edge of the slip zone.

In some areas, SSEs have been shown to have a close relationship with regular earthquakes. For instance, Ito et al. (2013) showed that two transient SSEs occurred before the 2011 Tohoku-Oki earthquake, inducing increased shear stress on the plate interface. The latter SSE triggered an M7.3 interplate earthquake, which was the largest foreshock of the 2011 Tohoku-Oki earthquake. SSEs on Kilauea volcano, Hawaii, caused dramatic increases in seismicity, which supported their interpretation that slow slip stresses the surrounding fault, thereby increasing the seismicity rate (Segall et al., 2006). However, the underlying physical relationship between regular earthquakes and slow slip events has not been well explored everywhere in the world. It is challenging to study whether SSEs enhance or suppress the occurrence of regular earthquakes on nearby faults due to the shortage of the long-term records of these events and spatially and temporally limited observations.

As noted above, SSEs can be associated with tectonic tremor, LFEs, VLFEs and regular earthquakes. Therefore, the study of SSEs can reveal physical relations among them. Fortunately, the Alaska-Aleutian subduction zone is such a natural laboratory for the study of SSEs because of actively detected SSEs, NVTs, LFEs, VLFEs and regular earthquakes and continuingly augmented

seismic and geodetic network coverage. GPS data in south-central Alaska provide good constraints on the source mechanisms of SSEs. Four long term SSEs have been observed in the Cook Inlet region (Fu & Freymueller, 2013; Li et al., 2016; Ohta et al., 2006). There was a clear spatial correlation between tremor and SSEs in Upper Cook Inlet (Ohta et al., 2006) where most tremors were located near the downdip edge of the SSE (Peterson & Christensen, 2009; Wech, 2016). The second long-term SSE in Upper Cook Inlet was associated with a clear seismicity increase based on analysis of the earthquake catalog in southcentral Alaska (Fu et al., 2015; Fu & Freymueller, 2013). Other two long-duration slow slip events (SSEs) have been detected beneath Lower Cook Inlet (Figure 3.1) (Li et al., 2016). SSEs in Lower Cook Inlet were estimated to occur in the depth range of 40-60 km within the transition zone on the plate interface.

In this paper, we use the inverted slip distribution from GPS displacements (Li et al., 2016) to calculate the Coulomb stressing rate changes (CSRC) due to the two Lower Cook Inlet SSEs resolved on two different definitions of receiver faults. We identified potential stress triggering areas, where the CSRCs were potentially significant, to test for changes in the seismicity rate during the SSE periods. After locating zones with significant stress triggering, we used the modified rate/state model (Dieterich, 1994; Segall et al., 2006) to quantitatively model the ratio of the stressing rate during the SSE to the background stressing rate. Our main goal is to explore how long-term SSEs in Lower Cook Inlet relate with earthquakes in the adjacent areas, and how they impact the strain accumulation along the Alaska-Aleutian subduction margin. Generally speaking, we want to test the triggering hypothesis: are the seismicity rates influenced by changes in stressing rates due to the two SSEs?

3.3 Data

3.3.1 Earthquake Data

We used earthquakes recorded in the Alaska Earthquake Center (AEC) catalog from January 1996 to November 2014 (Figure 3.2a). Multiple changes in sensor characteristics, network configuration, and data recording and processing systems occurred during that time. Earlier years had even larger changes in the network geometry and a much larger magnitude of completeness (Mc). Before July 1999, the location program HYPOELLIPSE was used to calculate locations and magnitudes of the recorded earthquakes from the combined USGS and UAF-GI seismic networks. After July 1999, AEC switched to the program dbloc2, part of the Antelope package (Boulder Real Time Technologies, Inc.), to locate events and calculate local magnitudes (Ruppert & Hansen,

2010). Over this time span, the Alaska regional seismic network greatly expanded its broadband component through AEC and other regional operators (Ruppert & Hansen, 2010). The magnitude of completeness (Mc) varies for different time periods, depth ranges and spatial locations. We used the Matlab-based ZMAP software package to calculate Mc for the regions of interest in this study. The ZMAP software uses the maximum likelihood method and the best combination method (Mc95 – Mc90 – maximum curvature) to estimate Mc (Wiemer, 2001). The overall Mc for Lower Cook Inlet over the whole time span was 1.74, although Mc varies over smaller areas due to heterogeneity in the seismic network. The estimated Mc values for the specific potential stress triggering areas will be introduced in the Results section. All recorded earthquakes in the AEC catalog above the estimated Mc were used to compute the seismicity rate changes throughout the pre-SSE periods, SSE periods and post-SSE periods.

3.3.2 Source faults of the two long-term SSEs

We used the estimated slip distributions for the two SSEs from Li et al. (2016) as the source faults to calculate the stress perturbations caused by the SSEs. We considered two different definitions of receiver faults (section 2.3). The first observed SSE (SSE1) lasted at least 9 years, starting before the earliest GPS data in 1995, with Mw~7.8 and an average slip rate of ~ 82 mm/yr. For this paper, we assumed that SSE1 began in 1995. The second SSE (SSE2) occurred in almost the same area as the first one, and had a duration of ~ 2 years with Mw ~ 7.2 and an average slip rate of ~ 91 mm/yr (Li et al., 2016).

3.3.3 Receiver faults

We considered two different definitions for potential receiver faults in the crust (depth < 30 km) and slab (depth >= 30 km). The first definition of the receiver fault geometry was based on the nodal planes of focal mechanism solutions of past earthquakes in the study region from the AEC catalog. To determine the orientation of the faults that caused these earthquakes, we used the focal mechanism solutions of over 2000 earthquakes from the AEC catalog in the time period (3/4/1990-12/30/2015) (Figure 3.2b). The deepest earthquakes reached about 200 km. The magnitude range of earthquakes in the focal mechanism catalog was between 1.8 and 6.8. The focal mechanism catalog showed that crustal earthquakes exhibited a variety of faulting types across the region. Slab events were mainly dominated by strike-slip and normal faulting in the shallower depth range (<100 km), and strike-slip and thrust faulting at greater depths (Ruppert, 2008).

The second definition for the receiver fault geometry was based on optimally oriented fault planes (OOP) (King et al., 1994; Wang et al., 2014; Xu et al., 2010). OOPs were determined by finding the strike, dip and rake angles that maximize the Coulomb stressing rate change given by the total stress tensor including an assumed regional stress field. In this paper, optimal fault orientations were calculated assuming a regional stress field with 10 MPa horizontal compressional stress oriented N0°E (Ruppert, 2008). The focal mechanism catalog showed that varied types of earthquakes, including normal, thrust and strike-slip faults, happened in the crust and slab over time. Therefore, we searched through the full ranges of strike, dip and rake angles from 0-360, 0-90 and 0-360, respectively, to find the optimally oriented fault planes.

3.4 Method

3.4.1 Coulomb Stressing Rate Change Criteria

We used the Coulomb stress change (ΔCFS) criterion to calculate the stress perturbations caused by the SSEs on the adjacent receiver faults. We used the Okada (Okada, 1992) elastic half-space dislocation model to estimate the change in the stress tensor on the receiver fault due to the source slip distribution. We then projected the estimated stress tensor onto the fault plane to determine the normal stress change ($\Delta\sigma$) and the shear stress change ($\Delta\tau$) in the fault slip direction. Based on the calculated shear stress change ($\Delta\tau$) and normal stress change ($\Delta\sigma$), we estimated the ΔCFS in Equation 3.1 (King et al., 1994):

$$\Delta CFS = \Delta\tau - \mu'\Delta\sigma \quad (3.1)$$

Where $\Delta\tau$ is the shear stress change, assumed positive in the fault slip direction, on a given failure plane, $\Delta\sigma$ is the normal stress change, which is assumed positive in the compressive direction, μ' is the apparent coefficient of friction, defined as $\mu' = \mu(1 - B)$, where B is Skempton's coefficient related to induced pore pressure change, and μ is the coefficient of friction. We tried different values of effective coefficient of friction (0.1, 0.4, and 0.7) and found the results didn't change much, so we chose $\mu' = 0.4$ in this study.

In our previous study (Li et al., 2016), we estimated the slip rates during the two SSEs and recognized that there were limitations in confirming the exact duration of the SSE1 due to the shortage of GPS data before 1995. We used the estimated slip rates (Li et al., 2016) instead of the slip magnitude for each fault patch on the source faults to calculate the CSRC as the time derivative of the ΔCFS. A positive CSRC promotes receiver fault failure due to the SSEs; a negative CSRC

means stress builds up at a slower rate during the SSE, which reduces the chance of failure on those potential receiver faults. We used a shear modulus of 5×10^4 MPa, in a uniform elastic half-space with Poisson's ratio of 0.25.

In this study, we identified potential stress triggering areas due to the two SSEs and estimated the seismicity rate changes in these areas. We chose to work with these selected areas instead of a spatial grid because we needed to average in space to have enough earthquakes for a robust estimate of the seismicity rates and the areas of significant stress change were small. Thus, we needed to select the most appropriate areas over which to average. We focused on the correlation between the CSRC and seismicity rate change in the areas close to the SSEs, where stressing rate changes might be significant. We computed the CSRC over a large area surrounding the SSEs (red dashed outline in Figure 3.1), and chose the potential triggering area based on a threshold value for the stressing rate changes (the specific threshold values will be introduced in the following paragraph). When resolving stressing rate changes on receiver faults defined by the geometry of observed nodal planes, more restrictive stress triggering areas were chosen based on the spatial distribution of the nodal planes that had maximum CSRC exceeding the thresholds. When resolving on receiver faults defined by OOPs, we divided the study area into a grid, and estimated the optimal orientation and calculated the maximum CSRC at each grid point. Then we picked the potential stress triggering areas based on the CSRC thresholds.

The threshold is an important factor in defining the potential stress triggering areas. Dixon et al. (2014) proposed that ΔCFS values larger than 0.1 MPa have been shown to influence aftershock locations and promote subsequent large thrust earthquakes in subduction environments. On the other hand, Ishibe et al. (2015) suggested that ΔCFS larger than 0.01 MPa was a reasonable threshold for static stress triggering. We chose thresholds based on the two criteria above and also a middle value between them in our study. Because the durations of the two SSEs here were different, we converted these thresholds to stressing rate by dividing by the SSE duration. The approximate duration of SSE1 was ~ 9 years, so the thresholds tested for CSRC were 0.001 MPa/year, 0.005 MPa/year and 0.01 MPa/year. The duration of the SSE2 was ~ 2 years, so the thresholds were 0.005 MPa/year, 0.025 MPa/year and 0.05 MPa/year.

3.4.2 Rate/State Stress Transfer Model

We used Dieterich's seismicity rate theory based on the rate/state friction model (Dieterich, 1994) to quantitatively model the seismicity rate changes. Our model domains were the stress

triggering areas chosen in the different depth ranges due to two SSEs. We used the equation for seismicity rate R as a function of the state variable γ under the reference stressing rate $\dot{\tau}_r$ and seismicity rate r in the background time period (Equation 3.2, (Dieterich, 1994)).

$$R = \frac{r}{\gamma \dot{\tau}_r} \quad (3.2)$$

The state variable γ evolves based on

$$d\gamma = \frac{1}{A\sigma}(dt - \gamma d\tau) \quad (3.3)$$

Where A is the constitutive constant, and τ and σ represent the shear and effective normal stress respectively. Variation in normal stress will be mostly balanced by the change in pore fluid pressure so we assumed no changes in normal stress.

Li et al. (2016) provided slip distributions for four time periods, including the SSE1 period (1995-2004.8), the post-SSE1/pre-SSE2 period (2004.8-2009.85), the SSE2 period (2009.85-2011.81) and the post-SSE2 period (2011.81-2014.87). In order to study the triggering effect of each SSE individually, we focused on the SSE1 period and the post-SSE1 period for studying SSE1, and the pre-SSE2, SSE2 and post-SSE2 periods for studying SSE2. We chose 1996 as the starting time instead of 1995 for the SSE1 to avoid the impact of the aftershock sequence following an Mw 5.5 earthquake in May 1995 in the target areas and because the overall Mc for 1995 and earlier was higher than 1996 to present. We used the recorded earthquakes in the post-SSE2 period (2011.81 – 2014.87) in each triggering area to estimate the background seismicity rate because available data were limited before SSE1 and the estimated slip distributions for the four time periods (Li et al. 2016) suggested that the post-SSE2 period was the best estimate of the steady deformation. The background stressing rate was assumed to be the same as the stressing rate during the post-SSE2 period, although the real stressing rate remains uncertain.

We assumed that the stressing rate was $\dot{\tau}_s$ during the SSE1 period, then it decreased to $\dot{\tau}_l$ which might be different from the background stressing rate $\dot{\tau}_r$. We calculated the cumulative number of earthquakes, N(t), by integrating R(t) in Equation 3.2 (modified from Segall et al. 2006):

$$N(t) = \begin{cases} rt_a \ln\left[\frac{\dot{\tau}_r}{\dot{\tau}_s}\left(\exp\left(\frac{\dot{\tau}_s (t-t_0)}{A\sigma}\right) - 1\right) + 1\right], & t_0 < t \le t_1 \\ rt_a \ln\left[\frac{\frac{\dot{\tau}_r}{\dot{\tau}_l}\exp\left(\frac{\dot{\tau}_l (t-t_1)}{A\sigma}\right) + C}{\frac{\dot{\tau}_r}{\dot{\tau}_l} + C}\right] + N(t_1), & t_1 < t \le t_2 \end{cases} \quad (3.4)$$

Where

$$C = \frac{\dot{\tau}_r}{\dot{\tau}_s} - \frac{\dot{\tau}_r}{\dot{\tau}_l} + \left(1 - \frac{\dot{\tau}_r}{\dot{\tau}_s}\right)\exp\left(\frac{-\dot{\tau}_s\,(t_1 - t_0)}{A\sigma}\right) \quad (3.5)$$

When calculating the predicted cumulative number of earthquakes in the SSE1 period and post-SSE1 period (Equations 3.4 and 3.5), the parameter t_a is the typical aftershock duration, $t_a = A\sigma/\dot{\tau}_r$, assuming the modified Omori law (Dieterich, 1994). We set t_a as 30 days based on the observed aftershock decay following an Mw 5.3 earthquake on 27th March 2008. In our study, t_0 is 1996 which was treated as the onset of SSE1, t_1 is 2004.8 which marked the end of SSE1 and t_2 is 2009.85 which was the end of post-SSE1 and also the onset of SSE2. The undetermined parameters were the ratio of the stressing rate during SSE1 to the background stressing rate ($\frac{\dot{\tau}_s}{\dot{\tau}_r}$), and the ratio of the stressing rate during the post-SSE1 period to the background stressing rate ($\frac{\dot{\tau}_l}{\dot{\tau}_r}$).

Compared with SSE1, SSE2 had better seismic network coverage during its time span. We assumed that the stressing rate during the pre-SSE2 period was $\dot{\tau}_l$, then it increased to $\dot{\tau}_p$ once SSE2 started, and decreased again to the background stressing rate $\dot{\tau}_r$ after SSE2 ended. We used the modified Equations 3.6 – 3.8 modifies from equations 3.4 and 3.5 to calculate the cumulative number of earthquakes through these three time periods:

$$N(t) = \begin{cases} rt_a \ln\left[\frac{\dot{\tau}_r}{\dot{\tau}_l}\left(\exp\left(\frac{\dot{\tau}_l\,(t-t_1)}{A\sigma}\right) - 1\right) + 1\right], & t_1 < t \le t_2 \\ rt_a \ln\left[\frac{\frac{\dot{\tau}_r}{\dot{\tau}_p}\exp\left(\frac{\dot{\tau}_p(t-t_2)}{A\sigma}\right) + C_1}{\frac{\dot{\tau}_r}{\dot{\tau}_p} + C_1}\right] + N(t_2), & t_2 < t \le t_3 \\ rt_a \ln\left[\frac{\frac{\dot{\tau}_p}{\dot{\tau}_r}\exp\left(\frac{\dot{\tau}_r(t-t_3)}{A\sigma}\right) + C_2}{\frac{\dot{\tau}_p}{\dot{\tau}_r} + C_2}\right] + N(t_3), & t_3 < t \le t_4 \end{cases} \quad (3.6)$$

Where

$$C_1 = \frac{\dot{\tau}_r}{\dot{\tau}_l} - \frac{\dot{\tau}_r}{\dot{\tau}_p} + \left(1 - \frac{\dot{\tau}_r}{\dot{\tau}_l}\right)\exp\left(\frac{-\dot{\tau}_l(t_2 - t_1)}{A\sigma}\right) \quad (3.7)$$

$$C_2 = 1 - \frac{\dot{\tau}_p}{\dot{\tau}_r} + \left(\frac{\dot{\tau}_p}{\dot{\tau}_l} - 1\right)\exp\left(\frac{-\dot{\tau}_p(t_3 - t_2)}{A\sigma}\right) + \left(\frac{\dot{\tau}_p}{\dot{\tau}_r} - \frac{\dot{\tau}_p}{\dot{\tau}_l}\right)\exp\left(\frac{-\dot{\tau}_p(t_3 - t_2) - \dot{\tau}_l(t_2 - t_1)}{A\sigma}\right) \quad (3.8)$$

In Equations 3.6 -3.8, t_1 was 2004.8, t_2 was 2009.85, t_3 was 2011.81 and t_4 was 2014.87. We still assumed t_a = 30 days. The two undetermined parameters were the ratio of the stressing rate during SSE2 to the background stressing rate ($\frac{\dot{\tau}_p}{\dot{\tau}_r}$), and the ratio of the stressing rate in the post-SSE2 to the background stressing rate ($\frac{\dot{\tau}_1}{\dot{\tau}_r}$).

3.5 Results

We first investigated the correlation between the CSRC and seismicity rate changes and identified the stress triggering areas in different depth ranges due to the SSEs. For stress triggering areas that showed a correlation with seismicity rate changes, we estimated the optimal ratio of the stressing rate during the SSE period to the background stressing rate using the modified rate/state stress transfer model (Dieterich, 1994; Segall et al., 2006).

3.5.1 Correlation between Increasing Stressing Rate Change due to SSEs and Observed Seismicity Rate Increase

3.5.1.1 Correlation Study on Receiver faults based on Optimally Oriented Fault Planes

We resolved CSRC on the OOPs (optimally oriented fault planes) in three different depth ranges (0-30 km, 30 – 60 km and 60 – 90 km) for each SSE (Figure 3.3), because the spatial pattern of the CSRC varied with depth. OOPs located within the crust (0 – 30 km) and the intermediate slab depth (60 – 90 km) were mainly strike-slip type faults, while those within the shallow slab depth (30 – 60 km) were mostly thrust fault type planes. SSE1 and SSE2 showed similar patterns for all depth ranges, which was expected given that the region of slip was very similar in SSE1 and SSE2. Overlap between the source fault and receiver fault caused the sawtooth-like artifacts in the shallow slab depth range.

We used all earthquakes above the corresponding magnitude completeness (Mc) (Table 3.1) within each potential triggering area to calculate the seismicity rate change through time. We conclude that SSEs triggered earthquakes within a depth range only if all three areas (all three thresholds) within this depth range show a good correlation between increasing Coulomb stressing rate and increasing seismicity rates. If there is a correlation for only some of the thresholds, then the evidence for triggering is weaker.

We found a good correlation between increasing Coulomb stressing rate and increasing seismicity rate within the areas in the shallow slab depth range (30 – 60 km) for both events (Figures 3.4 and 3.5). Within this depth range, there were more earthquakes during the SSEs. Both

SSEs promoted failure within shallow slab depths in areas that experienced a seismicity rate increase during the SSEs period and then a decrease after SSEs ended (Figures 3.4 and 3.5). But there was no clear correlation between seismicity rate and CSRC within the crust (0 – 30 km) and the intermediate slab depth (60 – 90 km).

3.5.1.2 Correlation Study on Receiver Faults based on Geometry of Nodal Planes of the Focal Mechanism Solutions

We resolved the CSRCs due to the two SSEs on faults defined by the nodal planes of the focal mechanism solutions for the past earthquakes in the study region. The focal mechanism solutions provided two potential nodal planes for each past earthquake and we were not sure which nodal plane was the real fault plane. The calculated CSRCs for the two nodal planes differed because the unclamping stresses were not the same, so we repeated the computation of CSRC on both nodal planes and selected the larger value as the CSRC in the correlation study. We considered receiver faults with this geometry throughout each potential stress triggering area in order to test their correlation with the corresponding seismicity rate change. We used all the recorded earthquakes above the Mc (Table 3.2) for each area to get a reliable estimate of the seismicity rate change through time.

As with the correlation study based on OOPs, there was no clear pattern found between CSRC and seismicity rate changes in potential triggering areas within the crust (0 – 30 km) and the intermediate slab (60 – 90 km) when using the fault geometry defined by the nodal planes for the receiver faults. The areas within the shallow slab depths (30 – 60 km) that experienced significant increase in Coulomb stressing rate due to SSE1 showed an increase in seismicity rate during SSE1. After the end of SSE1, the seismicity rate decreased again (Figure 3.6). For SSE2, no receiver faults experienced CSRC as high as 0.025 MPa/year or 0.05 MPa/year. Within the stress triggering area selected based on the 0.005 MPa/year threshold, the seismicity rate increased right after SSE2 started and the seismicity rate decreased once SSE2 ended (Figure 3.7).

3.5.2 Rate/State Stress Transfer Model Results

We used the modified rate/state stress model (Equations 3.2 – 3.8 modified from Segall et al. (2006) to calculate the predicted seismicity rate change through time in the stress triggering areas selected in section 3.5.1 and compared this to the observed cumulative number of earthquakes. As shown in section 3.5.1, the potential stress triggering areas due to SSE1 and SSE2 appeared to be different, so the ratios of the stressing rate and seismicity rate between the post-

SSE1 period (or pre-SSE2 period) and the background period were different when exploring the triggering effects due to two SSEs individually in the modified rate/state stress transfer model.

3.5.2.1 Rate/State Model in Stress Triggering Zones based on Optimally Oriented Fault Planes

In section 3.5.1.1, we found a good correlation between the CSRC and increasing seismicity rate in the stress triggering areas designed based on OOPs for the shallow slab seismicity, 30 – 60 km depth. We adjusted the stressing rate ratios to fit the calculated cumulative number of earthquakes to the observed seismicity rates. The best fit for the SSE1 period was an increase in stressing rate above the background stressing rate by a factor of 1.192, 1.102, and 1.28, corresponding to the different areas selected based on the thresholds 0.001, 0.005 and 0.01 MPa/year, respectively (Figures 3.4 and 3.8). The optimal ratios of the stressing rate during the post-SSE1 period to the background stressing rates were 1.089, 1.02 and 1.25 for these three triggering areas (Figures 3.4 and 3.8). This suggests there was a 10-20% increase in stressing rate during SSE1 followed by a return to close to the long-term steady stressing rate.

The estimated best ratios of the stressing rates during the SSE2 period to the background stressing rates were 1.48, 1.25 and 1.16 within the areas selected based on the thresholds 0.005, 0.025, 0.05 MPa/year, respectively. The model also showed that the optimal ratios of the stressing rate during the pre-SSE2 period to the background stressing rates were 1.3, 1.2 and 1.13 (Figure 3.9). These ratios indicated that the stressing rate and the seismicity rate both increased during the SSE2 period compared with those during the pre-SSE2 period and decreased after SSE2 ends.

3.5.2.2 Rate/State Model in Stress Triggering Zones based on Geometry of Nodal Planes of the Focal Mechanism Solutions

We repeated the analysis for the stress triggering areas (30 – 60 km) selected based on the geometry of the nodal planes of focal mechanism solutions. The stress triggering areas selected based on thresholds 0.005 and 0.01 MPa/year due to SSE1 were essentially the same areas in this case. The best fit, obtained for ratios of the stressing rates during the SSE1 period to the background stressing rate were 1.0842, 1.237 and 1.237 within the areas selected based on the thresholds 0.001, 0.005 and 0.01 MPa/year, respectively (Figure 3.10). The optimal ratios of the stressing rates during the post-SSE1 period to the background stressing rate were 1.048, 1.213 and 1.213 within the three areas. These are nearly identical to the results obtained using optimally oriented fault planes, which indicates that this result is not sensitive to the exact choice of receiver fault geometry, or to the triggering thresholds.

Since no areas exceeded the thresholds of 0.025 MPa/year or 0.05 MPa/year, the best ratio of the stressing rate during the SSE2 period to the background stressing rate was only estimated for the area based on threshold 0.005 MPa/year, with a result of 1.44. Meanwhile, the optimal ratio of the stressing rate during pre-SSE2 period and the background stressing rate was 1.37 (Figure 3.11). These ratios are also similar to the results calculated based on OOPs.

3.6 Discussion

3.6.1 Significance of Seismicity Rate Changes and Stressing Rate Changes due to SSEs

In order to evaluate the significance of seismicity rate changes due to SSEs, we used the z-value statistic(Habermann, 1983) implemented in ZMAP. The value of z represents the number of standard deviations away from the mean and has the same interpretation in terms of significance. A positive z-value indicates a decreasing seismicity rate while a negative value indicates an increasing seismicity rate. We calculated the z-value between the non-SSE period and the SSE period and saw how significant the seismicity rate changes due to SSEs were (Tables 3.3 and 3.4).

Based on the estimated z-values and their significance levels, the seismicity rate changes due to the two SSEs are significant in most of the selected stress triggering areas. Significance level for the seismicity rate change during SSE2 period compared with the seismicity rate in the post-SSE2 period (99%) or the pre-SSE2 (60%) has been identified within areas selected through receiver faults defined by nodal planes (Table 3.3). The significance level for the seismicity rate change during SSE1 compared with the seismicity rate in the post-SSE1 period within the area selected based on the 0.001 MPa/year threshold is 70%. The results within the triggering areas selected through OOP receiver faults indicate 99% and 96% significance levels for the seismicity rate change during SSE1 period compared with the seismicity rate in the post-SSE1 period within the areas selected based on 0.001 and 0.005 MPa/year thresholds. Significance levels for the seismicity rate change during SSE2 period are 89%, 99% compared with the pre-SSE2 and post-SSE2 periods within areas selected through OOP based on 0.005 MPa/year, 93% compared with the post-SSE2 period within area selected based on 0.025 MPa/year, and 74% compared with the post-SSE2 period within area selected based on 0.05 MPa/year. Mostly significance levels are larger than 50% (Table 3.4). In general, the calculated z-values and their significances within the stress triggering areas affected by two SSEs for two different receiver faults are very similar.

In our study, the potential triggering areas due to each SSE were explored individually. The quantitative models indicate that the background stressing rates and seismicity rates differ by

region. The percentage changes in stressing rate presented earlier cannot be compared directly because they refer to different areas, with different average background stressing rates. In order to compare directly the ratios for the two SSEs, we picked an area affected by both SSEs based on the stress triggering areas in section 3.5.1 (Figure 3.12a). We used all the earthquakes above Mc 1.78 within the area from 1996 to November in 2014 to calculate the seismicity rate change through time (Figure 3.12b). This area experienced an increase in seismicity rate during SSE1, the seismicity rate decreased to a value close to but still slightly larger than the background, then it increased again during SSE2 period and decreased back to the background. We also calculated the z-value and its significance in this area (Figure 3.12c). We used the same modified rate/state stress transfer model to adjust the stressing rate ratios to fit the calculated cumulative number of earthquakes to the observed seismicity rates. There was a 29% increase in stressing rate during the SSE1 period, a 9% increase during the post-SSE1 period and 18% increase during the SSE2 period comparing with the background which was assumed to be the same as the one in the post-SSE2 period (Figure 3.12d).

3.6.2 Limitations in investigating the relationship between SSEs and Regular Earthquakes

SSE1 lasted at least 9 years, as it was already underway when our GPS observations in that area begin in 1995, so we have no information about the slip distribution before SSE1. We also cannot test whether the seismicity rate changed at the start of SSE1 because the seismic network and analysis techniques changed dramatically in the early 1990s. The Mc for the early 1990s was about 2.3 and as a result too few earthquakes were left if we applied this Mc to the whole dataset. The lack of GPS displacement before 1995 and the seismic catalogue changes limit our understanding about the stressing rate and seismicity rate before SSE1. We could only explore the stressing rate change and seismicity rate change from the SSE1 period to the post-SSE1 period.

3.6.3 Triggering Effects on Seismogenic zone from the observed long-term SSEs in Alaska

The seismogenic zone is defined as the part of the plate interface that could slip coseismically during large earthquakes, based on present-day locking, uplift/subsidence history, and /or megathrust temperatures (Li et al., 2015). The two SSEs on the subduction plate interface were both located near the downdip end of the seismogenic zone based on the 1964 slip distribution (Suito & Freymueller, 2009). It has been proposed that slow slip could bring the seismogenic zone closer to failure and possibly trigger a large megathrust earthquake (Dixon et al., 2014) .

We calculated the Coulomb stress changes due to all four long-term SSEs in Alaska (both Upper and Lower Cook Inlet) on the seismogenic zone and added them together (Figure 3.13). Figure 3.13 showed that cumulative stress effects from the two long-term SSEs in each area caused significant positive Coulomb stress changes in the seismogenic zone on the megathrust up to 30–50 km up-dip of the SSE areas. Figure 3.13b presents the Coulomb stress change along two selected profile lines on the seismogenic zone due to SSEs in the Upper and Lower Cook Inlet. Gradually increasing Coulomb stress changes are predicted starting from the trench toward the downdip end of the seismogenic zone. SSEs in each area (Lower or Upper Cook Inlet) bring the megathrust updip of it closer to failure by 0.2 – 0.3MPa. It is also clear from Figure 3.13a that the stress triggering areas for SSEs in the Lower and Upper Cook Inlet do not overlap, as there is a clear region of low stress change between them.

3.7 Conclusion

In this study, we found a significant correlation between increasing stressing rates due to SSE slip and increases in seismicity rate during the SSEs within shallow slab depths (30 – 60 km). No similar correlation was found for areas in the crust (0 – 30 km) and at intermediate slab depths (60 – 90 km), even though some places in these depth ranges experienced significant increases in stressing rate during the SSEs. The z-value analysis suggests significant seismicity rate changes due to SSEs in most of the selected stress triggering areas. Applying the quantitative rate/state model suggests that there was a 10 – 28% increase in stressing rate during SSE1, and a 0.2% - 25% higher stressing rate during the post-SSE1 period compared with the background rate in the selected triggering areas affected by SSE1 only. The modeled results also show that there was a 16% - 48% increase in stressing rate during the SSE2 period compared with the background and then a decrease back to the background after the SSE2 ended. The inferred stressing rates before SSE2 were 13% - 30% higher than the background. We conclude that slip in the long-term SSEs stressed the adjacent faults, therefore increasing the seismicity rate even though the optimal fit for the ratio of the SSEs to the background stressing rate is small. Different ratios of the stressing rate between the post-SSE1 period (and the pre-SSE2 period) and the background in the areas affected by the two SSEs indicated a possible spatial variation in the background stressing rate or time variations in the slip pattern. The results from the modified rate/state model show that the exact choice of receiver fault geometry does not affect the calculated ratio of the stressing rates between SSE periods and the background period. We also confirm that the four detected long-term SSEs in

Cook Inlet promoted significant stress failure up-dip of the SSE areas in the seismogenic zone. Each long-term SSE in Cook Inlet brought the megathrust updip of the SSE region closer to failure, by up to 0.1 - 0.15 MPa. The SSEs in Upper Cook Inlet do not have triggering effects in the areas where significantly affected by the SSEs in Lower Cook Inlet and vice versa.

3.8 Acknowledgements

We acknowledge EarthScope for the Plate Boundary Observatory (PBO) data, UNAVCO for operations of the PBO and Alaska Earthquake Center for management of regional seismic network in Alaska. This research was supported by NSF award EAR-1215933 to the University of Alaska Fairbanks. The campaign GPS data that augmented the PBO data were collected mainly under NSF awards EAR-0106824, EAR-9980496, EAR-9805326, EAR-0106829, and EAR-0409950. We used the Generic Mapping Tools (GMT) (Wessel et al., 2013) to draw the figures.

3.9 Reference

Arai, R., Takahashi, T., Kodaira, S., Kaiho, Y., Nakanishi, A., Fujie, G., et al. (2016). Structure of the tsunamigenic plate boundary and low-frequency earthquakes in the southern Ryukyu Trench. *Nature Communications*, *7*, 12255.

Dieterich, J. (1994). A constitutive law for rate of earthquake production and its application to earthquake clustering. *Journal of Geophysical Research: Solid Earth*, *99*(B2), 2601–2618.

Dixon, T. H., Jiang, Y., Malservisi, R., McCaffrey, R., Voss, N., Protti, M., & Gonzalez, V. (2014). Earthquake and tsunami forecasts: Relation of slow slip events to subsequent earthquake rupture. *Proceedings of the National Academy of Sciences*, *111*(48), 17039–17044.

Dragert, H., Wang, K., & James, T. S. (2001). A silent slip event on the deeper Cascadia subduction interface. *Science*, *292*(5521), 1525–1528.

Fu, Y., & Freymueller, J. T. (2013). Repeated large Slow Slip Events at the southcentral Alaska subduction zone. *Earth and Planetary Science Letters*, *375*, 303–311.

Fu, Y., Liu, Z., & Freymueller, J. T. (2015). Spatiotemporal variations of the slow slip event between 2008 and 2013 in the southcentral Alaska subduction zone. *Geochemistry, Geophysics, Geosystems*, *16*(7), 2450–2461.

Furumoto, A. S. (1965). *Analysis of Rayleigh wave, Part II in source mechanism study of the Alaska earthquake and tsunami of March 27, 1964*. Report HIG-65-17, Honolulu: University of Hawaii, Institute of Geophysics, December, 31-42.

Habermann, R. E. (1983). Teleseismic detection in the Aleutian Island arc. *Journal of Geophysical Research: Solid Earth*, *88*(B6), 5056–5064.

Hirose, H., Asano, Y., Obara, K., Kimura, T., Matsuzawa, T., Tanaka, S., & Maeda, T. (2010). Slow earthquakes linked along dip in the Nankai subduction zone. *Science*, *330*(6010), 1502–1502.

Ide, S. (2012). Variety and spatial heterogeneity of tectonic tremor worldwide. *Journal of Geophysical Research: Solid Earth*, *117*(B3).

Ishibe, T., Satake, K., Sakai, S., Shimazaki, K., Tsuruoka, H., Yokota, Y., et al. (2015). Correlation between Coulomb stress imparted by the 2011 Tohoku-Oki earthquake and seismicity rate change in Kanto, Japan. *Geophysical Journal International*, *201*(1), 112–134.

Ito, Y., Hino, R., Kido, M., Fujimoto, H., Osada, Y., Inazu, D., et al. (2013). Episodic slow slip events in the Japan subduction zone before the 2011 Tohoku-Oki earthquake. *Tectonophysics*, *600*, 14–26.

Kim, M. J., Schwartz, S. Y., & Bannister, S. (2011). Non-volcanic tremor associated with the March 2010 Gisborne slow slip event at the Hikurangi subduction margin, New Zealand. *Geophysical Research Letters*, *38*(14).

King, G. C., Stein, R. S., & Lin, J. (1994). Static stress changes and the triggering of earthquakes. *Bulletin of the Seismological Society of America*, *84*(3), 935–953.

Kostoglodov, V., Singh, S. K., Santiago, J. A., Franco, S. I., Larson, K. M., Lowry, A. R., & Bilham, R. (2003). A large silent earthquake in the Guerrero seismic gap, Mexico. *Geophysical Research Letters*, *30*(15).

Li, J., Shillington, D. J., Bécel, A., Nedimović, M. R., Webb, S. C., Saffer, D. M., et al. (2015). Downdip variations in seismic reflection character: Implications for fault structure and seismogenic behavior in the Alaska subduction zone. *Journal of Geophysical Research: Solid Earth*, *120*(11), 7883–7904.

Li, S., Freymueller, J., & McCaffrey, R. (2016). Slow slip events and time-dependent variations in locking beneath Lower Cook Inlet of the Alaska-Aleutian subduction zone. *Journal of Geophysical Research: Solid Earth*, *121*(2), 1060–1079.

Nadeau, R. M., & Dolenc, D. (2005). Nonvolcanic tremors deep beneath the San Andreas Fault. *Science*, *307*(5708), 389–389.

Ochi, T., & Kato, T. (2013). Depth extent of the long-term slow slip event in the Tokai district, central Japan: A new insight. *Journal of Geophysical Research: Solid Earth*, *118*(9), 4847–4860.

Ohta, Y., Freymueller, J. T., Hreinsdóttir, S., & Suito, H. (2006). A large slow slip event and the depth of the seismogenic zone in the south central Alaska subduction zone. *Earth and Planetary Science Letters*, *247*(1), 108–116.

Okada, Y. (1992). Internal deformation due to shear and tensile faults in a half-space. *Bulletin of the Seismological Society of America*, *82*(2), 1018–1040.

Payero, J. S., Kostoglodov, V., Shapiro, N., Mikumo, T., Iglesias, A., Pérez-Campos, X., & Clayton, R. W. (2008). Nonvolcanic tremor observed in the Mexican subduction zone. *Geophysical Research Letters*, *35*(7).

Peterson, C. L., & Christensen, D. H. (2009). Possible relationship between nonvolcanic tremor and the 1998–2001 slow slip event, south central Alaska. *Journal of Geophysical Research: Solid Earth*, *114*(B6).

Rogers, G., & Dragert, H. (2003). Episodic tremor and slip on the Cascadia subduction zone: The chatter of silent slip. *Science*, *300*(5627), 1942–1943.

Ruppert, N. A. (2008). Stress map for Alaska from earthquake focal mechanisms. *Active Tectonics and Seismic Potential of Alaska*, 351–367.

Ruppert, N. A., & Hansen, R. A. (2010). Temporal and spatial variations of local magnitudes in Alaska and Aleutians and comparison with body-wave and moment magnitudes. *Bulletin of the Seismological Society of America*, *100*(3), 1174–1183.

Schwartz, S. Y., & Rokosky, J. M. (2007). Slow slip events and seismic tremor at circum-Pacific subduction zones. *Reviews of Geophysics*, *45*(3).

Segall, P., Desmarais, E. K., Shelly, D., Miklius, A., & Cervelli, P. (2006). Earthquakes triggered by silent slip events on Kīlauea volcano, Hawaii. *Nature*, *442*(7098), 71.

Suito, H., & Freymueller, J. T. (2009). A viscoelastic and afterslip postseismic deformation model for the 1964 Alaska earthquake. *Journal of Geophysical Research: Solid Earth (1978–2012)*, *114*(B11).

Szeliga, W., Melbourne, T. I., Miller, M. M., & Santillan, V. M. (2004). Southern Cascadia episodic slow earthquakes. *Geophysical Research Letters*, *31*(16).

Wallace, L. M., & Beavan, J. (2010). Diverse slow slip behavior at the Hikurangi subduction margin, New Zealand. *Journal of Geophysical Research: Solid Earth (1978–2012)*, *115*(B12).

Walter, J. I., Schwartz, S. Y., Protti, J. M., & Gonzalez, V. (2011). Persistent tremor within the northern Costa Rica seismogenic zone. *Geophysical Research Letters*, *38*(1).

Wang, J., Xu, C., Freymueller, J. T., Li, Z., & Shen, W. (2014). Sensitivity of Coulomb stress change to the parameters of the Coulomb failure model: A case study using the 2008 Mw 7.9 Wenchuan earthquake. *Journal of Geophysical Research: Solid Earth*, *119*(4), 3371–3392.

Wech, A. G. (2016). Extending Alaska's plate boundary: Tectonic tremor generated by Yakutat subduction. *Geology*, *44*(7), 587–590.

Wessel, P., Smith, W. H., Scharroo, R., Luis, J., & Wobbe, F. (2013). Generic mapping tools: improved version released. *Eos, Transactions American Geophysical Union*, *94*(45), 409–410.

Wiemer, S. (2001). A software package to analyze seismicity: ZMAP. *Seismological Research Letters*, *72*(3), 373–382.

Xu, C., Wang, J., Li, Z., & Drummond, J. (2010). Applying the Coulomb failure function with an optimally oriented plane to the 2008 Mw 7.9 Wenchuan earthquake triggering. *Tectonophysics*, *491*(1–4), 119–126.

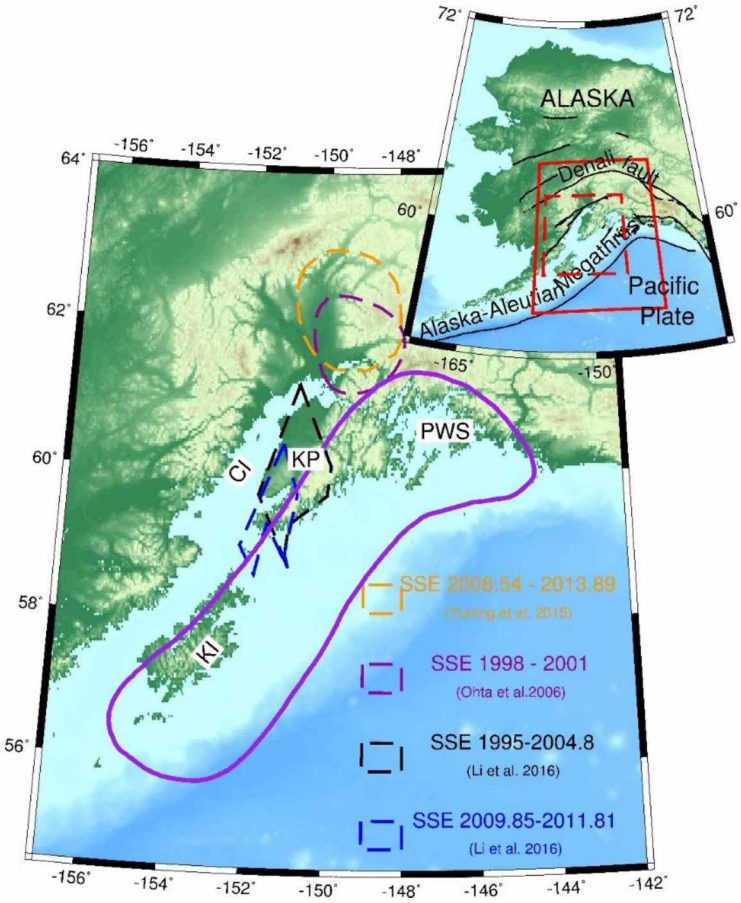

Figure 3.1 Tectonic setting (inset) and study area in south central Alaska (red solid rectangle in inset map). Red dashed rectangle is the study area for exploring the stress triggering areas due to two SSEs. Purple outline shows the approximate rupture extent of the 1964 earthquake (Furumoto, 1965). Purple dashed outline shows the 1998-2001 slow slip event (Ohta et al., 2006); orange dashed outline shows the 2009-2013 slow slip event (Fu & Freymueller, 2013); black dashed outline shows the 1995-2004.8 slow slip event (Li et al., 2016); and blue dashed outline shows the 2009.85-2011.81 slow slip event (Li et al., 2016). CI: Cook Inlet; KP: Kenai Peninsula; PWS: Prince William Sound; and KI: Kodiak Island.

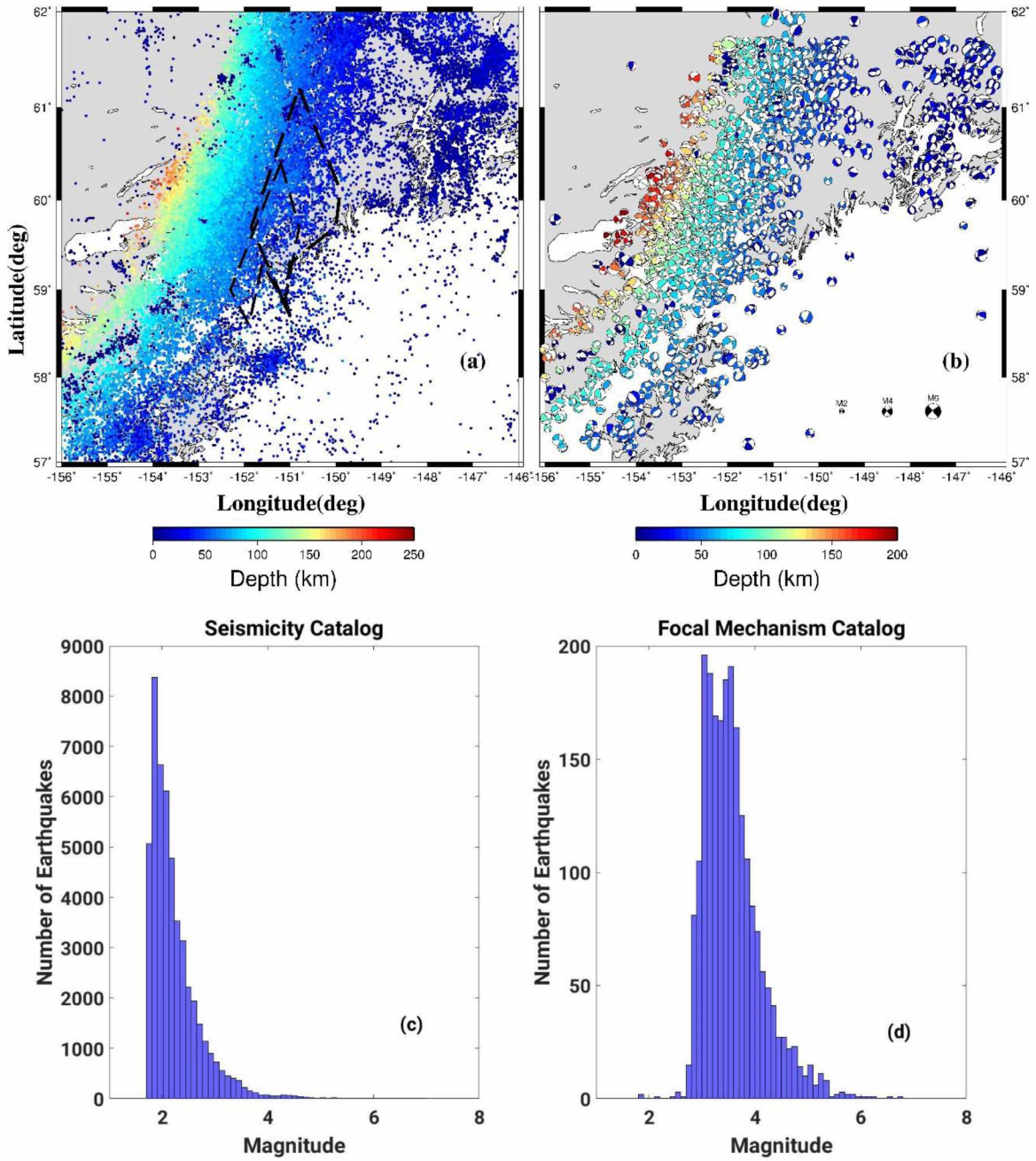

Figure 3.2 Spatial distribution of recorded earthquakes and focal mechanism solutions of the past earthquakes from the AEC catalog. (a) All earthquakes in the study region from the AEC catalog (Magnitude > 1.74); (b) Focal mechanism solutions from the AEC catalog that will be used for one definition of the receiver faults; (c) Magnitude histogram for the seismicity catalog in (a); (d) Magnitude histogram for the focal mechanism catalog in (b).

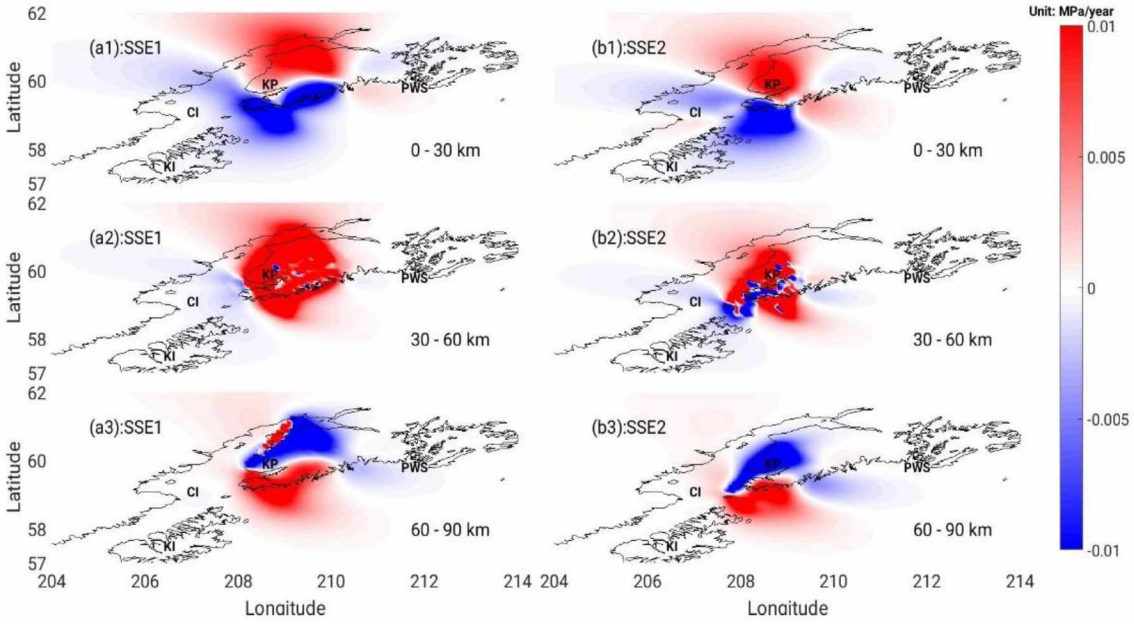

Figure 3.3 Changes in Coulomb stressing rate on OOPs due to SSE1 (a1 – a3) and SSE2 (b1 – b3) within three different depth ranges (0 – 30 km, 30 – 60 km, 60 – 90 km). CI: Cook Inlet, KP: Kenai Peninsula, PWS: Prince William Sound, KI: Kodiak Island.

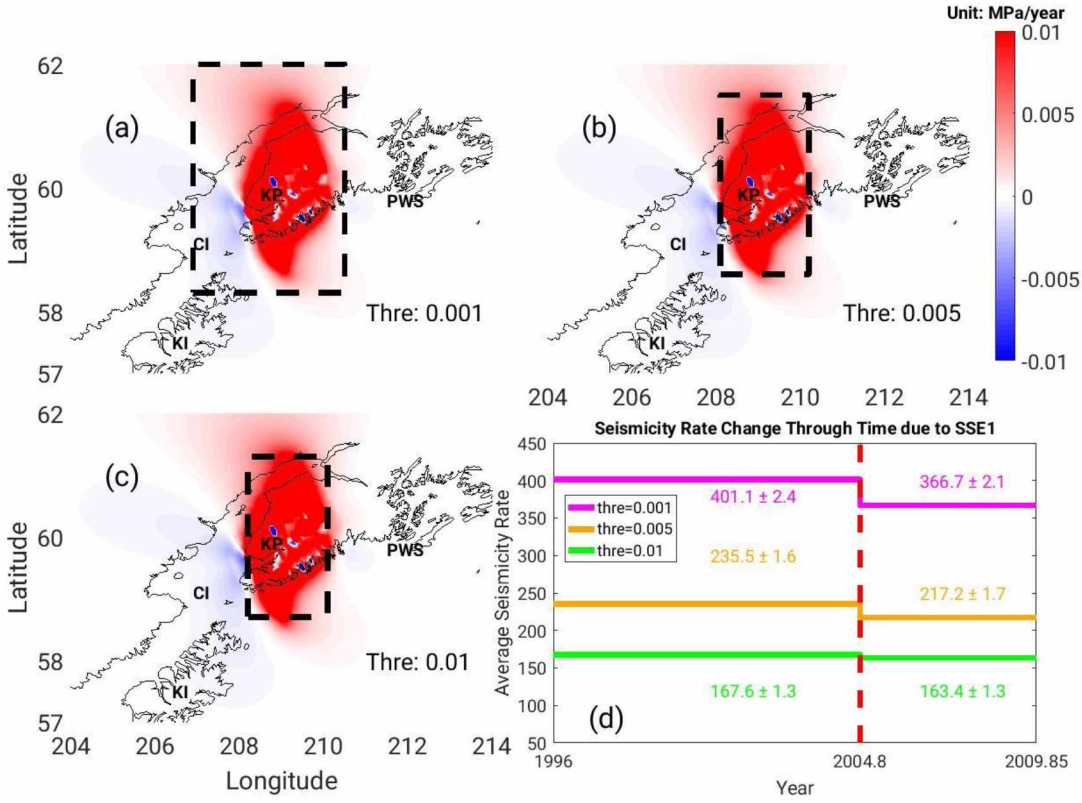

Figure 3.4 Correlation between CSRC on OOPs and seismicity rate change due to the SSE1 in areas selected by three thresholds (a-c) within 30 – 60 km depth range. The numbers in (d) represent the calculated seismicity rate for each time window (SSE1 period and post-SSE1 period). Different colors indicate different seismicity rates in areas selected by different thresholds. CI: Cook Inlet, KP: Kenai Peninsula, PWS: Prince William Sound, KI: Kodiak Island.

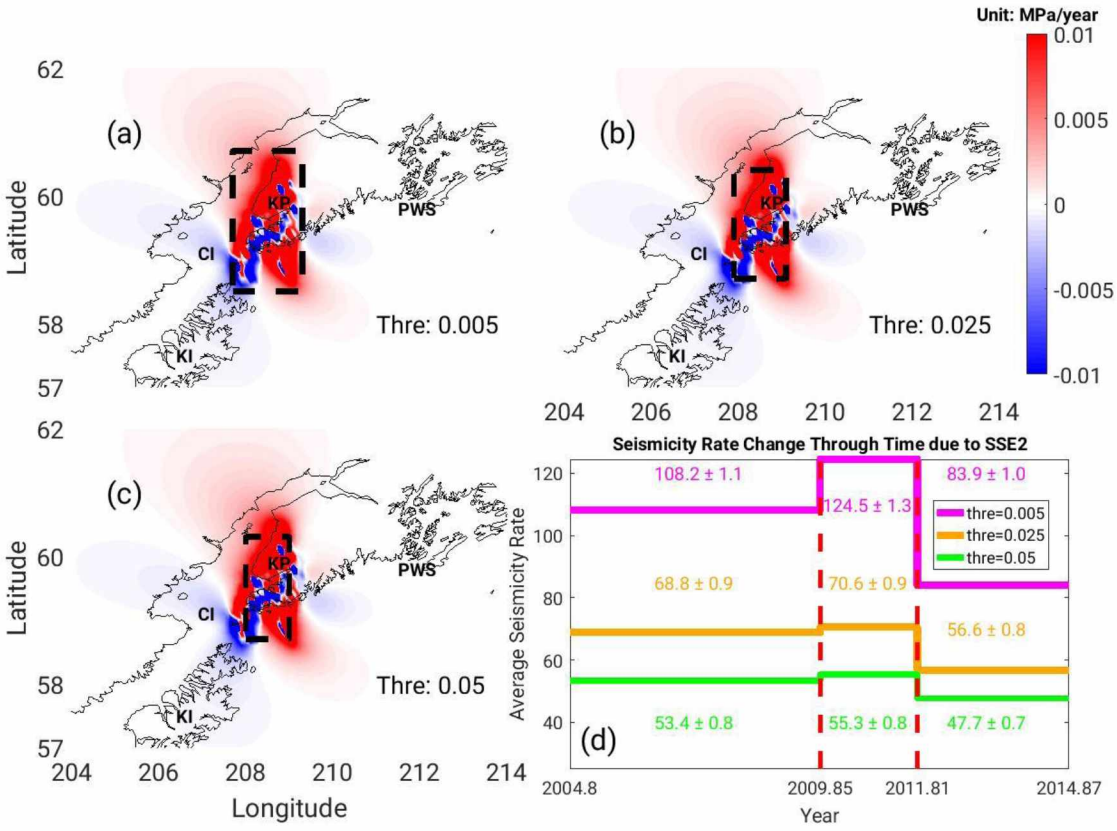

Figure 3.5 Correlation between CSRC on OOPs and in seismicity rate change due to the SSE2 in areas selected by three thresholds (a-c) within 30 – 60 km depth range. The numbers in (d) represent the calculated seismicity rate for three time windows (pre-SSE2, SSE2 and post-SSE2 periods). Different colors indicate different seismicity rates in areas selected by different thresholds. CI: Cook Inlet, KP: Kenai Peninsula, PWS: Prince William Sound, KI: Kodiak Island.

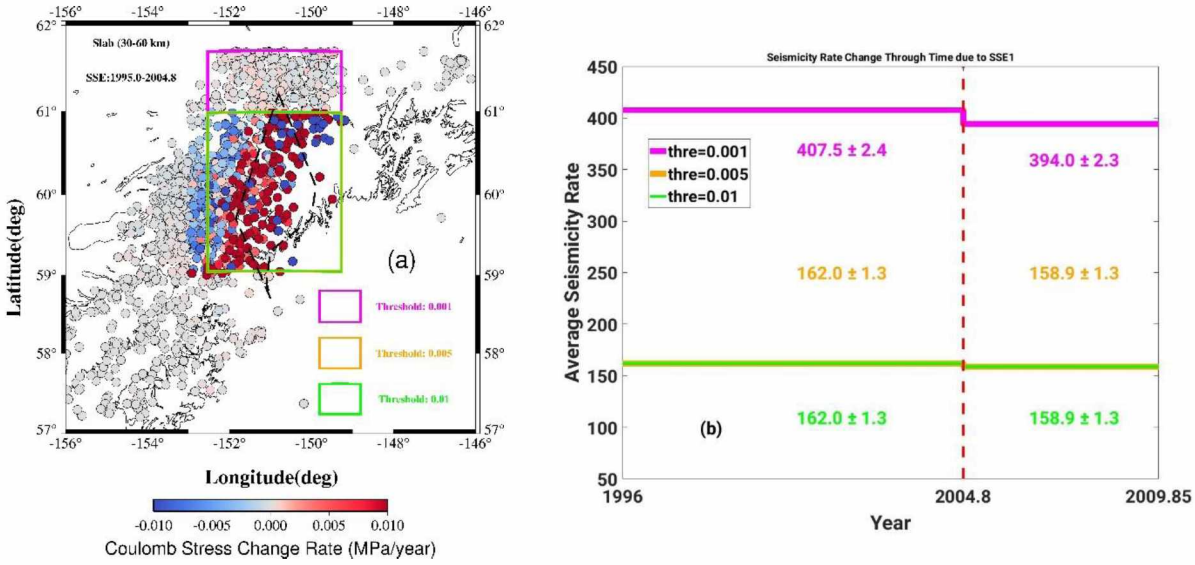

Figure 3.6 Correlation between CSRC resolved on receiver faults based on observed nodal plane geometry (a) and seismicity rate change (b) in stress triggering areas within the 30 – 60 km depth range due to SSE1.

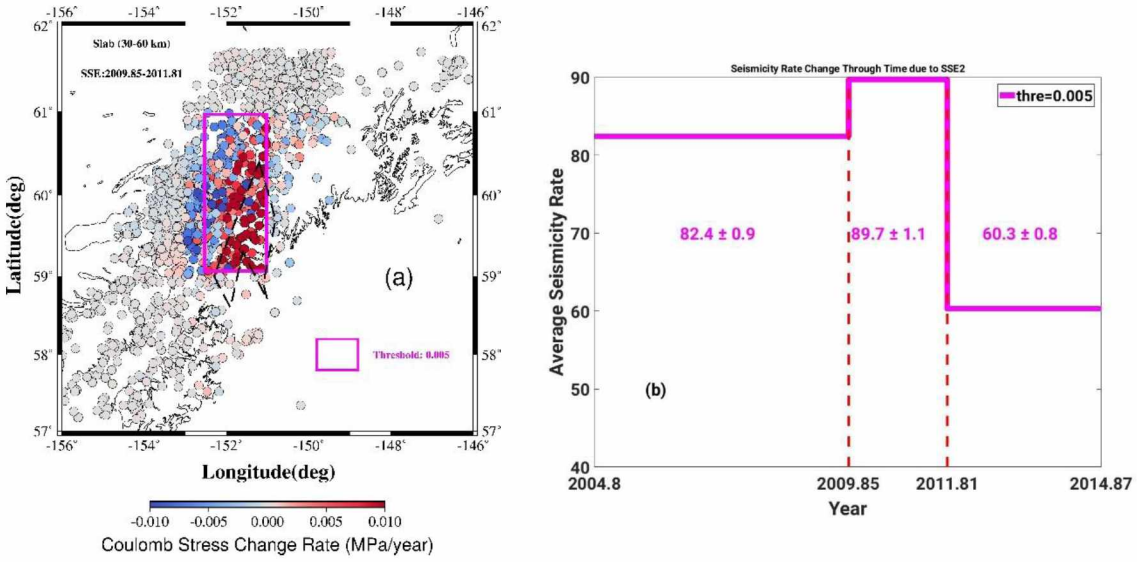

Figure 3.7 Correlation between CSRC resolved on receiver faults based on observed nodal plane geometry (a) and seismicity rate change (b) in stress triggering areas within 30 – 60 km depth range due to SSE2.

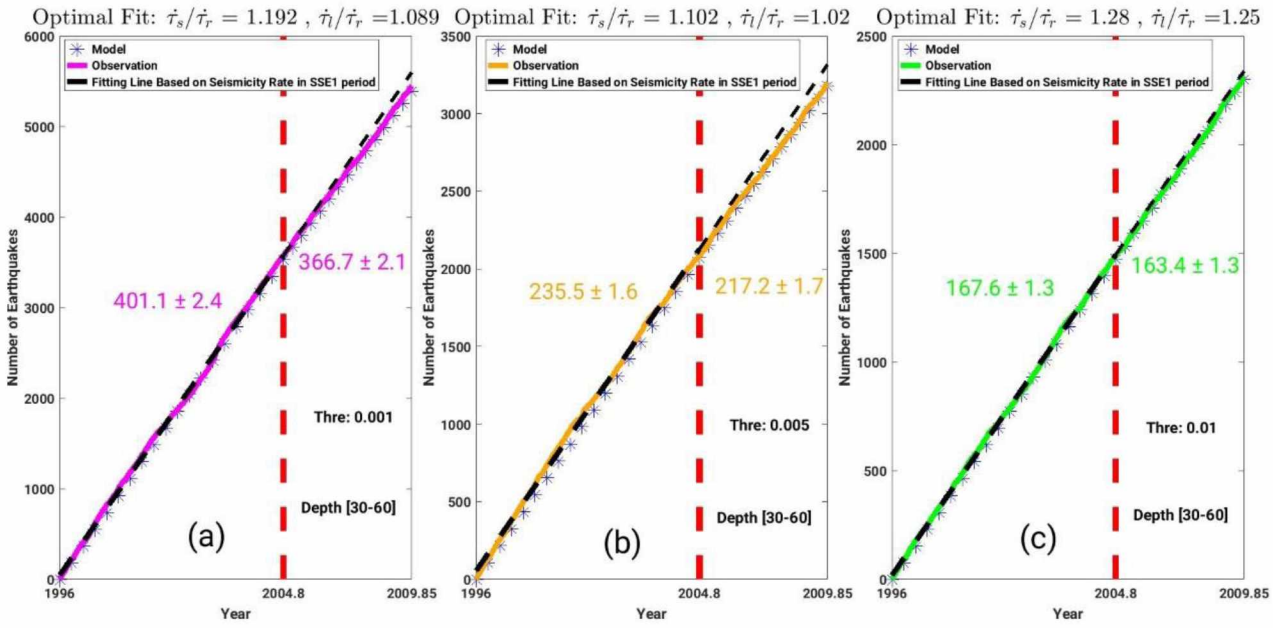

Figure 3.8 The rate/state stress transfer model results in the different stress triggering areas affected by SSE1 on OOPs (a-c correspond to three areas in Figure 3.4a – 3.4c). $\frac{\dot{\tau}_s}{\dot{\tau}_r}$ is the optimal ratio of the stressing rate during SSE1 period and the background stressing rate. $\frac{\dot{\tau}_l}{\dot{\tau}_r}$ is the optimal ratio of the stressing rate during post-SSE1 period and the background stressing rate. The red dashed line shows the end time of SSE1 (2004.8).

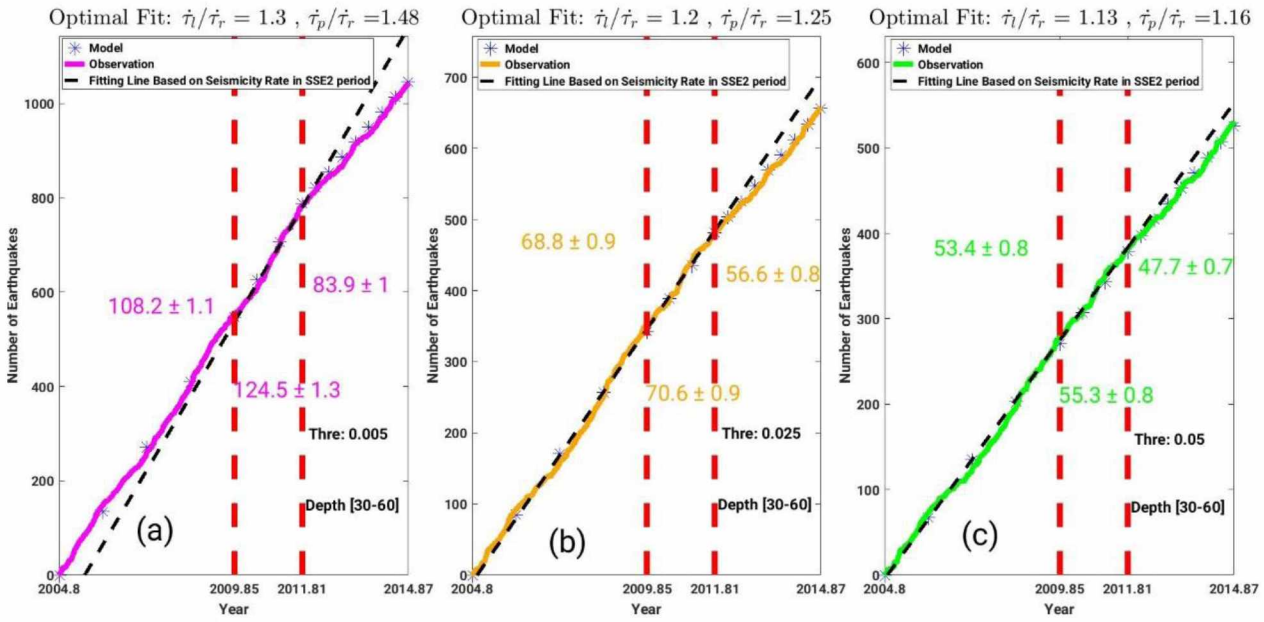

Figure 3.9 The rate/state stress transfer model results in the stress triggering zones affected by SSE2 on OOPs (a-c correspond to three areas in Figure 3.5a – 3.5c). $\frac{\dot{\tau}_l}{\dot{\tau}_r}$ is the optimal ratio of the stressing rate during Pre-SSE2 period to the background stressing rate. $\frac{\dot{\tau}_p}{\dot{\tau}_r}$ is the optimal ratio of the stressing rate during SSE2 period to the background stressing rate. The red dashed lines show the start time and end time of the SSE2.

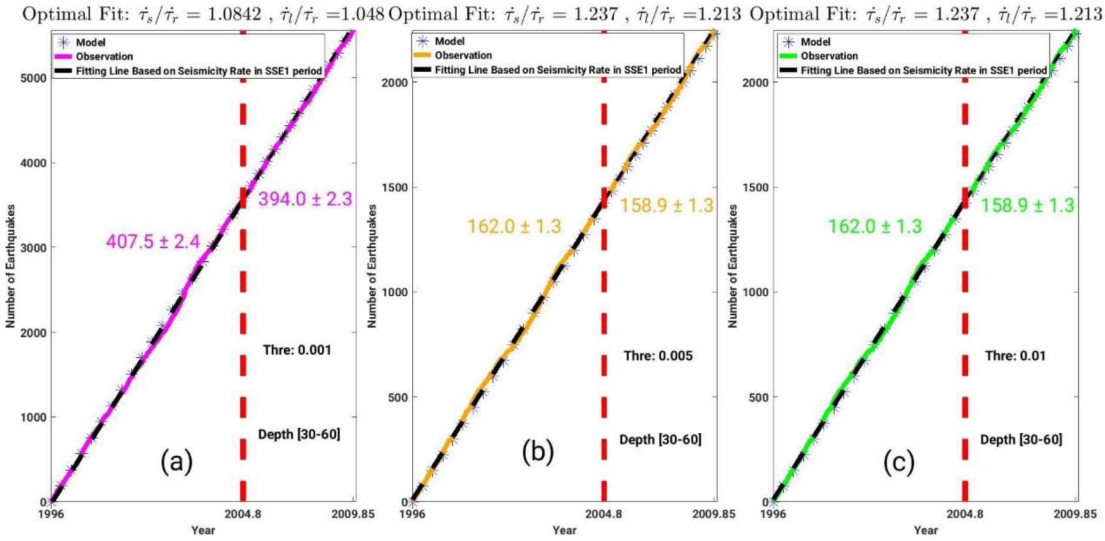

Figure 3.10 The rate/state stress transfer model results in the stress triggering zones affected by SSE1 on nodal planes (a-c). $\frac{\dot{\tau}_S}{\dot{\tau}_r}$ is the optimal ratio of the stressing rate during SSE1 period to the background stressing rate. $\frac{\dot{\tau}_l}{\dot{\tau}_r}$ is the optimal ratio of the stressing rate during Post-SSE1 period to the background stressing rate. The red dashed line show the end time of the SSE1.

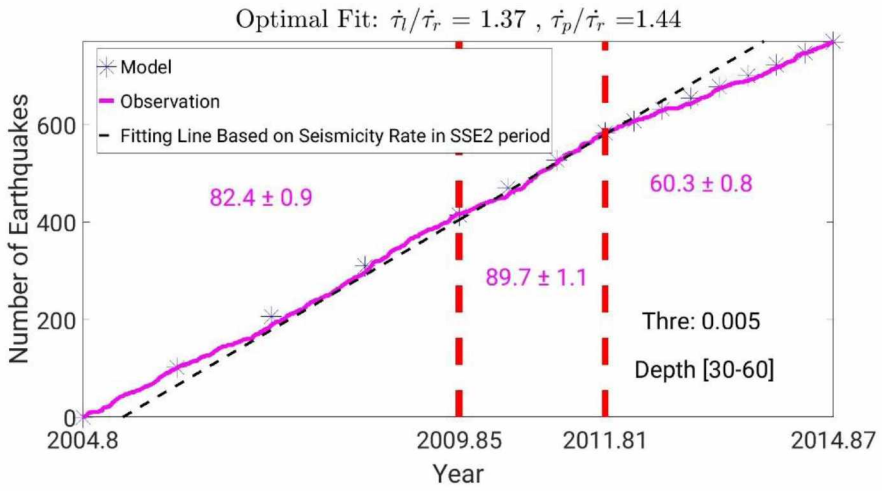

Figure 3.11 The rate/state stress transfer model results in the stress triggering zones affected by SSE2 on nodal planes. $\frac{\dot{\tau}_l}{\dot{\tau}_r}$ is the optimal ratio of the stressing rate during Pre-SSE2 period and the background stressing rate. $\frac{\dot{\tau}_p}{\dot{\tau}_r}$ is the optimal ratio of the stressing rate during SSE2 period and the background stressing rate. The red dashed lines mark the start time and end time of the SSE2.

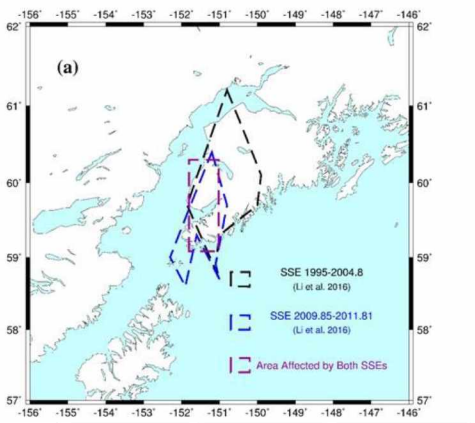

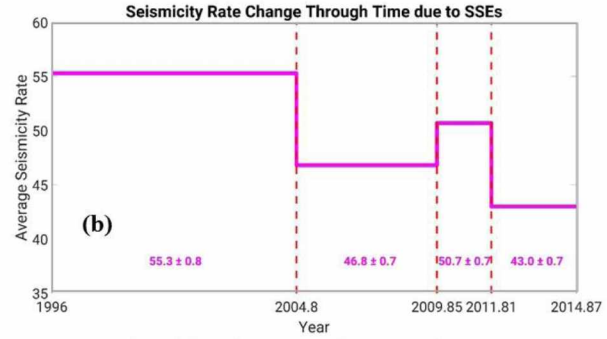

(c)

Periods Comparison	Z-value	Significance
p1 and p2	2.1798	97%
p2 and p3	-0.6617	49%
p3 and p4	1.2048	77%

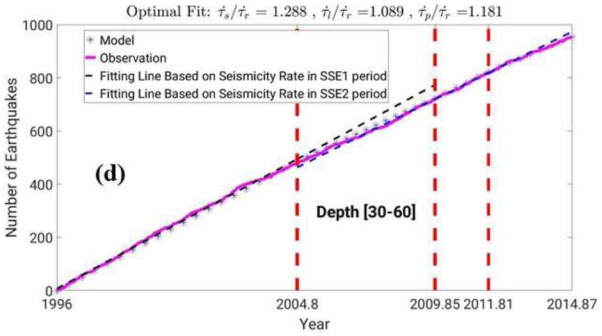

Figure 3.12 Correlation between Coulomb stressing rate change and seismicity rate change in an area affected by both SSEs based on the stress triggering areas in section 3.5.1. (a) The selected area affected by both SSEs. The numbers in (b) represent the calculated seismicity rate for each time window (SSE1 period, post-SSE1 period, SSE2 period and post-SSE2 period). (c) Z-value and its significance within the stress triggering areas affected by the two SSEs in area selected in (a). p1: SSE1 period, p2: post-SSE1 period or pre-SSE2 period, p3: SSE2 period and p4: post-SSE2 period. (d) The rate/state stress transfer model results in the area affected by two SSEs. $\frac{\dot{\tau}_s}{\dot{\tau}_r}$ is the optimal ratio of the stressing rate during SSE1 period and the background stressing rate. $\frac{\dot{\tau}_l}{\dot{\tau}_r}$ is the optimal ratio of the stressing rate during post-SSE1 period and the background stressing rate. $\frac{\dot{\tau}_p}{\dot{\tau}_r}$ is the optimal ratio of the stressing rate during SSE2 period and the background stressing rate.

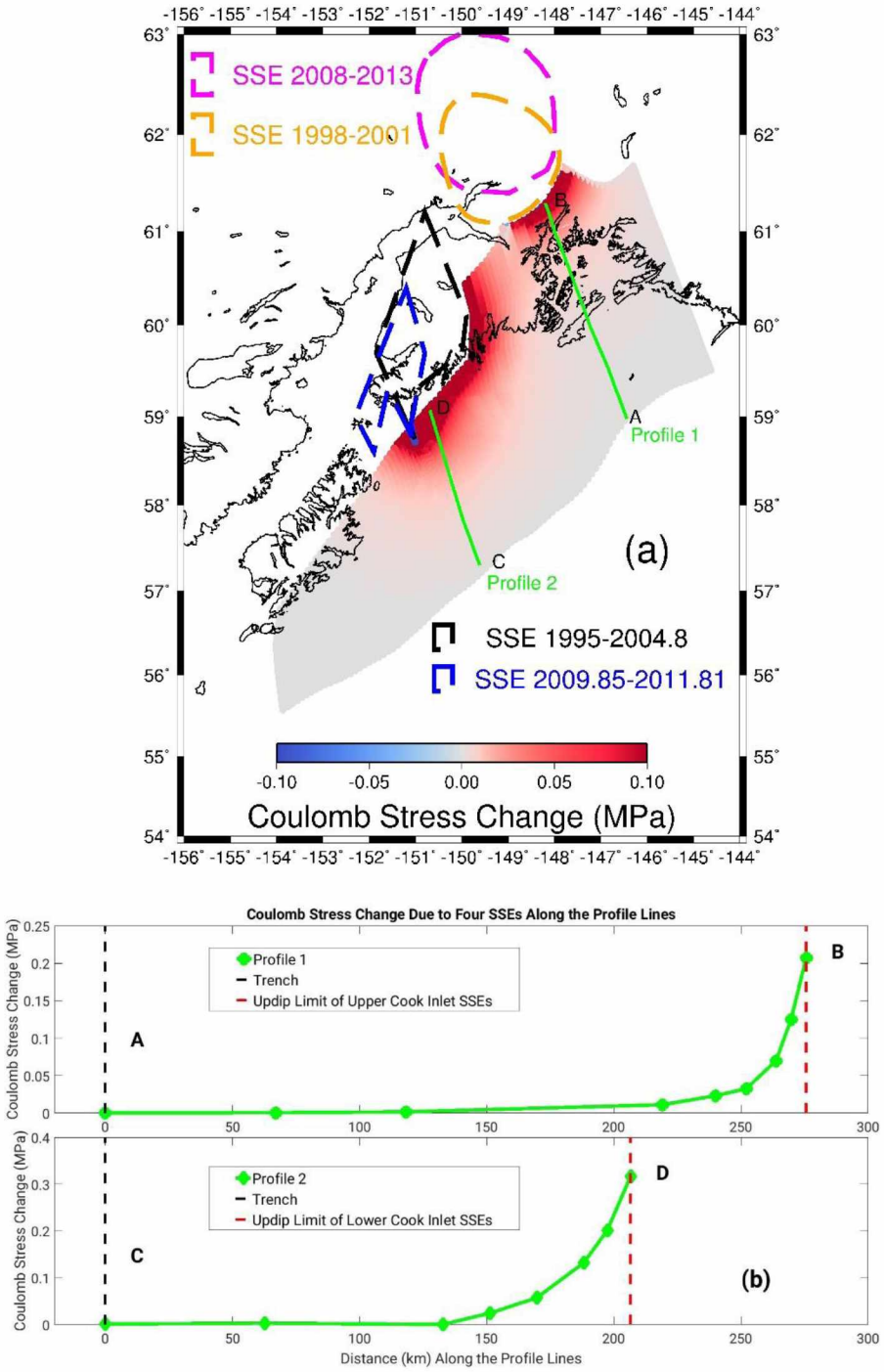

Figure 3.13 Resolved Coulomb stress change on seismogenic zone due to four detected long-term SSEs in Alaska-Aleutian Subduction Zone (a) and Coulomb Stress Change due to SSEs along Two Profile Lines (1 and 2 in (a)) (b). Black dashed lines in (b) indicate the location of trench on two profile lines. Red dashed lines in (b) mark the updip limit of Cook Inlet SSEs.

Table 3.1 CSRC thresholds and Magnitude of Completeness (Mc) used for different stress triggering areas based on three thresholds due to each event within 30 – 60 km on OOPs. The unit of the threshold is MPa/year.

Event	SSE1			SSE2		
Threshold	0.001	0.005	0.01	0.005	0.025	0.05
Mc	1.79	1.79	1.81	1.88	1.89	1.92

Table 3.2 CSRC thresholds and Magnitude of Completeness (Mc) used for the stress triggering areas selected based on three thresholds due to the two SSEs within 30 – 60 km on nodal planes. The unit of the threshold is MPa/year.

Event	SSE1			SSE2
Threshold	0.001	0.005	0.01	0.005
Mc	1.66	1.86	1.86	1.89

Table 3.3 Z-value and its significance within the stress triggering areas affected by the two SSEs for receiver faults defined by nodal planes. p1: SSE1 period, p2: post-SSE1 period or pre-SSE2 period, p3: SSE2 period and p4: post-SSE2 period.

SSEs	Thresholds	Periods Comparison	Z-value	Significance
SSE1	0.001	p1 and p2	1.0346	70%
	0.005	p1 and p2	0.4188	32%
	0.01	p1 and p2	0.4188	32%
SSE2	0.005	p2 and p3	-0.8451	60%
		p3 and p4	3.3169	99%

Table 3.4 Z-value and its significance within the stress triggering areas affected by the two SSEs for OOP receiver faults. p1: SSE1 period, p2: post-SSE1 period or pre-SSE2 period, p3: SSE2 period and p4: post-SSE2 period.

SSEs	Thresholds	Periods Comparison	Z-value	Significance
SSE1	0.001	p1 and p2	2.7683	99%
	0.005	p1 and p2	2.0123	96%
	0.01	p1 and p2	0.5678	43%
SSE2	0.005	p2 and p3	-1.6028	89%
		p3 and p4	3.8728	99%
	0.025	P2 and p3	-0.242	19%
		P3 and p4	1.8052	93%
	0.05	P2 and p3	-0.2962	23%
		P3 and p4	1.1187	74%

Chapter 4

Spatial Variation of Slip Behavior beneath the Alaska Peninsula along Alaska-Aleutian Subduction Zone[3]

4. 1 Abstract

We re-surveyed pre-existing campaign GPS sites and estimated a highly precise GPS velocity field for the Alaska Peninsula. We use the TDEFNODE software to model the slip deficit distribution using the new GPS velocities. We find systematic misfits to the vertical velocities from the optimal model that fits the horizontal velocities well, which cannot be explained by altering the slip distribution, so we use only the horizontal velocities in the study. Locations of three boundaries that mark significant along-strike change in the locking distribution are identified. The Kodiak segment is strongly locked, the Semidi segment is intermediate, the Shumagin segment is weakly locked and the Sanak segment is dominantly creeping. We suggest that a change in pre-existing plate fabric orientation on the downgoing plate has an important control on the along-strike variation in the megathrust locking distribution and subduction seismicity.

[3] Li, S., & Freymueller, J. T. (2018). Spatial variation of slip behavior beneath the Alaska Peninsula along Alaska-Aleutian subduction zone. Geophysical Research Letters, 45, 3453–3460. https://doi.org/10.1002/2017GL076761.

4.2 Introduction and Background

Subduction zones exhibit remarkable along-strike variations in seismic activity and in plate interface slip deficit worldwide. Understanding the cause of along-strike variations in slip behavior on the plate interface and seismic potential is important for better understanding the dynamic mechanical properties of the faults, and the rheology of the lower crust and lithosphere. Geodetic measurements can be used to study the process of the strain accumulation, and estimate the extent of plate interface frictional locking or moment deficit on the plate interface. The Alaska Peninsula, which includes the Shumagin and Semidi segments of the Aleutian subduction zone, features a dramatic along-strike transition from a widely locked region to a mainly creeping area on the plate interface (Fournier & Freymueller, 2007).

A magnitude 8.3 earthquake in 1938 last ruptured the subduction interface from west of Kodiak Island to east of the Shumagin segment (Johnson and Satake, 1994). Fournier and Freymueller (2007) estimated that the plate interface is almost fully locked (70%-90%) within the 1938 earthquake rupture zone (Figure 4.1a). The region between the 1946 earthquake (Ms 7.4) rupture zone and the 1938 earthquake (Mw 8.3) rupture zone was identified as a possible seismic gap in the 1970s (McCann et al., 1979). The eastern part of this region has a ~30% slip deficit, which is much smaller than the adjacent area within 1938 rupture zone, while the western part appears to be creeping at all depths (Fournier and Freymueller, 2007).

Marine seismic imaging studies in our study area document significant along-strike variations in the structure of the incoming plate that appear to be associated with changes in plate boundary behavior. Changes in the amount of bending faulting and sediment thickness on the incoming plate have been proposed to contribute to a more heterogeneous megathrust in the Shumagin Gap than in the Semidi segment, which could have consequences for plate boundary behavior (Bécel et al., 2017; Shillington et al., 2015).

Our main goal for this study is to characterize the slip deficit along this segment of the Aleutian subduction zone, and relate this to potential causes for the change in behavior. We inverted for the slip deficit distribution from a new dense GPS velocity field (Figure 4.1b). Then we identified the locations of the along-strike boundaries that mark the transition from strongly to weakly locked segments of the subduction margin, and explored their along-strike widths. We then correlate them with along-strike changes in pre-existing fabric on the downgoing plate, and subduction seismicity.

4.3 Data

We used three component GPS velocities from 78 sites along the Alaska Peninsula, surveyed between 1992 and 2016 (Figure 4.1b, Table 4.1) including both continuous and campaign stations. Subsets of the data were used earlier by Freymueller and Beavan (1999), Fletcher et al. (2001), Fournier and Freymueller (2007, 2008). New observations of 35 campaign sites were made within the Shumagins and the 1938 rupture zone to the northeast in May-June 2016. These sites all had past measurements from up to 20 years ago but many had been surveyed only once. With the long time span and additional measurements, we have a much denser site network than previous studies, with much lower uncertainties than the earlier GPS data sets. GPS sites located close to Veniaminof volcano have a large effect from volcano deformation (Fournier & Freymueller, 2008) and thus were not used (Figure 4.1a, orange dots).

We used the GIPSY/OASIS goa-5.0 software developed by Jet Propulsion Laboratory (JPL) to obtain daily coordinate and covariance estimates for all the used continuous and campaign GPS stations in the Alaska Peninsula using point positioning. The GPS data analysis method was the same as Li et al. (2016). We adopted the JPL non-fiducial orbits and clock products, and estimated a daily transformation for each daily solution into the ITRF2008 reference frame (Altamimi et al., 2011). We calculated velocities from the time series of each individual station by weighted least squares using all data within the survey period (1992 - 2016). We removed the GRACE-derived seasonal variation in the velocity fit (Zou et al., 2014) and estimated residual seasonal terms for the continuous sites. We also removed the geocenter translation rate error in ITRF2008 estimated by Argus et al. (2010) and rotated the velocities into a North America fixed reference frame. We also removed models for Glacial Isostatic Adjustment (GIA) (Hu and Freymueller, 2012) and 1964 postseismic deformation (Suito and Freymueller, 2009) from all GPS velocities. Both of these corrections have only a small effect within the study area.

The GPS velocity field (Figure 4.1b) reveals that the horizontal velocities are largest near the trench and decrease with distance from the trench due to elastic deformation from the locked subduction zone. There are also strong along-strike variations in the GPS horizontal velocities. Sites that are further east have larger velocities than those in the west, given the same distance from the trench. Sites in the west, especially within the Sanak segment, move in a nearly trench-parallel direction and show no variation in velocities with distance from the trench. The vertical velocities indicate that subsidence occurs in the eastern part of the Semidi segment and in the

Shumagin segment. Some sites in the Semidi segment and Sanak segment show subsidence and others show uplift.

4.4 Method

In general, all the continuous GPS sites and all campaign sites with multiple surveys show linear motion with a constant site velocity, with the exception of one small slow slip event (Appendix A.1 and Figure A.1, Table A.1). We found evidence for only minimal time variations in the slip distribution in the study region, so we assume that a constant velocity model describes all of the sites with only two surveys. We used TDEFNODE (McCaffrey, 2002) software to estimate the slip deficit rate distribution on the megathrust by inverting the GPS velocity data. We used Slab1.0 plate geometry (Hayes et al., 2012) to construct the slab interface. The slab was digitized about every 25 km in the along-strike direction and every 5 km in the downdip direction. We grouped together pairs of adjacent fault geometry nodes to have the same locking fraction, so the final grid of model parameters had 18 nodes in the along-strike direction and 7 nodes in the downdip direction, an average spacing of 50 km and 10 km, respectively.

The entire upper plate in the Alaska Peninsula moves relative to North America (Cross and Freymueller, 2008; Freymueller et al., 2008), and we must account for this motion via a block model to avoid biasing the estimated slip distribution on the megathrust (Li et al., 2016). The block model uses the Southern Alaska block (SOAK) from Fletcher (2002), the Bering plate (BRNG) from Cross and Freymueller (2008), the Peninsula block (PENN) modified from Li et al. (2016), and two major plates: NOAM and PCFC (Sella et al., 2007) (Appendix A.2 and Figure A.2). The estimated angular velocity of the PENN block in Li et al. (2016) used data from Cook Inlet and Alaska Peninsula; Cook Inlet appears to be moving slightly faster (~1 mm/yr) than the Alaska Peninsula, leading to systematic trench-parallel residual in the GPS velocities here. So we re-estimated the angular velocity of the PENN block using the sites within the Alaska Peninsula and sites in the eastern Aleutians as far west as Atka that show no strain from a locked megathrust, and excluding sites from Cook Inlet (Appendix A.2). The estimation of block rotation for PENN block used a different set of sites (Table 4.2) from those used in Li et al. (2016), selected to minimize potential biases from the locking model. After the estimation of the PENN block, we fixed all the block motions per Table 4.3 for the remaining inversions in this paper.

TDEFNODE combines spherical block rotations with interseismic fault locking distributions modeled as dislocations in an elastic half-space (Okada, 1985). Interseismic locking

describes the slip deficit rate distribution on the megathrust. The plate interface is represented by a grid of nodes, and the locking fraction ϕ (ratio of the slip deficit rate to the long-term slip rate) is estimated at each node on a continuous fault geometry. In all the inversion models, we restricted the locking ratio ϕ to the range [0, 1] where the brackets indicate minimum and maximum allowed locking values. Spatial smoothing in the along-strike and down-dip directions was applied in the estimation of locking distribution.

4.5 Results

We first estimated the locking distribution on the plate interface beneath the Alaska Peninsula using three component GPS velocities. In this inversion model, we applied Laplacian smoothing with the same smoothing factors in both along-strike and downdip directions. Varying the smoothing factors generate a series of solutions where the curvature of the locking pattern is damped to varying degrees (e.g., Li et al., 2016). After analyzing the trade-off curve, we find that the optimal smoothing factor are $2 \cdot 10^8$ using both horizontal and vertical velocities (Figure A.3) and $1 \cdot 10^8$ using horizontal velocities only (Figure A.4). In the abovementioned model, there are long-wavelength systematic misfits to the vertical velocities while the model fits the horizontal velocities fairly well. The vertical misfits cannot be explained by altering the slip distribution on the plate interface. Possible explanations for the systematic misfit are investigated in the Supplement (Appendix A.3, DeGrandpre, 2015). Because the vertical velocities appear to contain a significant component in addition to the subduction zone deformation, we only used the horizontal velocities for the remainder of this study.

4.5.1 Slip Model for Sub-segments

We found that a standard inversion model significantly over-smooths the locking distribution and underestimates the strong locking variations along-strike. In this inversion model, the area west of the Shumagin segment is barely affected by subduction strain, so high smoothing does not affect the slip distribution in this region (the best fitting slip deficit is nearly zero). However the eastern part of the Alaska Peninsula has large variation of locking values, so high smoothing will smooth out the strong along-strike variation in the locking distribution and cause large data misfit.

From this smoothed inversion model, we can easily identify four different patterns in the locking distribution. Therefore, we divided the plate interface into four segments based on the observed along-strike variation from strongly locked in the northeast to mostly creeping in the

southwest. We estimated the optimal smoothing factor and got the best fitting locking distribution for each segment individually (Figure 4.4). Then we averaged the locking values along-strike for each segment and combined all the segments to generate an initial locking distribution on the slab interface beneath the Alaska Peninsula. With this locking distribution, we constructed a forward model (Figure 4.5) with a smaller data residual than the smoothed inversion model (comparable to extremely rough models that contain obvious artifacts, see Appendix A.4, Figures A.4 and A.5). The improvement in data fit comes from having sharp along-strike boundaries, while strong along-strike smoothing within each segment does not degrade model fit.

4.5.2 Locating the Boundaries that Mark Sharp Changes in Locking

Given the optimal locking values estimated for each segment, we then varied the location and width of the along-strike transitions to determine where the optimal boundaries that mark the transitions in locking are located, and whether sharp or gradual changes in the locking distribution provide a better fitting model.

In order to locate the boundaries where there are sharp changes in locking distribution, we varied the location of the three potential boundaries indicated by the three node lines in Figure 4.2a. We varied the location of the first boundary from the first node line in the Kodiak segment to the last node line in the Sanak segment, and calculated the residual for each forward model with different locations of the first boundary. The locking distribution in the east side of the boundary is set to be the same as the optimal model in the first segment and the distribution in the west side of the boundary is the same as the forward model shown in Figure 4.5. The best location of the first boundary was selected based on the model that has the minimum of the weighted sum of squared residuals (WRSS). After locating the best position of the first boundary, we used the same method to test the best location of the second boundary starting from where the first boundary is located towards the last node line in the west, and then do the same for the third boundary.

The optimal locations of the boundaries are shown in Figure 4.2a. Strong along-strike variation in the estimated locking distribution (Figure 4.2c) is best described by step-wise decreases in the width of the locked region from the NE to the SW along strike. Besides that, there is a sharp decrease from strongly locked to weakly locked within a short distance in the downdip part of the Kodiak segment, which is different from the more gradual decrease in the locking fraction estimated for the other three segments. However, the strongest locking near the trench cannot be well constrained due to lack of data offshore. Animations A.1 to A.3 show the data

residuals and locking distribution for each forward model when we vary the location of each potential boundary. We also calculated the relative (fractional) increase in residuals above the best fit model, and showed the uncertainty range for the location of each boundary based on models that show less than a 20% relative increase in misfit (Figure 4.2). The locking fraction within the Semidi segment is poorly resolved due to lack of data near the trench (Figures 4.2 and A.5).

We next tested the possibility of gradual along-strike changes in the locking distribution in comparison to the sharp changes in locking assumed in the model of Figure 4.2a. We varied the width of each boundary tested above and checked how the WRSS changes with the width of the transition. A model with a gradual along-strike change in locking does not provide smaller misfit than the model with abrupt changes, and in most cases, the gradual change produced a worse fit to the data (Animations A.4 to A.6).

4.6 Discussion

4.6.1 Correlation between the Locking Distribution and the Plate Fabric from Magnetic Anomalies, and Subduction Seismicity

Atwater (1989) examined the magnetic anomaly isochron pattern in the northeast Pacific and its implications for the history of sea-floor spreading among the plates within the North Pacific Ocean basin. Her study indicated that the incoming oceanic lithosphere exhibits abrupt changes in seafloor fabric caused by the past seafloor spreading geometry. The pattern of abyssal hills and relic normal faults in the oceanic crust are aligned with the former spreading ridge. Three different pre-existing seafloor spreading ridge orientations were identified through the magnetic anomalies: (1) Kula-Pacific spreading from 80 to 56 (44?) Ma at an average rate of ~ 60 mm/yr (Green bold arrow in Figure 4.3a). (2) Farallon-Pacific spreading from 100 to 55 Ma at a full spreading rate of ~ 80 mm/yr (Magenta bold arrow in Figure 4.3a). (3) Vancouver-Pacific spreading from 53 to 30 Ma with the same rate as Farallon-Pacific spreading (Red bold arrow in Figure 4.3a).

Given the present motion of the Pacific plate, these lateral changes in plate fabric result in abrupt along-strike changes in the fabric of the downgoing plate entering the trench along the Alaska Peninsula. Along-strike variations in pre-existing fabric orientations in the Alaska Peninsula strongly correlate with variations in the estimated megathrust locking distribution within the subduction zone. The boundary located between the Kodiak segment and Semidi segment that marks the change from strongly locked to intermediate locked is correlated with the change in pre-existing plate fabric due to the cessation of the Kula-Pacific spreading (intermediate locked) and

beginning of the Vancouver-Pacific spreading (strongly locked) (Figure 4.3a). The boundary located between the Semidi segment and the Shumagin segment, which marks the significant change from intermediate to weakly locked, seems to be correlated with the change in pre-existing plate fabric where the northern portion of the Farallon plate broke off and became the Vancouver plate with a new spreading direction (Figure 4.3a). The boundary between the Shumagin segment and the Sanak segment, which marks the change from weakly locked to creeping dominated, is correlated with a major orientation change in two younger sections of pre-existing seafloor fabric indicated by the magnetic anomalies near the trench. These correlations suggest that the remnant seafloor structures in the subducting plate are an important control on along-strike variations in megathrust locking distribution within the Alaska Peninsula.

Shillington et al. (2015) proposed that more water is delivered into the subduction zone in the Shumagin segment than in the Semidi segment, where the pre-existing downgoing plate fabric is oriented nearly parallel to the trench and promotes bending faulting at the outer-rise, and that high pore fluid pressure due to hydration affects the intermediate depth seismicity (van Keken et al., 2011). The correlation between the pre-existing fabric orientation and the megathrust slip behavior in our study suggests that more bending faulting and hydration may promote sliding, perhaps through enhanced alternation of clay minerals in the fault zone. Areas where fluids are well-drained and remnant fabric is oriented highly oblique ($\geq 90^{o}$) to the trench may experience fluids migrating into and metamorphosing the permeable overlying plate, reducing the pore-fluid pressure at the megathrust (Nakajima & Hasegawa, 2016). The decreased pore-fluid pressure and fluid leakage increase the effective normal stress with no variation in friction coefficient in a conditionally stable friction regime, which can lead to stick slip behavior and thus a locked megathrust.

Wang and Bilek (2014) summarized that creeping is the dominant mode of subduction when the incoming seafloor is rough, and that smooth subducting seafloor results in thrust locking. They pointed out the Shumagin segment involved subduction of smooth seafloor and was an exception to this rule because it exhibited creep based on previous geodetic observations. However, when the normal faulting at the outer-rise is factored in with a relatively thin sediment cover, the seafloor coming into the trench is actually rougher than for the strongly locked Semidi segment where the faulted basement with a relative thick sediment may result in a relatively smooth contact at depth (Shillington et al., 2015). Therefore our study area actually agrees well

with the relationship between the roughness of seafloor and slip behavior expressed by Wang and Bilek (2014). To sum up, the change in pre-existing seafloor fabric structures contributes significantly to the recent locking distribution based on variation in fluid extent and seafloor roughness.

Shallow earthquakes (Figure 4.3b) are much more common in the regions that are dominated by creep (west of boundary 3) and near the trench in the strongly locked area (east of boundary 1), but are less common in between. Outer-rise earthquakes are more abundant in the creeping dominated area than the other three areas, and the change in the abundance of outer-rise earthquakes correlates with boundary 3. There are more intermediate-depth earthquakes in the creeping dominated area (west of boundary 3), fewer in the weakly and intermediate locked areas, and more again in the strongly locked area (east of boundary 1). The spatial pattern of those intermediate-depth earthquakes correlates well with the estimated boundaries in slip behavior within the seismogenic zone in Figures 4.2 and 4.3b.

In general, our results suggest that the change in locking distribution is correlated with the change in along-strike subduction seismicity distribution. Shillington et al. (2015) attributed the abundance of outer-rise earthquakes in the creeping segment to the abundant normal faults at the outer rise, and the greater number of intermediate-depth earthquakes to dehydration embrittlement due to high plate hydration. However, intermediate-depth earthquakes are again more abundant in the Kodiak segment, so their argument does not hold for the entire study area. The cause of the correlation pattern between shallow earthquakes and the locking distribution is unclear due to the high uncertainty in locations of those shallow events. For example, we do not know what fraction of those events is due to slip on the plate interface or to faulting in the overriding plate. Our results support the idea that the abundance of normal faults and the resulting hydration of the oceanic plate are both important mechanisms in controlling the locking behavior in comparison with the pre-existing plate fabric above. The change in the pre-existing seafloor fabric is an important control in variation in megathrust slip and seismicity behavior.

Our model shows distinctive variation in downdip extent of slip deficit along the length of the study area. Our estimated gradual downdip decrease in the locking fraction within the Semidi segment (Figures 4.2 and 4.3) can be compared with the identified variations in reflection characteristics of the megathrust fault with depth inferred from seismic reflection by Li et al. (2015). From trench to ~40 km landward, the observed two parallel reflections interpreted as the

top and bottom of subducted sediment section correlate well with the region of intermediate locking (~ 0.7). Then from ~50 to 95 km from the trench, the plate interface appears as a thin reflection band interpreted as a compacted sediment layer matches well with the region of weakly locking (~ 0.4). Within our region of almost creeping (≤ 0.2), they found a thick reflection band which may be interpreted as a wide deformation zone with branching faults.

Our estimated locking model also shows a correlation with the rupture history of past great earthquakes. The model shows a transition from strongly locked to intermediate locked within the 1938 rupture zone, which is in agreement with the identified two episodes of moment release during this event through waveform modeling, with the second and larger release occurring in the NE part of the rupture zone (Estabrook et al., 1994), which features a wider locked zone. The strongly locked region in the Kodiak segment agrees well with the suggested high moment release under Kodiak Island during 1964 earthquake (Christensen & Beck, 1994).

4.7 Conclusion

Our model shows three distinct changes in the locking distribution along-strike from strongly locked in the Kodiak segment, intermediate in the Semidi segment, weakly locked in the Shumagin segment, to a creeping-dominated zone in the Sanak segment. The width of the locked region decreases step-wise from NE to SW along strike. We find that the changes in pre-existing fabric orientation in the subducting oceanic plate are correlated with the along-strike changes in locking distribution based on variation in fluid extent and seafloor roughness. More outer-rise earthquakes are observed in the creeping-dominated area than in the other three areas. Shallow earthquakes are more common in the creeping-dominated area and near trench in the strongly locked area. More intermediate-depth earthquakes are located downdip of the creeping-dominated and strongly locked areas and fewer in between where the plate fabric is less uniform. The along-strike variations in the subduction seismicity mostly correlate with the changes in the locking distribution. Our study supports the idea that the pre-existing seafloor fabric in the downgoing plate changes the extent of hydration in the oceanic plate along strike, and that a strongly hydrated downgoing plate with rough seafloor is more likely to creep, which results in changes in megathrust fault locking distribution and the subduction seismicity.

4.8 Acknowledgement

We appreciate Editor Jeroen Ritsema, reviewer Laura Wallace and Donna Shilington for providing helpful comments that significantly improve the manuscripts. We acknowledge

EarthScope for the Plate Boundary Observatory (PBO) data, UNAVCO for operations of the PBO and Alaska Earthquake Center for management of the regional seismic network in Alaska. This research was supported by GeoPRISMS program (NSF award EAR-1457361) to the University of Alaska Fairbanks. We thank Max Kaufman for carrying out the GPS fieldwork in May 2016. We use the Generic Mapping Tools (GMT) (Wessel et al., 2013) to draw the figures. The raw data are available in the UNAVCO archive, and our velocities are in the supplement.

4.9 References

Altamimi, Z., Collilieux, X., & Métivier, L. (2011). ITRF2008: an improved solution of the international terrestrial reference frame. *Journal of Geodesy*, *85*(8), 457–473.

Argus, D. F., Gordon, R. G., Heflin, M. B., Ma, C., Eanes, R. J., Willis, P., et al. (2010). The angular velocities of the plates and the velocity of Earth's centre from space geodesy. *Geophysical Journal International*, *180*(3), 913–960.

Atwater, T. (1989). Plate tectonic history of the northeast Pacific and western North America. *The Eastern Pacific Ocean and Hawaii: Boulder, Colorado, Geological Society of America, Geology of North America, v. N*, 21–72.

Atwater, T., & Severinghaus, J. (1989). Tectonic maps of the northeast Pacific. *The Geology of North America*, 15–20.

Bécel, A., Shillington, D. J., Delescluse, M., Nedimović, M. R., Abers, G. A., Saffer, D. M., et al. (2017). Tsunamigenic structures in a creeping section of the Alaska subduction zone. *Nature Geoscience*, *10*(8), 609–613.

Christensen, D. H., & Beck, S. L. (1994). The rupture process and tectonic implications of the great 1964 Prince William Sound earthquake. *Pure and Applied Geophysics*, *142*(1), 29–53.

Cross, R. S., & Freymueller, J. T. (2008). Evidence for and implications of a Bering plate based on geodetic measurements from the Aleutians and western Alaska. *Journal of Geophysical Research: Solid Earth (1978–2012)*, *113*(B7).

Davies, J., Sykes, L., House, L., & Jacob, K. (1981). Shumagin Seismic Gap, Alaska Peninsula: History of great earthquakes, tectonic setting, and evidence for high seismic potential. *Journal of Geophysical Research: Solid Earth*, *86*(B5), 3821–3855. https://doi.org/10.1029/JB086iB05p03821.

DeGrandpre, K. (2015). *Relative Sea Level Change in Western Alaska as Constructed From Satellite Altimetry and Repeat GPS Measurements* (M. Sc. Thesis). University of Alaska Fairbanks.

Estabrook, C. H., Jacob, K. H., & Sykes, L. R. (1994). Body wave and surface wave analysis of large and great earthquakes along the Eastern Aleutian Arc, 1923–1993: Implications for future events. *Journal of Geophysical Research: Solid Earth*, *99*(B6), 11643–11662.

Fletcher, H. J. (2002). *Crustal deformation in Alaska measured using the Global Positioning System*. University of Alaska Fairbanks.

Fletcher, H. J., Beavan, J., Freymueller, J., & Gilbert, L. (2001). High interseismic coupling of the Alaska subduction zone SW of Kodiak island inferred from GPS data. *Geophysical Research Letters*, *28*(3), 443–446.

Fournier, T. J., & Freymueller, J. T. (2007). Transition from locked to creeping subduction in the Shumagin region, Alaska. *Geophysical Research Letters*, *34*(6).

Fournier, T. J., & Freymueller, J. T. (2008). Inflation detected at Mount Veniaminof, Alaska, with campaign GPS. *Geophysical Research Letters*, *35*(20).

Freymueller, J. T., & Beavan, J. (1999). Absence of strain accumulation in the western Shumagin segment of the Alaska subduction zone. *Geophysical Research Letters*, *26*(21), 3233–3236.

Freymueller, J. T., Woodard, H., Cohen, S. C., Cross, R., Elliott, J., Larsen, C. F., et al. (2008). Active deformation processes in Alaska, based on 15 years of GPS measurements. *Active Tectonics and Seismic Potential of Alaska*, *179*, 1–42.

Hayes, G. P., Wald, D. J., & Johnson, R. L. (2012). Slab1. 0: A three-dimensional model of global subduction zone geometries. *Journal of Geophysical Research: Solid Earth (1978–2012)*, *117*(B1).

Hu, Y., & Freymueller, J. T. (2012). Geodetic observations of Glacial Isostatic Adjustment in Southeast Alaska and its implication of Earth rheology. In *AGU Fall Meeting Abstracts*.

Johnson, J. M., & Satake, K. (1994). Rupture extent of the 1938 Alaskan earthquake as inferred from tsunami waveforms. *Geophysical Research Letters*, *21*(8), 733–736.

van Keken, P. E., Hacker, B. R., Syracuse, E. M., & Abers, G. A. (2011). Subduction factory: 4. Depth-dependent flux of H2O from subducting slabs worldwide. *Journal of Geophysical Research: Solid Earth*, *116*(B1).

Li, J., Shillington, D. J., Bécel, A., Nedimović, M. R., Webb, S. C., Saffer, D. M., et al. (2015). Downdip variations in seismic reflection character: Implications for fault structure and seismogenic behavior in the Alaska subduction zone. *Journal of Geophysical Research: Solid Earth*, *120*(11), 7883–7904.

Li, S., Freymueller, J., & McCaffrey, R. (2016). Slow slip events and time-dependent variations in locking beneath Lower Cook Inlet of the Alaska-Aleutian subduction zone. *Journal of Geophysical Research: Solid Earth*, *121*(2), 1060–1079.

McCaffrey, R. (2002). Crustal block rotations and plate coupling. *Plate Boundary Zones*, 101–122.

McCann, W. R., Nishenko, S. P., Sykes, L. R., & Krause, J. (1979). Seismic gaps and plate tectonics: seismic potential for major boundaries. *Pure and Applied Geophysics*, *117*(6), 1082–1147.

Nakajima, J., & Hasegawa, A. (2016). Tremor activity inhibited by well-drained conditions above a megathrust. *Nature Communications*, *7*, 13863.

Okada, Y. (1985). Surface deformation due to shear and tensile faults in a half-space. *Bulletin of the Seismological Society of America*, *75*(4), 1135–1154.

Sella, G. F., Stein, S., Dixon, T. H., Craymer, M., James, T. S., Mazzotti, S., & Dokka, R. K. (2007). Observation of glacial isostatic adjustment in "stable" North America with GPS. *Geophysical Research Letters*, *34*(2).

Shillington, D. J., Bécel, A., Nedimović, M. R., Kuehn, H., Webb, S. C., Abers, G. A., et al. (2015). Link between plate fabric, hydration and subduction zone seismicity in Alaska. *Nature Geoscience*, *8*(12), 961–964.

Suito, H., & Freymueller, J. T. (2009). A viscoelastic and afterslip postseismic deformation model for the 1964 Alaska earthquake. *Journal of Geophysical Research: Solid Earth (1978–2012)*, *114*(B11).

Wang, K., & Bilek, S. L. (2014). Invited review paper: Fault creep caused by subduction of rough seafloor relief. *Tectonophysics*, *610*, 1–24.

Wessel, P., Smith, W. H., Scharroo, R., Luis, J., & Wobbe, F. (2013). Generic mapping tools: improved version released. *Eos, Transactions American Geophysical Union*, *94*(45), 409–410.

Zou, R., Freymueller, J. T., Ding, K., Yang, S., & Wang, Q. (2014). Evaluating seasonal loading models and their impact on global and regional reference frame alignment. *Journal of Geophysical Research: Solid Earth*, *119*(2), 1337–1358.

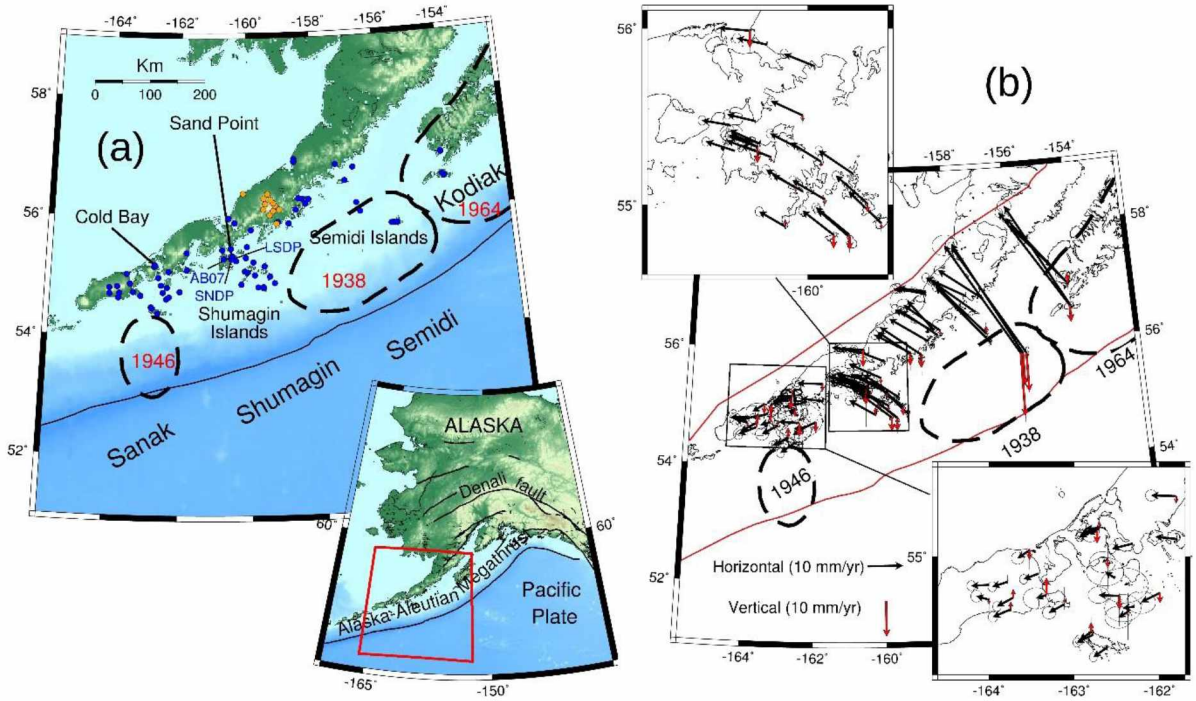

Figure 4.1 Tectonic setting and Observed GPS velocities for stations in the Alaska Peninsula. (a) Topographic map and tectonic setting (inset) of the study area on the Alaska Peninsula (red rectangle in inset map). Black dashed outlines show the rupture zone of past large earthquakes (Davies et al., 1981). Major towns are marked. The Alaska Peninsula are divided into four segments: Sanak, Shumagin, Semidi and Kodiak. Blue dots are GPS stations used in this study. Orange dots are GPS stations with significant volcano deformation. (b) Observed GPS velocities in horizontal (black) and vertical (red) for stations in the Alaska Peninsula.

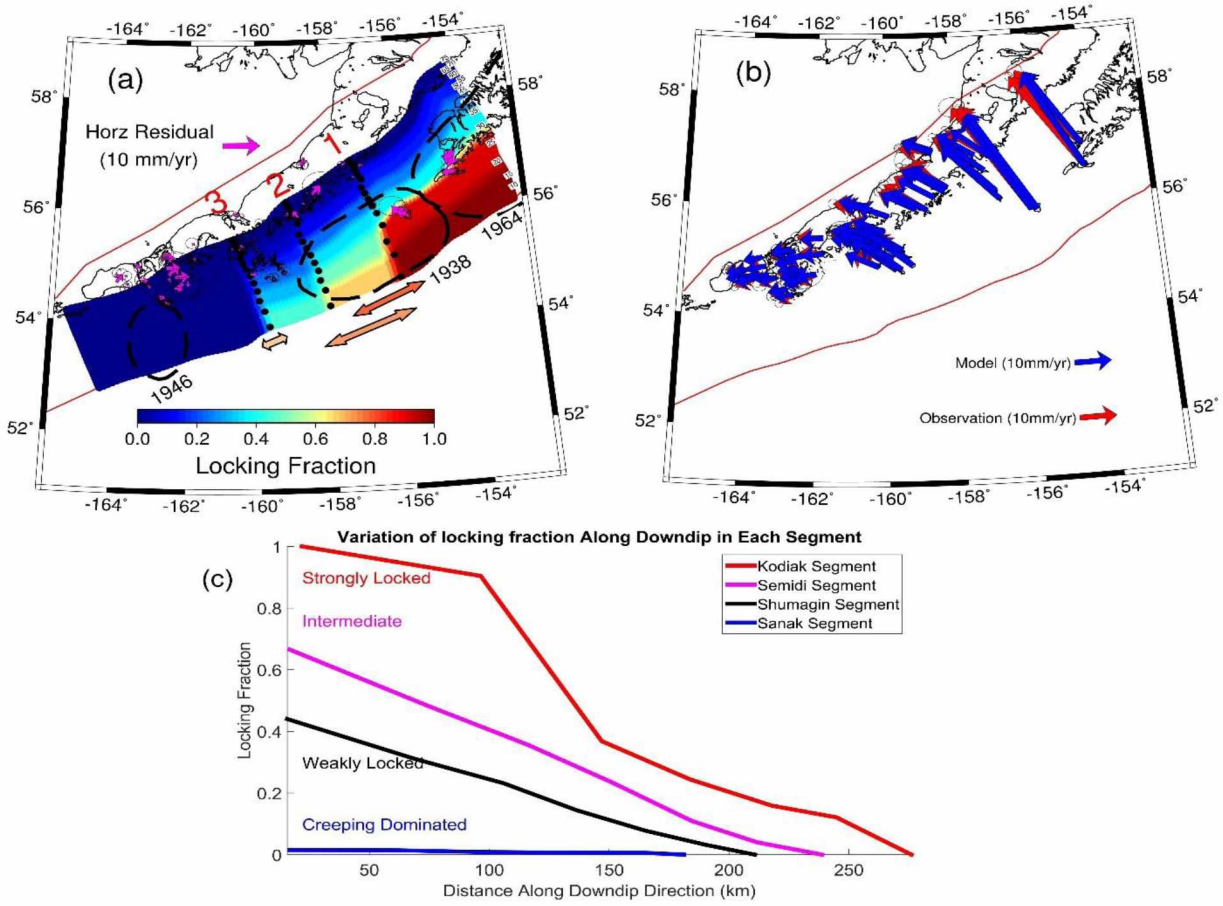

Figure 4.2 Optimal Locking model, Observed and modeled GPS velocities and variation of the locking fraction in the downdip direction. Best fitting model which has the optimal locations of three boundaries mark the sharp changes in locking (a). The orange arrow spans the uncertainty range of the location for the first boundary ($^{+25}_{-125}$) km (+ means NE direction, - means SW direction). The yellow-orange arrow spans the uncertainty range of the location for the second boundary ($^{+150}_{-50}$) km. The light-orange arrow spans the uncertainty range of the location for the second boundary ($^{+25}_{-25}$) km. The observed versus modeled GPS horizontal velocities in the best fitting model (b). Variation of the locking fraction in the downdip direction for each segment from strongly locked to creeping dominated (c).

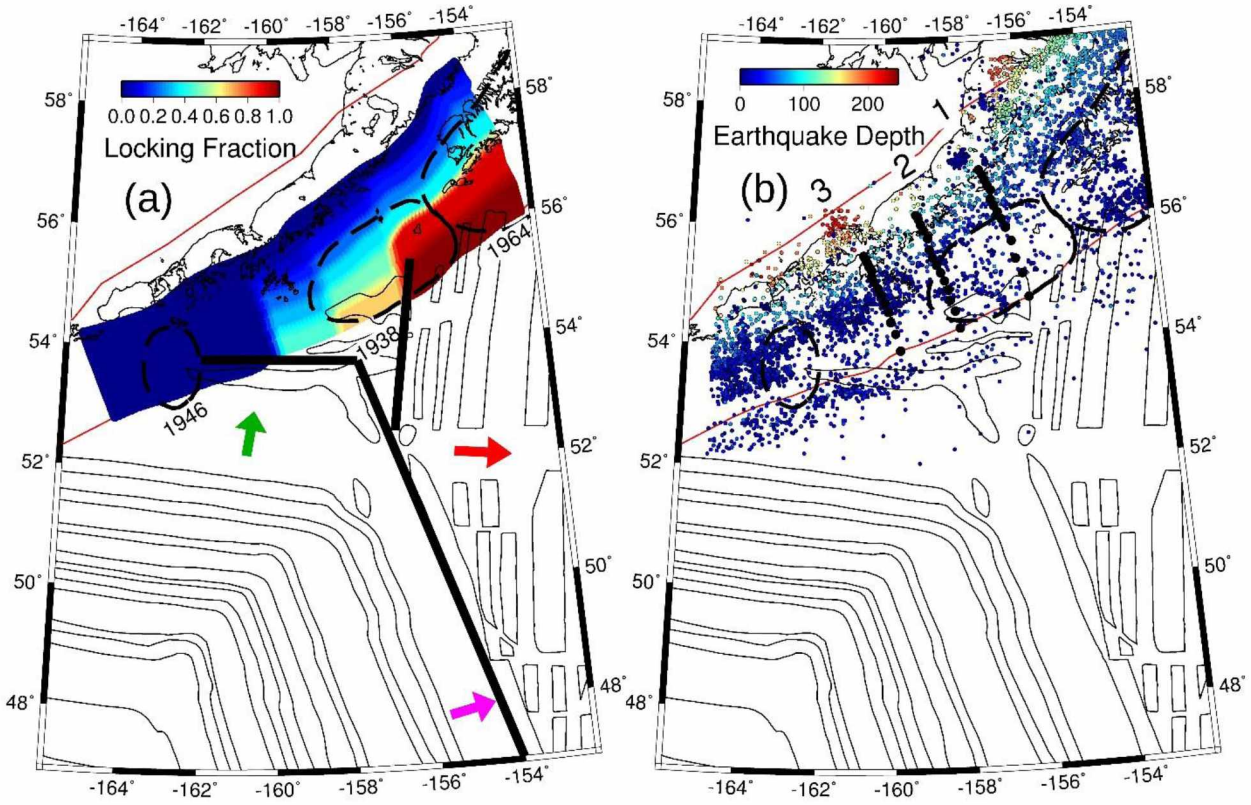

Figure 4.3 Correlation among fault locking, pre-existing plate fabric and subduction seismicity. (a) Relationship between significant changes in estimated fault locking and change in pre-existing plate fabric based on magnetic anomaly. Digital magnetic anomaly polygons provided by Peter Haeussler and Keith Labay. The original magnetic anomaly data comes from Atwater (1989) and Atwater and Severinghaus (Atwater & Severinghaus, 1989). Green arrow indicates the spreading direction of the Kula-Pacific spreading center, magenta arrow indicates the spreading direction of the Farallon-Pacific spreading center, and red arrow shows the spreading direction of the Vancouver-Pacific spreading center. The black lines are corresponding to the change in pre-existing plate fabric due to the seafloor spreading history based on the magnetic anomalies. (b) Seismicity (Magnitude > 3.0) from the Alaska Earthquake Center (AEC) from 1990 to present. Numbers 1-3 mark the sharp boundaries of the locking changes.

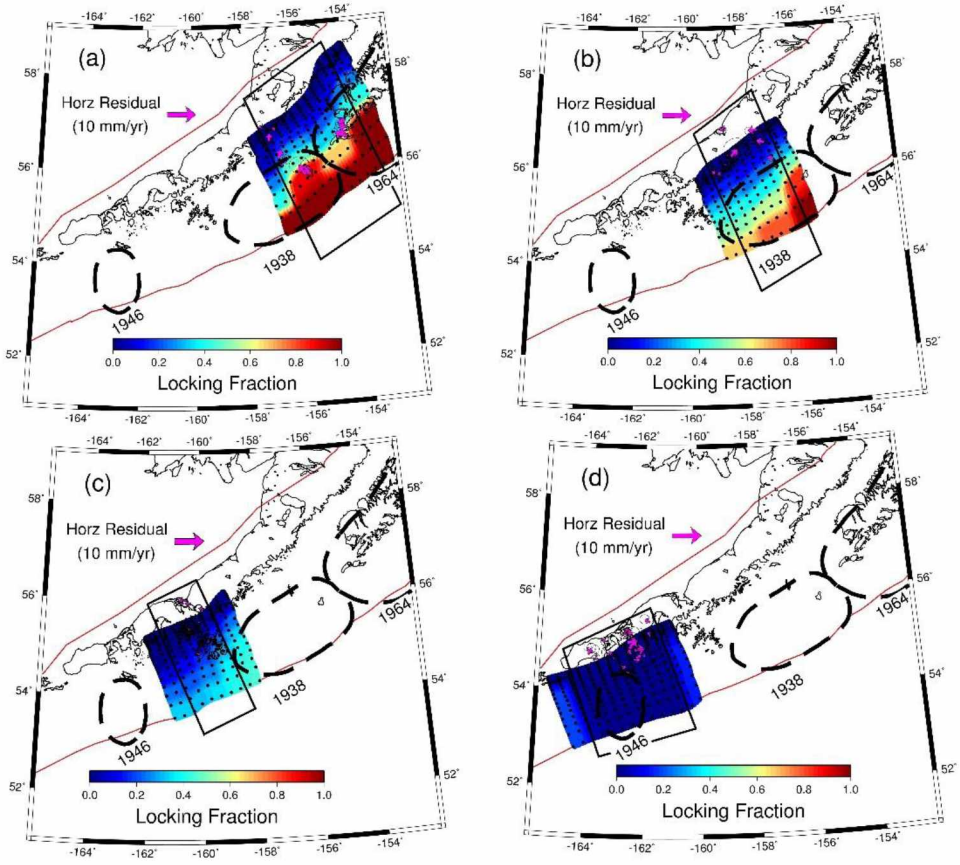

Figure 4.4 Best fitting model and selection of optimal locking ratios for each segment (a: strongly locked; b: intermediate; c: weakly locked; d: creeping-dominated). Magenta arrows show the horizontal residuals (mm/yr) of the sites that used in each optimal model. The black rectangles show the chosen segments; the model was averaged along-strike within each box.

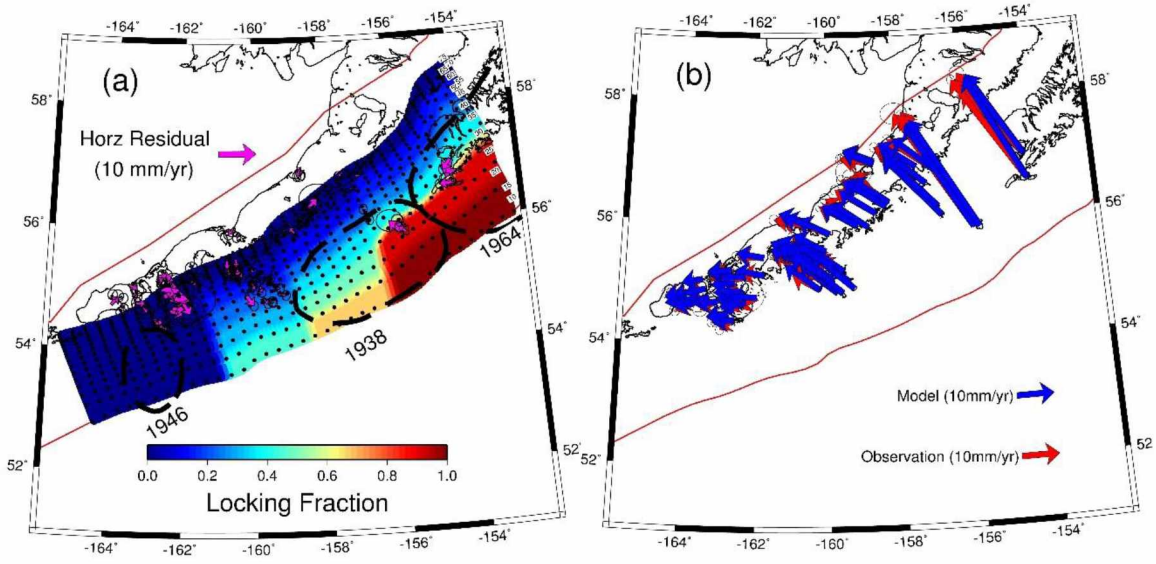

Figure 4.5 Forward locking model (a) and observed versus modeled horizontal GPS velocities in the forward model (b) based on our best estimation of locking distribution in the four individual segments within the Alaska Peninsula.

Table 4.1 GPS site locations, velocities and associated uncertainties in the horizontal (east and north) component and vertical component, and names. Velocities are based on the survey period (1992 - 2016). Column 1. Station Names; Column 2. Site position, Longitude; Column 3. Site position, Latitude; Column 4. East velocity (mm/yr); Column 5. East standard deviation (mm/yr); Column 6. North velocity (mm/yr); Column 7. North standard deviation (mm/yr); Column 8. Vertical velocity (mm/yr); Column 9. Vertical standard deviation (mm/yr).

Name	Long	Lat	Ve	Se	Vn	Sn	Vz	Sz
1293	199.49744	55.33200	-7.380	1.310	3.900	1.000	-4.520	2.600
3502	199.42175	55.98659	-8.850	0.520	0.800	0.570	-4.750	0.640
891G	201.59600	56.29512	-7.170	1.990	8.630	1.640	0.640	4.630
9016	201.18123	55.88859	-11.370	0.550	8.190	0.570	-3.720	0.890
9450	199.49963	55.33114	-7.960	0.440	3.050	0.530	-1.970	0.310
9758	198.20791	55.11905	-6.250	0.500	0.660	0.550	-0.240	0.560
AHKI	205.82539	56.94108	-14.980	0.510	18.030	0.570	2.880	0.730
ALIK	199.22671	55.45543	-8.020	0.450	1.340	0.540	-0.530	0.330
AND2	199.91324	55.32339	-8.180	0.460	4.210	0.540	-0.560	0.320
ASPE	202.62795	56.85380	-11.000	0.440	5.830	0.530	0.440	0.300
BIRD	200.25709	54.82921	-8.770	0.450	6.810	0.530	-3.830	0.290
CENT	200.06897	55.78855	-8.650	0.460	3.440	0.540	-1.090	0.350
CHIR	204.27150	55.82588	-17.880	0.660	32.390	0.650	-9.160	1.020
CHN1_CHNB	200.41733	54.81466	-9.070	0.440	7.770	0.530	-3.550	0.300
CHRN	197.63069	54.62904	-2.720	1.560	-1.570	1.270	-1.410	2.680
CLFF	201.70080	56.21148	-10.120	0.440	7.320	0.530	-0.060	0.310
CONG	200.50347	56.22066	-13.760	2.090	3.590	1.610	9.020	4.410
CROW	197.19898	54.49083	-3.230	0.530	-2.210	0.570	2.760	0.570
DAY	197.52907	54.73546	-5.890	1.200	0.280	0.960	-3.890	1.870
EC44	200.63157	56.03191	-4.480	0.650	2.180	0.630	-1.100	1.040
FAWN	197.64481	54.82458	-1.400	2.780	-0.740	2.020	-0.980	4.630
FING	200.79154	56.19125	-4.020	0.860	2.390	0.740	4.250	1.570
FOG	200.45915	56.31583	-10.780	0.770	2.850	0.720	0.470	1.390
FOUR	199.27164	55.30900	-8.190	0.450	2.660	0.530	0.010	0.270
HARP	200.73711	56.23664	-3.400	0.870	4.580	0.760	8.260	1.660
HEID	201.38766	56.96388	-7.740	0.450	1.220	0.540	-0.580	0.330
HUEY	203.14463	56.79436	-12.070	0.440	8.850	0.530	-0.150	0.310
INSU	200.44942	55.17962	-9.670	0.440	6.540	0.530	-0.470	0.240
ISLK	201.39968	56.11342	-10.670	0.480	6.750	0.550	0.010	0.510
JIMM	201.38255	56.91688	-8.180	0.530	1.940	0.580	-0.750	0.690
KARP	199.94750	55.51036	-8.950	0.460	4.120	0.540	-1.690	0.310
KATY	196.47618	55.04427	-3.330	0.730	-2.240	0.690	-2.750	1.140

Table 4.1 cont.

Name	Long	Lat	Ve	Se	Vn	Sn	Vz	Sz
KITS	201.79328	56.28817	-10.030	0.800	7.620	0.720	-1.410	1.370
KOPP	199.63324	55.27378	-8.410	0.450	3.400	0.530	-1.200	0.270
LAG	197.70320	54.66411	-3.230	2.100	-0.430	1.580	0.600	3.510
LATE	204.20592	55.82304	-19.310	1.420	32.110	1.180	-17.760	2.350
LITT	200.59643	55.00727	-8.950	0.440	7.970	0.530	-2.360	0.260
LONE	198.00396	54.75572	-5.350	1.680	-2.640	1.290	-2.800	2.690
LSDP	199.50484	55.30205	-8.940	0.450	3.320	0.540	-1.160	0.320
MOUN	199.77436	54.87637	-7.380	0.460	4.270	0.540	2.100	0.330
OLET	200.67226	56.29035	-4.910	1.040	4.680	0.880	4.000	1.930
PANK	196.88680	54.67909	-4.360	0.770	-2.380	0.710	1.620	1.310
PETE	197.38103	54.38387	-3.760	0.450	-2.700	0.540	0.840	0.300
PEVA	200.84544	55.90986	-8.920	0.520	6.400	0.560	-3.330	0.580
PV02	198.19509	55.40581	-7.080	0.670	0.210	0.650	-2.070	1.100
RDMD	200.73319	56.10194	-4.480	1.080	1.400	0.880	3.570	2.050
REEF	197.47702	54.85738	-2.750	2.150	1.750	1.630	0.680	3.620
SATT	197.26802	55.17378	-1.910	0.900	-1.110	0.820	-3.560	1.380
SDP1	199.52450	55.35301	-8.920	0.870	2.230	0.700	0.550	1.160
SEMI	203.30786	56.04807	-14.460	0.440	16.590	0.530	0.620	0.310
SENI	199.85659	56.39762	-7.410	0.480	0.970	0.550	-1.570	0.480
SITK	205.86414	56.54028	-16.120	0.810	30.180	0.750	0.400	1.280
SMNF_SIME	200.73272	54.89667	-9.240	0.450	8.920	0.540	-1.610	0.320
SNDP	199.52451	55.35232	-8.470	0.560	2.200	0.580	0.930	0.520
STAR	200.83012	55.89358	-10.470	0.500	5.800	0.560	-0.830	0.610
SWED	199.47779	55.47776	-7.990	0.450	1.870	0.540	-0.630	0.300
TELE	197.39532	54.98441	-1.530	1.500	-0.830	1.210	-2.380	2.500
TOMH	196.67717	54.74136	-2.930	1.500	-0.930	1.230	4.880	2.610
TRNR	200.16416	55.03361	-8.990	0.440	5.300	0.530	-1.460	0.250
TWIN	200.44541	56.13265	-11.390	1.690	3.840	1.320	10.310	3.430
VSG	200.91345	56.12408	-8.250	1.020	5.190	0.880	-1.020	1.930
WEDG	200.13156	55.24827	-8.680	0.460	5.420	0.540	-1.340	0.340
WIK	202.89138	56.57646	-11.970	0.440	9.600	0.530	0.250	0.290
WOOL	199.87667	55.09769	-8.350	0.480	5.200	0.550	-1.200	0.420
YAST	200.57973	56.38560	-6.560	0.930	1.930	0.810	1.480	1.730
YUK	203.19800	56.19511	-13.580	0.440	14.760	0.540	2.200	0.330
AB06	196.57655	54.88532	-4.060	0.470	-1.530	0.550	0.300	0.370
AB07	199.52324	55.34928	-8.490	0.450	3.830	0.550	-0.920	0.350
AB13	201.49621	56.30733	-9.850	0.450	6.230	0.550	-0.430	0.370

Table 4.1 cont.

Name	Long	Lat	Ve	Se	Vn	Sn	Vz	Sz
AC02	205.81696	56.95059	-15.660	0.420	19.970	0.530	-1.180	0.260
AC12	200.41044	54.83096	-9.330	0.460	7.630	0.550	-1.920	0.380
AC13	204.37760	55.82190	-18.900	0.430	31.630	0.540	-10.940	0.290
AC21	200.87228	55.92109	-10.080	0.440	5.470	0.530	-0.980	0.270
AC25	197.68595	55.08897	-5.870	0.450	-1.470	0.540	0.150	0.320
AC28	199.95084	55.07849	-8.590	0.440	4.700	0.540	-0.500	0.290
AC40	201.38143	56.93035	-8.930	0.440	1.570	0.540	0.050	0.290
AC41	199.59270	55.90867	-8.550	0.480	1.820	0.570	0.970	0.470
AC42	197.21635	54.47178	-4.470	0.450	-2.150	0.540	1.540	0.310
AC45	205.81904	56.56445	-17.420	0.430	28.070	0.530	-4.710	0.280
AV34	196.28708	54.72491	-4.630	0.490	-2.530	0.570	2.320	0.470
AV37	196.00277	54.70938	-3.590	0.630	1.050	0.690	-1.290	0.930
AV38	196.21913	54.83147	-4.290	0.500	-1.390	0.570	0.650	0.500
AV39	196.00153	54.81134	-4.990	0.510	-0.270	0.580	-0.200	0.540
AV40	196.25703	54.64454	-5.020	0.550	-2.120	0.610	2.140	0.680
BAY1	197.29284	55.19027	-5.400	0.450	-2.430	0.540	-0.090	0.290
BAY2	197.29324	55.19042	-5.620	0.460	-2.350	0.540	0.060	0.340
BAY5	197.29284	55.19027	-5.320	0.450	-1.620	0.540	0.080	0.310
BAY6	197.29324	55.19042	-5.040	0.450	-1.350	0.540	-0.590	0.320
CDB7	197.28153	55.20034	-4.970	0.490	-2.090	0.570	0.320	0.490
CDB8	197.29360	55.19237	-4.020	0.560	-0.050	0.630	1.880	0.750

Table 4.2 GPS site locations, velocities and associated uncertainties in the horizontal (east and north) component, and names for sites used in estimating the new pole for PENN block in Appendix A.2 (Survey period: 1992 - 2016).Sites were chosen based on an observed lack of subduction-related strain, and we assume that this component is zero (rigid body rotation only). Column 1. Station Names; Column 2. Site position, Longitude; Column 3. Site position, Latitude; Column 4. East velocity (mm/yr); Column 5. North velocity (mm/yr); Column 6. East standard deviation (mm/yr); Column 7. North standard deviation (mm/yr); Column 8. Correlations.

Name	Long	Lat	Ve	Vn	Se	Sn	Rho
BAY1	197.29284	55.19027	-5.400	-2.430	0.450	0.540	0.000
BAY2	197.29324	55.19042	-5.620	-2.350	0.460	0.540	0.000
AB06	196.57655	54.88532	-4.060	-1.530	0.470	0.550	0.000
BAY5	197.29284	55.19027	-5.320	-1.620	0.450	0.540	0.000
CHRN	197.63069	54.62904	-2.720	-1.570	1.560	1.270	0.000
CROW	197.19898	54.49083	-3.230	-2.210	0.530	0.570	0.000
FAWN	197.64481	54.82458	-1.400	-0.740	2.780	2.020	0.000
PETE	197.38103	54.38387	-3.76	-2.7	0.45	0.54	0.000
REEF	197.47702	54.85738	-2.750	1.750	2.150	1.630	0.000
TELE	197.39532	54.98441	-1.530	-0.830	1.500	1.210	0.000
9758	198.20791	55.11905	-6.250	0.660	0.500	0.550	0.000
DAY	197.52907	54.73546	-5.890	0.280	1.200	0.960	0.000
KATY	196.47618	55.04427	-3.330	-2.240	0.730	0.6900	0.000
LAG	197.70320	54.66411	-3.230	-0.430	2.100	1.580	0.000
LONE	198.00396	54.75572	-5.350	-2.640	1.680	1.290	0.000
PANK	196.88680	54.67909	-4.360	-2.380	0.770	0.710	0.000
PV02	198.19509	55.40581	-7.080	0.210	0.670	0.650	0.000
SATT	197.26802	55.17378	-1.910	-1.110	0.900	0.820	0.000
TOMH	196.67717	54.74136	-2.930	-0.930	1.500	1.230	0.000
AC25	197.68595	55.08897	-5.870	-1.470	0.450	0.540	0.000
AC42	197.21635	54.47178	-4.470	-2.150	0.450	0.540	0.000
AV34	196.28708	54.72491	-4.630	-2.530	0.490	0.570	0.000
AV40	196.25703	54.64454	-5.020	-2.120	0.550	0.610	0.000
BAY6	197.29324	55.19042	-5.040	-1.350	0.450	0.540	0.000
CDB7	197.28153	55.20034	-4.970	-2.090	0.490	0.570	0.000
CDB8	197.29360	55.19237	-4.020	-0.060	0.560	0.630	0.000
ACHU	185.75300	52.17912	-4.210	-2.440	0.750	0.690	0.000
AKUN	194.40666	54.21068	-4.640	-2.090	0.580	0.580	0.000
ATKA	185.79333	52.21846	-2.460	-3.220	0.650	0.660	0.000
DCH1	193.47240	53.88867	-3.940	-2.470	0.460	0.540	0.000

Table 4.2 cont.

Name	Long	Lat	Ve	Vn	Se	Sn	Rho
DEC2	185.83073	52.23135	-3.400	-2.950	0.720	0.620	0.000
DHFA	193.45150	53.90465	-4.120	-2.350	0.700	0.640	0.000
DT16	193.46879	53.87398	-6.040	-2.610	0.910	0.770	0.000
DT19	193.46719	53.87446	-4.780	-2.540	0.820	0.740	0.000
DTOC	193.46364	53.87596	-0.020	-5.020	5.200	3.150	0.000
GUNN	193.48362	53.92385	-4.080	-2.510	0.500	0.550	0.000
ILIU	193.51511	53.85243	-3.940	-2.650	0.500	0.550	0.000
PUPA	185.76394	52.19952	-5.240	-2.170	0.780	0.700	0.000
ROTK	194.47919	54.06372	-4.740	-2.600	0.830	0.680	0.000
SBS2	193.48473	53.89742	-3.960	-2.580	0.530	0.580	0.000
WNDA	185.71100	52.16110	-4.020	-1.820	0.740	0.680	0.000
AB01	185.79524	52.20951	-6.770	-0.410	0.510	0.550	0.000
AV09	193.45817	53.87564	-5.130	-2.300	0.460	0.540	0.000
DUTC	193.45152	53.90501	-3.920	-0.870	0.570	0.620	0.000
MREP	193.25166	53.80960	-4.350	-1.950	0.510	0.580	0.000
MSWB	193.21212	53.91469	-5.090	-1.620	0.530	0.590	0.000
MHAA_MAPS	193.05955	53.80810	-4.960	-1.740	0.480	0.550	0.000

Table 4.3 Block Poles, Location of Poles, and Angular Speed of the Block Model, Relative to the North American Plate.

Block Name	Latitude of Pole	Longitude of Pole	Angular Speed (deg/Ma)	Source
SOAK	59.6000	212.6002	0.7700	(Fletcher, 2002)
PCFC	50.1734	284.1136	-0.7696	(Sella et al., 2007)
BRNG	43.9007	125.6082	-0.0638	(Cross and Freymueller, 2008)
PENN	-26.841	218.683	0.045	Estimated in this study

Chapter 5

General Conclusion

In subduction zones, the lithosphere is recycled into the mantle and the sinking of the lithosphere provides a significant contribution to the plate motion and the diversity of deformation including fast earthquakes, slow earthquakes, tsunami and volcanic eruption process, etc. Studying the dynamic mechanisms related to those active deformation processes can help us better understand the dynamics of subduction. Currently, the increasing development of GPS and seismic observations combined with tide gauge data, magnetic anomaly and gravity, etc, have helped to explore the characteristics of those deformation processes in subduction zones. The main goal for my thesis has been to utilize modern geodetic techniques with other observations in order to analyze and understand the dynamic mechanisms related to slow earthquakes and the along-strike variation in slip behavior in the Alaska-Aleutian Subduction Zone. This helps us gain more insight into the realistic assessment of seismic hazards in this area which are demonstrated in the previous chapters.

Two long-term SSEs were detected using campaign and continuous GPS observations in Lower Cook Inlet, Alaska in Chapter 2. Three different criteria for significance of the velocity change corresponding to the SSEs were explored for identifying the timing of velocity changes: the relative difference of the data misfit, the absolute difference of data misfit and the magnitude of velocity change. The second criteria produces the most spatially coherent set of sites with significant changes and the timing of velocity changes are in late 2004, the end of 2009, and late 2011. Unlike other SSEs observed in Alaska, the slip rates appear to be relatively constant during these two SSEs. The timing of each velocity change had a spatial progression, with the velocity changes propagating in either the updip or downdip direction. We also developed a new block model with a new block named the Peninsula block (PENN) that includes both the Alaska Peninsula and the Kenai Peninsula. We estimated the angular velocity of PENN, but fixed the poles of all the other plates and blocks at their published values. A single angular velocity explains the block motion well from all time periods including inter-SSE and SSE periods. We then estimated the slip deficit rate distribution for the inter-SSE and SSE periods with two different limiting ranges of the locking fraction (ϕ): [-2, 1] and [0, 1]. The GPS observations require negative slip deficit rates in the Lower Cook Inlet area in the SSE periods, which indicates that slip rates were faster than the plate convergence rates during these two time periods. The first SSE

lasted at least 9 years, as it was already underway when our observations in that area began in 1995. The second SSE in the same area lasted almost 2 years from end of 2009 to the end of 2011. Based on the geodetic slip inversion, the two SSEs were both located at the same depth range of 40 to 60 km, at the downdip end of the locked zone, which is presumably the transition zone. A checkboard test allows us to confirm that the model resolution is constrained well in the Lower Cook Inlet area where there is sufficient number of data, but not in the near-trench region where we don't have offshore data.

Over such a long time range, SSEs contribute significantly to the interseismic deformation through the seismic cycle in the Alaska-Aleutian subduction zone. SSEs especially play a crucial role in the cycle of strain accumulation and release in subduction megathrusts. Chapter 3 examined the relationship between SSEs and earthquakes in the Alaska-Aleutian subduction zone and checked whether SSEs have a large impact on the seismicity rate in the surrounding areas by using Coulomb stress calculations and the rate/state quantitative model. We found a good correlation between increasing stressing rates due to SSE slip and increases in seismicity rate during the SSEs period for the 30 – 60 km depth range. No similar correlation was found for areas within the 0 – 30 km and 60 – 90 km depth range. A z-value analysis suggested significant seismicity rate changes due to the SSEs in most of the selected stress triggering areas. Slip in the long-term SSEs stressed the adjacent faults, therefore increasing the seismicity rate even though the optimal fit for the ratio of the stressing rate due to the SSEs to the background stressing rate was small. Based on the previous studies of the slip distribution of all the detected long-term SSEs in Alaska, we estimated that the four long-term SSEs in Cook Inlet caused significant stress changes that would promote failure up-dip of the SSE area within the seismogenic zone. Our results indicated that long-term SSEs change the stress field in the seismogenic zone significantly. Future work is necessary to assess the temporal variation in slip migration pattern during the long-term SSEs and how these variations affect the surrounding stress field and seismicity.

Chapter 4 mainly focused on the along-strike and downdip variations in slip behavior beneath the Alaska Peninsula on the slab where there was no temporal variation in displacement detected by the geodetic observations. This study explored the possible mechanisms for the causes of such strong variation in slip behavior in the Alaska-Aleutian subduction zone. The changes in the orientation of the pre-existing fabric of the subducting oceanic plate, the subduction seismicity patterns, and the rupture history of past great earthquakes were found to be correlated with the

identified along-strike changes in the locking distribution. A lack of resolution near the trench and offshore was largely due to the shortage of data offshore and the long distance from the shoreline to the trench. Future work can be expanded to construct a new interplate geometry and explore the surrounding geologic evidence of splay faults in the shallow region based on the upcoming offshore-onshore seismic experiment.

Through the research detailed in this thesis, we have improved our understanding of the applicability of the GPS observations in detecting the long-term aseismic slip signal embedded in the steady tectonic movement; characterized the relationship between long-term SSEs and regular earthquakes in the subduction zone and quantified the possible triggering effect from long-term SSEs in the seismogenic zone which provides significant insight into the next possible megathrust earthquake; and resolved the details of transitions among dominantly locked, intermediate locked and dominantly creeping behavior beneath the Alaska Peninsula and correlated them with the features of the downgoing plate, seismicity patterns and rupture history of past great earthquakes through other observations over long time scales. This research has thus added to our knowledge of understanding the dynamic processes in the subduction zone and what controls and impacts those dynamic processes through modern and past observations.

Appendix A

Support Information for Chapter 4

A.1 Example of GPS Time Series in the Alaska Peninsula

In the Alaska Peninsula, all the GPS stations show linear motion through the whole survey period (1992 - 2016), with two exceptions. PBO site AB07 in Sand Point, set up in 2004, reveals a small gradual displacement (8 ± 1 mm) in the north component as shown in the red shaded area starting from about May 2011 (Figure A.1). We modeled this slow displacement as a hyperbolic tangent centered on 2011.5 with a time constant of 0.45 years. There is a 7.6 ± 1.6 mm displacement in the vertical component, and no significant displacement in the east component. Two earthquakes (M5.7 and M5.8) happened near the beginning of this event (May 2011), at 36 km depth and 28 km south of site AB07. The velocity before this event is the same as the velocity afterward. We interpret this as a slow slip event (SSE). AB28, the nearest continuous site to AB07, shows no significant displacement over this time, while AC12 on Chernabura Island in the Outer Shumagins shows a possible small eastward displacement. No other continuous sites show a displacement at this time. Velocities for co-located campaign sites near the continuous site AB07 in Sand Point, SNDP and LSDP, are listed in Table A.1. The SNDP and LSDP velocities are almost identical to the velocity for site AB07 (Table A.1). The impact of this SSE on site velocities at the campaign sites averaged over 20 years is small, less than 0.7 mm/yr. There were no $M > 5$ earthquakes within 75 km of the site SNDP from 1994 to 2010, but the 1993 survey was only 2 months after M6.9 earthquake which could include a potential postseismic effect. Given the nearly identical campaign and continuous velocities, we think it is likely that the small offset started in May 2011 was the only slow slip event (SSE) here in the time span 1993 – 2016.

A.2 Estimation of Angular Velocity of PENN Block using Stations in the Alaska Peninsula and further west

Using the angular velocity of the Peninsula block (PENN) estimated by Li et al. (2016) leads to a systematic residual in the GPS horizontal velocities in the trench-parallel direction for sites within the Alaska Peninsula. That pole was estimated using data from the Cook Inlet area along with a subset of the data used here for the Alaska Peninsula. Analysis of the residuals shows that Cook Inlet moves slightly faster in the trench-parallel direction than the Alaska Peninsula, by

~1 mm/yr. Using inversions for the pole based on different data sets, we found that the eastern Aleutian Islands as far west as Atka and the Alaska Peninsula move as a rigid block with very small misfit, and with a velocity distinct from the Cook Inlet area. Therefore, we re-estimated the angular velocity of the PENN block using GPS sites within the Alaska Peninsula and eastern Aleutians (Dutch Harbor and Atka) that are in segments of the arc that do not show strain related to elastic deformation from the locked subduction zone (Table 4.2).

The location of the pole for a small block like the PENN block is very sensitive to small changes in the data set used in the inversion. However, even when the pole changes by a large amount, the predicted linear velocities across the block do not change much; this reflects the reality that one component of the angular velocity vector is poorly constrained. In addition, for a small block located far enough from its pole, the inversion problem may have two nearly equal solutions, located on opposite sides of the block and with opposite senses of rotation (like a mirror image). This is true as long as the pole is located a large angular distance away from the block, so that all of the linear velocity vectors within the block are nearly parallel. In such a case noise in the velocities can flip the best-fit solution between the two "mirror image" poles. We found that this was the case when using different subsets of data only from the Alaska Peninsula and/or Cook Inlet. Adding the data from the Dutch Harbor and Atka areas, where the strain signal from the megathrust is minimal (Cross & Freymueller, 2008) increases the size of the block being considered and reduces these indeterminacies.

The new best-fit pole for the PENN block is located in the South Pacific Ocean, 85.4° distant from the center of the PENN block, and with counterclockwise rotation. In order to compare it more easily with the Li et al. (2016) estimated pole, we convert the new estimated pole to its antipode, which is slightly over 90° away (94.6°) from the PENN block and has the same clockwise sense of rotation as the Li et al. (2016) result. This is the pole shown in Figure A.2. The new estimated pole for the PENN block gives systematically smaller trench-parallel residual for sites in the Alaska Peninsula than using the Li et al. (2016) pole. When using this new pole to predict velocities of sites in the Cook Inlet area, we found only a very small difference in misfit for back-slip inversions in that area, so we think this new definition of the PENN block is superior to our earlier version. Figure A.2 shows the locations of poles for all the blocks used in this study, including the pole for the PENN block estimated in Li et al. (2016) and the new pole's antipode (for clockwise rotation) estimated here.

A.3 Inconsistency between the horizontal and vertical velocities

We used both the horizontal and vertical velocities to invert for a locking model, using strong smoothing factors along-strike and down-dip (Figure A.3). There are systematic misfits to the vertical velocity, while the optimal model explains most of the variation in the horizontal data. The pattern of vertical residuals is very long wavelength, and not correlated with the along-strike changes in locking. The Sanak segment is mostly creeping starting from the trench and has no strain related with the subduction zone, but the vertical residuals are almost the same as for sites further east where there is substantial strain. This back-slip model predicts that the Kodiak segment is strongly locked, the Semidi segment is intermediate with a locking ratio ~ 0.7, the Shumagin segment is weakly locked with locking ratio ~ 0.4, and the Sanak segment is creeping dominated, very similar to our preferred model but with smoother along strike changes in locking. Altering the slip distribution can change the fit to the horizontal data but does not reduce the systematic misfit to the vertical.

We tested several possible reasons to explain this long wavelength misfit in the vertical velocities. We considered different published plate geometries (Hayes et al., 2012; Suito & Freymueller, 2009) in the inversion model, different Glacial Isostatic Adjustment (GIA) corrections (ICE-5G, ICE-6G and DeGrandpre, 2015) and evaluated different potential reference frame shifts in the GPS velocities. None of these can explain the vertical residuals. We hypothesize that GIA may be the cause of these motions, but the development of a new GIA model is beyond the scope of this paper.

For the sites west of Kodiak Island, especially on Chirikof Island, vertical residuals are significantly larger than all other sites. The estimated models under-predict the observed subsidence. The same is true even if we allow the near-trench region to creep. A change in the geometry of the shallow plate interface might help improve the model prediction. The previous published slab models are largely determined by the evidence of intermediate slab earthquakes which gives better resolution for the depth of the plate interface in intermediate depths but not shallow depths. Explaining this subsidence by adjusting the plate interface geometry would require a more complex plate boundary geometry which is different from any published plate geometry so far. Direct observations of the interface geometry are lacking, but might come from an upcoming offshore-onshore seismic experiment.

A.4 Inversion Using Horizontal Velocities Only for the whole area: Smoothing Constraints and "Zebra Stripe" Test

We used GPS horizontal velocities only to invert for a locking model and evaluated a range of smoothing factors to determine the trade-off between the misfits and the complexity of the predicted locking distributions (Figure A.4). The optimal smoothed inversion with just the horizontal velocities (Figure A.4c) produced a result that fits the horizontal data better than the inversions including both horizontal and vertical velocities shown in Figure A.3a, but with the same basic characteristics. As expected, the locking models with smaller smoothing factors become increasingly complex and include strong oscillation in the estimated locking in along-strike direction. Conversely, as smoothing is increased and the locking fraction decreases more smoothly from NE to SW through the Alaska Peninsula (Figure A.4). The key result of these comparisons is that strong smoothing within each segment does not degrade the model fit, but any smoothing across the sharp segment boundaries does. This motivated out our approach in sections 4.5.1 and 4.5.2.

To reveal the sensitivity and resolution of the preferred inversion model using GPS horizontal velocities only for the whole area (Figure A.4c), we conducted a synthetic "zebra stripe" test. We generated synthetic data from a forward model with starting ϕ values of either 1 or 0 in a zebra stripe pattern (Figure A.5a) and added random errors with the same variance as those of the observed velocities to the calculated velocities at each station. We then inverted the synthetic data produced in the forward model using the same inversion setting as the preferred smoothed inversion model. We assumed the locking fraction of nodes decreases along downdip direction and also fixed the locking fraction to 0 at the deepest nodes (deeper than 70 km) on the fault because we assumed that a fully slipping state occurs at these depths. The recovery model (Figure A.5b) reproduced the synthetic test model well for the area where GPS stations are most dense on land. It shows that the estimated location of boundary 3 is resolved much better than that of boundary 1 or boundary 2. The uncertainty bounds in the location of the boundaries are consistent with this test (see main text and animations A.4 to A.6). The lack of resolution near the trench, and offshore, especially near boundary 2, is not surprising given the shortage of data offshore and long distance from the shoreline to the trench.

A.5 References

Cross, R. S., & Freymueller, J. T. (2008). Evidence for and implications of a Bering plate based on geodetic measurements from the Aleutians and western Alaska. Journal of Geophysical Research: Solid Earth (1978–2012), 113(B7).

DeGrandpre, K. (2015). Relative Sea Level Change in Western Alaska as Constructed From Satellite Altimetry and Repeat GPS Measurements (M. Sc. Thesis). University of Alaska Fairbanks.

Hayes, G. P., Wald, D. J., & Johnson, R. L. (2012). Slab1. 0: A three-dimensional model of global subduction zone geometries. Journal of Geophysical Research: Solid Earth (1978–2012), 117(B1).

Li, S., Freymueller, J., & McCaffrey, R. (2016). Slow slip events and time-dependent variations in locking beneath Lower Cook Inlet of the Alaska-Aleutian subduction zone. Journal of Geophysical Research: Solid Earth, 121(2), 1060–1079.

Suito, H., & Freymueller, J. T. (2009). A viscoelastic and afterslip postseismic deformation model for the 1964 Alaska earthquake. Journal of Geophysical Research: Solid Earth (1978–2012), 114(B11).

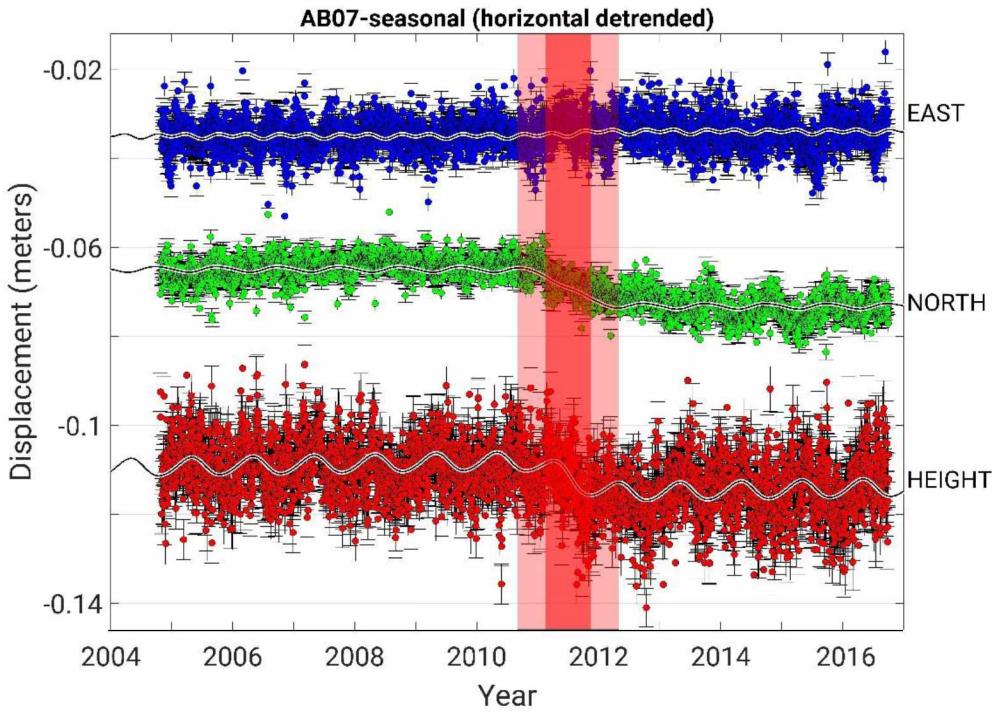

Figure A.1 Time Series of GPS station AB07 in the Alaska Peninsula, detrended based on pre-SSE velocity (GRACE-derived seasonal variation removed and residual seasonal terms are estimated and shown). The strongly shaded area contains 68% of the SSE deformation (2011.5 $\pm$ 0.37). The weakly shaded area contains 95% of the SSE deformation (2011.5 $\pm$ 0.83). The SSE has a center-point of the event at 2011.50.

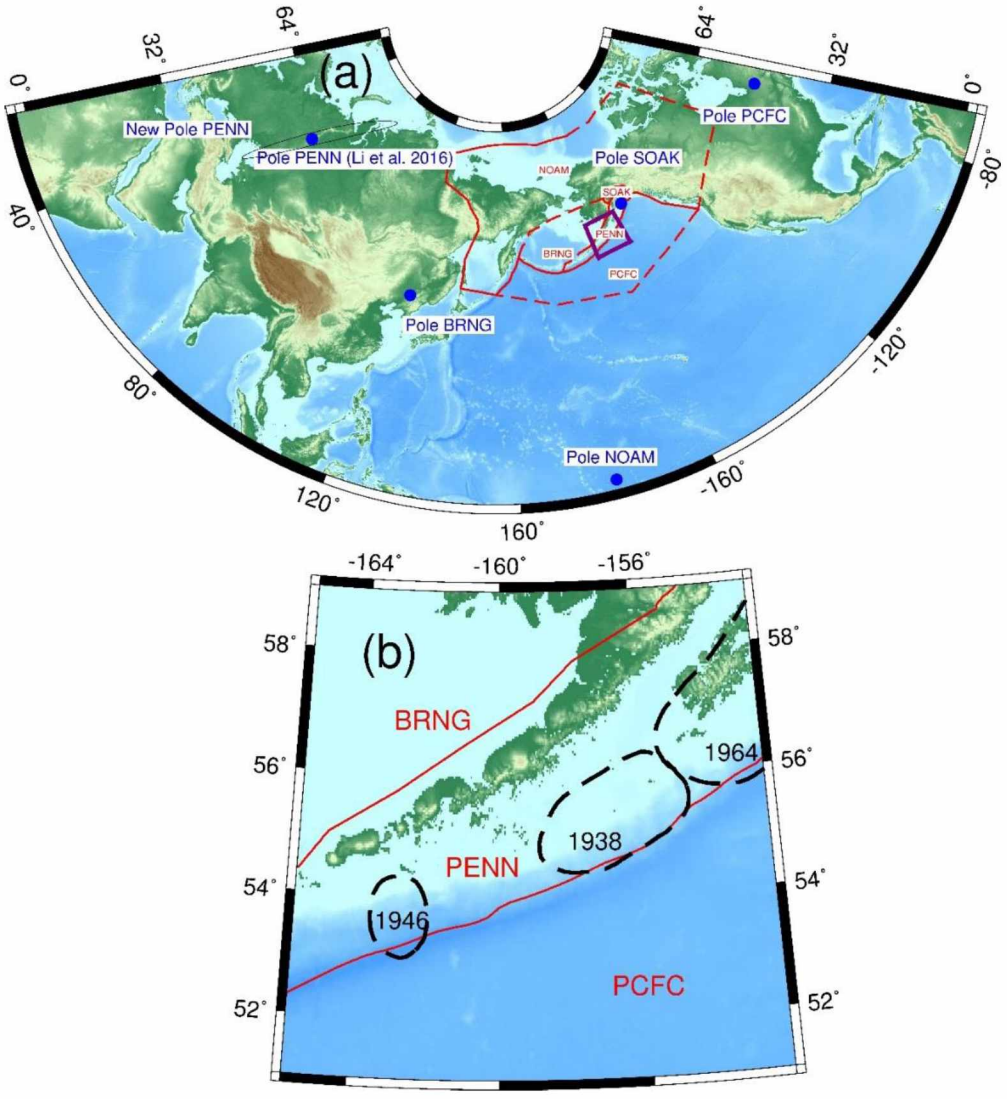

Figure A.2 (a) The location of poles (blue dots) for all the blocks used in this study and (b) a zoom in map of the study area outlined by purple rectangle in (a).The red solid and dashed lines show the block boundaries. The Li et al. (2016) estimated pole for PENN, based on data from Cook Inlet and the Alaska Peninsula, is located in northern Russia. The new estimated pole for PENN, based on data from Alaska Peninsula and sites around Dutch Harbor and Atka, is located in southern Pacific Ocean, mainly 90° away from the Peninsula block. Its amplitude is shown here (clockwise rotation).

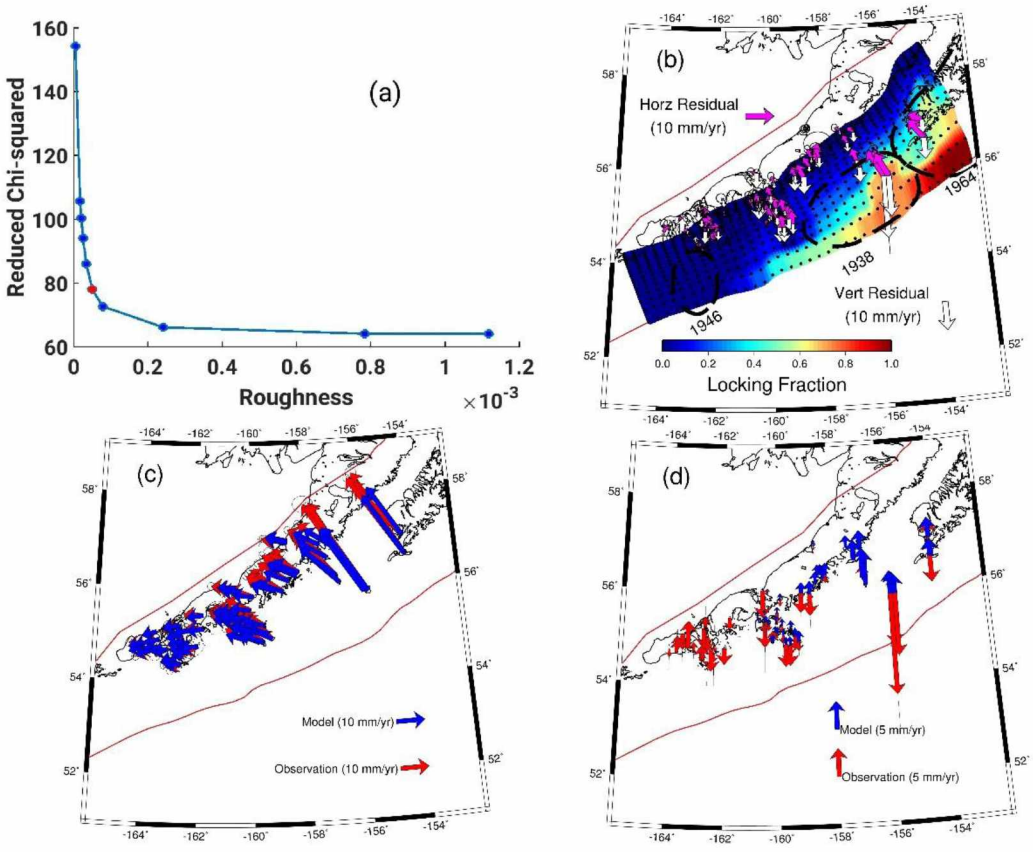

Figure A.3 Trade-off curve and best fit model for inverted locking distribution by using both GPS horizontal and vertical velocities (Smoothing factor are $2 \cdot 10^8$ in along-strike and downdip directions). (a) The trade-off curve between the reduced Chi-squared and model roughness. (b) Residuals for GPS horizontal (magenta) and vertical velocities (white) with the optimal locking model (red circle in (a)); (c) Comparison between the predicted (blue) and observed (red) horizontal velocities; (d) Comparison between the predicted (blue) and observed (red) vertical velocities.

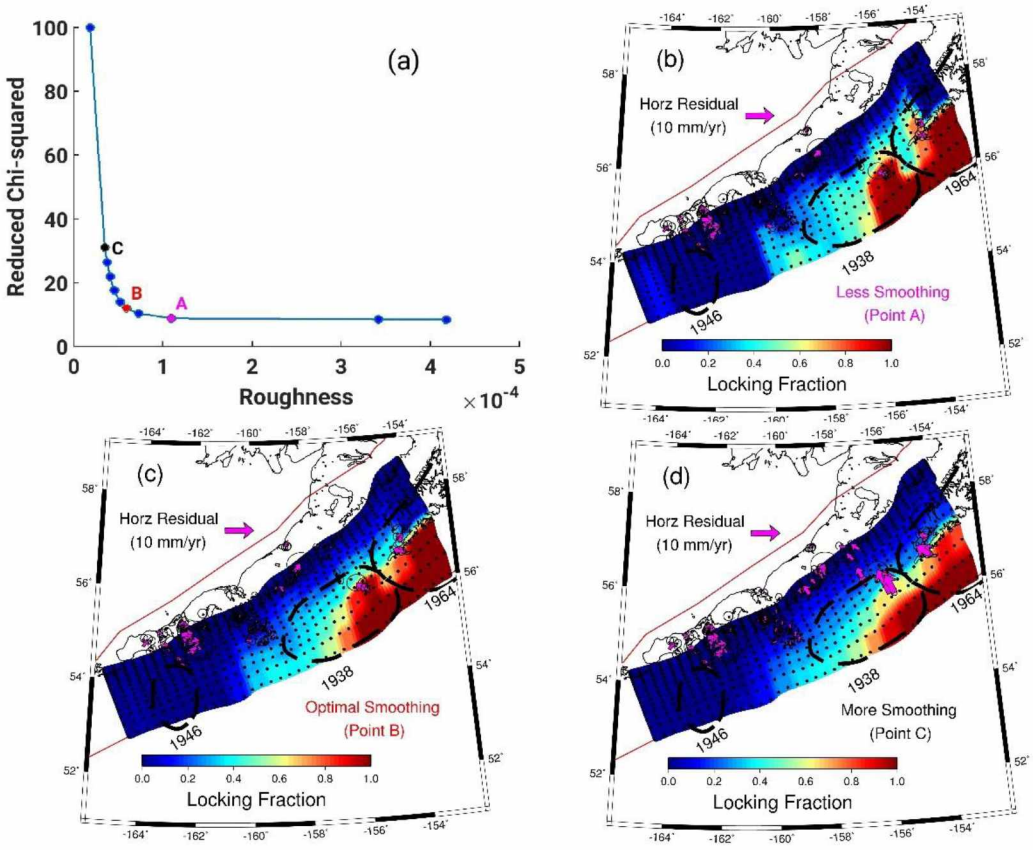

Figure A.4 The trade-off curve and effects of smoothing on the standard inversion model by using GPS horizontal velocities only.(a) The trade-off curve between the reduced Chi-squared value of data and roughness. The magenta circle marked by point A is the smoothing factor $1 \cdot 10^7$ which was selected to show the less smoothed result. The red circle marked by point B is the optimal smoothing factor $1 \cdot 10^8$. The dark circle marked by point C is the smoothing factor $1 \cdot 10^9$, which was selected to show the over-smoothed result. (b) Less smoothing (point A) than preferred model (point B) (c), and (d) more smoothing (point C) than preferred model.

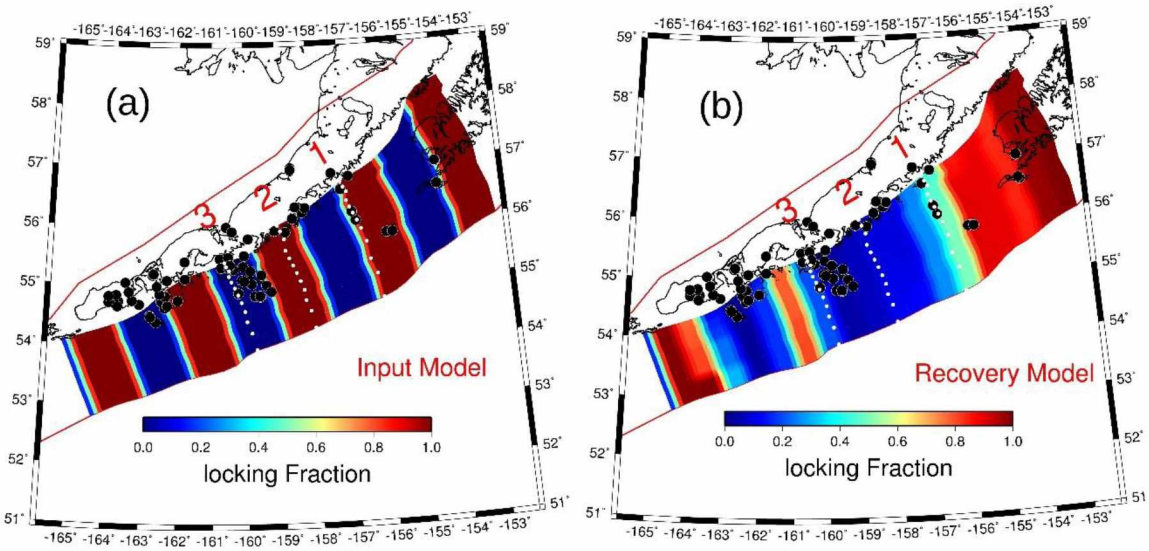

Figure A.5 "Zebra stripe" test showing the spatial resolution of the inversion of GPS horizontal velocities only. In the inversion, we assume locking fraction for nodes always decrease in the downdip direction. (a) The input model. (b) The recovery model with the smoothing factor $1 \cdot 10^8$ from our preferred model in Figure A.4. The numbers and the white dotted lines indicate our estimated optimal boundaries in Figure 4.2.

Table A.1 Estimated East and North Components of GPS velocities for Co-Located Sites in Sand Point (SNDP, AB07 and LSDP).The units for East and North are both mm/yr. SNDP and LSDP are campaign sites with three and four surveys, respectively.

Site	Time Span	East	North
SNDP	1993 - 2003	-8.5 $\pm$ 0.6	2.2 $\pm$ 0.6
SNDP	1995 - 2003	-8.9 $\pm$ 0.6	4.1 $\pm$ 0.6
AB07	2004 - 2011	-8.5 $\pm$ 0.5	3.8 $\pm$ 0.6
AB07 with SSE modeled	2004 - 2016	-8.6 $\pm$ 0.4	4.0 $\pm$ 0.5
LSDP	1993 - 2016	-8.9 $\pm$ 0.5	3.3 $\pm$ 0.5

Animation A.1 Location of the first boundary that marks the sharp change from strongly locked to intermediate. When changing the location of the first boundary from NE to SW as shown in (a), the dashed line indicates the weighted sum square of residuals (WRSS) of each forward model in (b).

Animation A.2 Location of the second boundary that marks the sharp change from intermediate locked to weakly locked. When changing the location of the second boundary from the first boundary to SW as shown in (a), the dashed line indicates the WRSS of each forward model in (b).

Animation A.3 Location of the third boundary that marks the sharp change from weakly locked to creeping-dominated. When changing the location of the third boundary from the second boundary to SW as shown in (a), the dashed line indicates the WRSS of each forward model in (b).

Animation A.4 Changing the width of the first boundary that marks the gradual change from strongly locked to intermediate. When changing the width of the first boundary as shown in (a), the dashed line indicates the WRSS of each forward model in (b).

Animation A.5 Changing the width of the second boundary that marks the gradual change from intermediate to weakly locked. When changing the width of the second boundary as shown in (a), the dashed line indicates the WRSS of each forward model in (b).

Animation A.6 Changing the width of the third boundary that marks the gradual change from weakly locked to creeping-dominated. When changing the width of the third boundary as shown in (a), the dashed line indicates the WRSS of each forward model in (b).

Appendix B

General Appendix

The following statements are from coauthors, which are not committee members, granting permission for including published and submitted manuscripts in this dissertation.

28 March 2018

Dear Shanshan,

I give you my permission to use the following paper in your dissertation.

Li, S., J. Freymueller, and R. McCaffrey (2016), Slow slip events and time-dependent variations in locking beneath Lower Cook Inlet of the Alaska-Aleutian subduction zone, *J. Geophys. Res. Solid Earth*, 121, 1060–1079, *doi:* 10.1002/2015JB012491.

Sincerely,

Rob McCaffrey
Portland State University

Permission to include journal article in dissertation

Jianjun, Wang jjwang@sgg.whu.edu.cn March 28th, 2018
To: Shanshan Li <sli11@alaska.edu>

To whom it may concern,

I, Jianjun Wang, give permission to Shanshan Li to use the following paper in her dissertation for which I am a coauthor.

Li, S., J. Freymueller, J. Wang and N. Ruppert, (submitted), Correlation between Coulomb Stress Rate Change imparted by the Slow Slip Events and Seismic Rate Change in Lower Cook Inlet of the Alaska-Aleutian Subduction Zone, Journal of Geophysical Research: Solid Earth.

Regards,
Jianjun

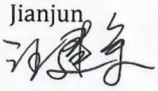

Jianjun Wang
Lecturer
School of Geodesy and Geomatics
Wuhan University
Wuhan, China 430079
Tel:+(86) 027-68771793
Email:jjwang@sgg.whu.edu.cn

permission to include journal article in dissertation

Natalia Ruppert <naruppert@alaska.edu> Tue, Mar 27, 2018 at 3:16 PM
To: Shanshan Li <sli11@alaska.edu>

To whom it may concern:

I, Natalia Ruppert, give permission to Shanhnan Li to use the following paper in her dissertation for which I am a coauthor.

Li, S., J. Freymueller, J. Wang and N. Ruppert, (submitted), Correlation between Coulomb Stress Rate Change imparted by the Slow Slip Events and Seismic Rate Change in Lower Cook Inlet of the Alaska-Aleutian Subduction Zone, Journal of Geophysical Research: Solid Earth.

Best regards.

~~~
~~~